



Marcello Alves Reis

**Mode-Matching Technique Along Oblique
Surfaces and Applications to the Modeling of
Curved Waveguides**

Dissertação de Mestrado

Thesis presented to the Programa de Pós-graduação em Engenharia Elétrica, do Departamento de Engenharia Elétrica da PUC-Rio in partial fulfillment of the requirements for the degree of Mestre em Engenharia Elétrica.

Advisor: Prof. Guilherme Simon da Rosa

Rio de Janeiro
March 2023



Marcello Alves Reis

**Mode-Matching Technique Along Oblique
Surfaces and Applications to the Modeling of
Curved Waveguides**

Thesis presented to the Programa de Pós-graduação em Engenharia Elétrica da PUC-Rio in partial fulfillment of the requirements for the degree of Mestre em Engenharia Elétrica. Approved by the Examination Committee:

Prof. Guilherme Simon da Rosa

Advisor

Departamento de Engenharia Elétrica – PUC-Rio

Prof. Maiquel dos Santos Canabarro

Universidade Federal de Pelotas – UFPel

Prof. Luiz Alencar Reis da Silva Mello

Departamento de Engenharia Elétrica – PUC-Rio

Rio de Janeiro, March the 16th, 2023

All rights reserved.

Marcello Alves Reis

He received his B.S. degree in Electric Engineering from Universidade do Estado do Rio de Janeiro (UERJ), Rio de Janeiro, Brazil, in 2013. He is currently pursuing a Master's degree in Applied Electromagnetism in the Center for Telecommunications Studies at PUC-Rio.

Bibliographic data

Alves Reis, Marcello

Mode-Matching Technique Along Oblique Surfaces and Applications to the Modeling of Curved Waveguides / Marcello Alves Reis; advisor: Guilherme Simon da Rosa. – 2023.

105 f: il. color. ; 30 cm

Dissertação (mestrado) - Pontifícia Universidade Católica do Rio de Janeiro, Departamento de Engenharia Elétrica, 2023.

Inclui bibliografia

1. Engenharia Elétrica – Teses. 2. Engenharia de Telecomunicações – Teses. 3. Superfícies oblíquas. 4. Guias de ondas cilíndricos curvos. 5. Método de casamento de modos. I. Simon da Rosa, Guilherme. II. Pontifícia Universidade Católica do Rio de Janeiro. Departamento de Engenharia Elétrica. III. Título.

CDD: 621.3

To my family, for their support
and encouragement.

Acknowledgments

I would like to start by thanking my advisor Guilherme Simon da Rosa for his constant assistance, guidance, encouragement, and suggestions during this project.

I would like to thank to PUC-Rio for the exemption of school fees offered by the Programa de Pós-Graduação em Engenharia Elétrica.

This study was financed by the Pontifical Catholic University of Rio de Janeiro (PUC-Rio).

This study was financed in part by the Coordenação de Aperfeiçoamento de Pessoal de Nível Superior – Brasil (CAPES) – Finance Code 001.

I would like to thank the Brazilian Navy for the trust and the opportunity to do this master's course.

I would also like to thank my parents Jorge and Rita and my brother Rodrigo for their encouragement, and thank my friend Paulo for supporting me during the whole course.

Finally, I thank my wife Stefany for the daily support and understanding, and I especially thank my daughter Maria Antônia for being the inspiration for everything in my life.

Abstract

Alves Reis, Marcello; Simon da Rosa, Guilherme (Advisor). **Mode-Matching Technique Along Oblique Surfaces and Applications to the Modeling of Curved Waveguides**. Rio de Janeiro, 2023. 105p. Dissertação de Mestrado – Departamento de Engenharia Elétrica, Pontifícia Universidade Católica do Rio de Janeiro.

Waveguides are widely used in telecommunications engineering for transmitting signals and manufacturing filters and other devices in the microwave applications. In this work, we present a formulation based on the mode-matching technique (MMT) for the analysis of discontinuities in cylindrical waveguides caused by curvatures in the longitudinal axis of the transmission line. We present and validate a technique for modal analysis of curved waveguides by approximating the curvature in a succession of oblique surfaces by means of their generalized scattering matrices (GSMs) extracted from the MMT. The present approach is a computationally efficient alternative for modeling curvature in cylindrical waveguides when compared to usual numerical brute force techniques (such as element-based, volume-based, or finite difference solutions). An algorithm is presented to compute the GSM matrix elements for different configurations of waveguide junctions. The novelty of the present method consists in considering the projection of electromagnetic fields onto oblique surfaces for the application of MMT. We present a series of numerical results that show that the technique presented in this study can guarantee results with good accuracy and precision when performing the analysis of the modal behavior of electromagnetic fields at discontinuities caused by curvatures.

Keywords

Oblique surfaces; Cylindrical curved waveguides; Mode-Matching technique.

Resumo

Alves Reis, Marcello; Simon da Rosa, Guilherme. **Método de Casamento de Modos ao Longo de Superfícies Oblíquas e Aplicações para a Modelagem de Guias de Ondas Curvados**. Rio de Janeiro, 2023. 105p. Dissertação de Mestrado – Departamento de Engenharia Elétrica, Pontifícia Universidade Católica do Rio de Janeiro.

Guias de onda são amplamente utilizados na engenharia de telecomunicações para a transmissão de sinais e construção de filtros e outros dispositivos de micro-ondas. Neste trabalho, apresentamos uma formulação baseada na técnica de casamento de modos (MMT) para a análise de descontinuidades em guias de ondas cilíndricos causadas por curvaturas no eixo longitudinal da linha de transmissão. Apresentamos e validamos uma técnica para análise modal de guias de ondas curvos através da aproximação da curvatura por uma sucessão de superfícies oblíquas por meio de suas matrizes de espalhamento generalizadas (GSMs) extraídas do MMT. A presente abordagem é uma alternativa computacionalmente eficiente para modelar curvaturas em guias de ondas cilíndricos quando comparada às técnicas usuais de força bruta numérica (tais como soluções baseadas em elementos, volumes, ou diferenças finitas). Um algoritmo é apresentado para calcular os elementos da matriz GSM para diferentes configurações de junções de guias de onda. A novidade do presente método consiste em considerar a projeção dos campos eletromagnéticos em superfícies oblíquas para a aplicação do MMT. Apresentamos uma série de resultados numéricos que mostram que a técnica apresentada neste estudo pode garantir resultados com boa acurácia e precisão ao realizar a análise do comportamento modal dos campos eletromagnéticos em descontinuidades provocados por curvaturas.

Palavras-chave

Superfícies oblíquas; Guias de ondas cilíndricos curvos; Método de casamento de modos.

Table of contents

1	Introduction	16
1.1	General Introduction	16
1.2	Scientific Contributions	18
1.3	Dissertation Organization	18
2	Electromagnetic Fields in Cylindrical Waveguides	20
2.1	Introduction	20
2.2	Circular Wave functions	21
2.3	Propagation Modes in Circular Waveguide	26
3	MMT Along Oblique Junctions	30
3.1	Introduction	30
3.2	MMT Formulation	31
3.3	Waveguides with Oblique Junction	32
3.4	Reaction Integrals	39
3.4.1	Special Case of a Straight Junction	45
3.5	Generalized Scattering Matrix	47
3.6	Cascading Generalized Scattering Matrices	47
4	MMT Algorithm Validation and Results	51
4.1	Introduction	51
4.2	Algorithm Structure	51
4.3	Straight Junctions Validation Results	52
4.3.1	Case 1	52
4.3.2	Case 2	54
4.3.3	Case 3	57
4.3.4	Case 4	60
4.4	Oblique Junctions Results	67
4.4.1	Case 1	67
4.4.2	Case 2	75
5	Conclusion	100
	Bibliography	102

List of figures

Figure 1.1	X-Band antenna structure with curved waveguides.	17
Figure 2.1	Cylindrical waveguides. [1]	20
Figure 2.2	Rectangular and Cylindrical coordinate systems. [2]	21
Figure 2.3	Cylindrical waveguide in \hat{z} direction [2]	23
Figure 2.4	Fields configuration of first 9 lower order modes. [2]	29
Figure 3.1	Representation of transmitted and reflected waves at a coaxial waveguide discontinuity.	31
Figure 3.2	Uniform circular waveguide with the longitudinal axis align with the z -axis.	32
Figure 3.3	View of (x_1, y_1, z_1) and (x_2, y_2, z_2) coordinate systems.	33
Figure 3.4	Junction of two straight waveguides along a oblique surface described by the tilt angle θ_{12} .	34
Figure 3.5	Waveguide junctions showing the surfaces S_1 , S_2 , and \tilde{S}_1 .	37
Figure 3.6	View of the S_J surface over the plane $z_J = 0$.	41
Figure 3.7	Junction of two straight waveguides.	45
Figure 3.8	Waveguide with three different regions.	49
Figure 3.9	A 90-degree curved waveguide discretized into 5 regions.	50
Figure 4.1	Geometry of a straight waveguide junction.	52
Figure 4.2	Reflection coefficient from $g = 2$ to $g = 10$. Results from CST and Matlab.	53
Figure 4.3	Qualwave's circular waveguide specifications for Ku-band frequency ranges. [3]	57
Figure 4.4	Straight waveguide device with three sections.	60
Figure 4.5	Results for (a) $L = 5$ mm $\epsilon_2 = 2\epsilon_0$ and (b) $L = 10$ mm $\epsilon_2 = 2\epsilon_0$.	61
Figure 4.6	Results for (a) $L = 15$ mm $\epsilon_2 = 2\epsilon_0$ and (b) $L = 20$ mm $\epsilon_2 = 2\epsilon_0$.	62
Figure 4.7	Results for (a) $L = 25$ mm $\epsilon_2 = 2\epsilon_0$ and (b) $L = 30$ mm $\epsilon_2 = 2\epsilon_0$.	63
Figure 4.8	Results for (a) $L = 5$ mm $\epsilon_2 = 4\epsilon_0$ and (b) $L = 10$ mm $\epsilon_2 = 4\epsilon_0$.	64
Figure 4.9	Results for (a) $L = 15$ mm $\epsilon_2 = 4\epsilon_0$ (b) $L = 20$ mm $\epsilon_2 = 4\epsilon_0$.	65
Figure 4.10	Results for (a) $L = 25$ mm $\epsilon_2 = 4\epsilon_0$ and (b) $L = 30$ mm $\epsilon_2 = 4\epsilon_0$.	66
Figure 4.11	Geometry of an oblique waveguide junction.	67
Figure 4.12	CST structure with TE_{11}^z mode excitation as a $\sin(n\phi)$ configuration.	68
Figure 4.13	CST structure with TE_{11}^z mode excitation as a $\cos(n\phi)$ configuration.	68
Figure 4.14	Absolute error (dB) between CST simulation and algorithm (with $n = 1$) for TE_{11}^z mode as a $\cos(n\phi)$.	69

Figure 4.15 Absolute error (dB) between CST simulation and algorithm (with $n = 2$) for TE_{11}^z mode as a $\cos(n\phi)$.	70
Figure 4.16 Absolute error (dB) between CST simulation and algorithm (with $n = 3$) for TE_{11}^z mode as a $\cos(n\phi)$.	71
Figure 4.17 Absolute error (dB) between CST simulation and algorithm (with $n = 1$) for TE_{11}^z mode as a $\sin(n\phi)$.	72
Figure 4.18 Absolute error (dB) between CST simulation and algorithm (with $n = 2$) for TE_{11}^z mode as a $\sin(n\phi)$.	73
Figure 4.19 Absolute error (dB) between CST simulation and algorithm (with $n = 3$) for TE_{11}^z mode as a $\sin(n\phi)$.	74
Figure 4.20 Reflection Coefficient TE_{11}^z mode as a $\cos(n\phi)$.	75
Figure 4.21 Reflection Coefficient for TE_{11}^z mode as a $\sin(n\phi)$.	75
Figure 4.22 Absolute error for the configuration $\cos(n\phi)$, with $f = 10$ GHz.	76
Figure 4.23 Absolute error for the configuration $\cos(n\phi)$, with $f = 10.5$ GHz.	77
Figure 4.24 Absolute error for the configuration $\cos(n\phi)$, with $f = 11$ GHz.	78
Figure 4.25 Absolute error for the configuration $\cos(n\phi)$, with $f = 11.5$ GHz.	79
Figure 4.26 Absolute error for the configuration $\cos(n\phi)$, with $f = 12$ GHz.	80
Figure 4.27 Absolute error for the configuration $\cos(n\phi)$, with $f = 12.5$ GHz.	81
Figure 4.28 Absolute error for the configuration $\cos(n\phi)$, with $f = 13$ GHz.	82
Figure 4.29 Absolute error for the configuration $\cos(n\phi)$, with $f = 13.5$ GHz.	83
Figure 4.30 Absolute error for the configuration $\cos(n\phi)$, with $f = 14$ GHz.	84
Figure 4.31 Absolute error for the configuration $\cos(n\phi)$, with $f = 14.5$ GHz.	85
Figure 4.32 Absolute error for the configuration $\cos(n\phi)$, with $f = 15$ GHz.	86
Figure 4.33 Absolute error for the configuration $\sin(n\phi)$, with $f = 10$ GHz.	87
Figure 4.34 Absolute error for the configuration $\sin(n\phi)$, with $f = 10.5$ GHz.	88
Figure 4.35 Absolute error for the configuration $\sin(n\phi)$, with $f = 11$ GHz.	89
Figure 4.36 Absolute error for the configuration $\sin(n\phi)$, with $f = 11.5$ GHz.	90
Figure 4.37 Absolute error for the configuration $\sin(n\phi)$, with $f = 12$ GHz.	91
Figure 4.38 Absolute error for the configuration $\sin(n\phi)$, with $f = 12.5$ GHz.	92
Figure 4.39 Absolute error for the configuration $\sin(n\phi)$, with $f = 13$ GHz.	93

Figure 4.40 Absolute error for the configuration $\sin(n\phi)$, with $f = 13.5$ GHz.	94
Figure 4.41 Absolute error for the configuration $\sin(n\phi)$, with $f = 14$ GHz.	95
Figure 4.42 Absolute error for the configuration $\sin(n\phi)$, with $f = 14.5$ GHz.	96
Figure 4.43 Absolute error for the configuration $\sin(n\phi)$, with $f = 15$ GHz.	97
Figure 4.44 Reflection coefficient from CST for $\text{TE}_{11}^z = \cos(n\phi)$.	98
Figure 4.45 Reflection coefficient from our algorithm ($n = 2$ and $p = 1$) for $\text{TE}_{11}^z = \cos(n\phi)$.	98
Figure 4.46 Reflection coefficient from CST for $\text{TE}_{11}^z = \sin(n\phi)$.	99
Figure 4.47 Reflection coefficient from our algorithm ($n = 1$ and $p = 1$) for $\text{TE}_{11}^z = \sin(n\phi)$.	99

List of tables

Table 2.1	Ordered zeros x_{np} of $J_n(x)$.	27
Table 2.2	Ordered zeros x'_{np} of $J'_n(x)$.	28
Table 4.1	Results of the reflection coefficient with $f = 10$ GHz and relative permittivity ϵ_2 varying with $g = 2$ to $g = 10$, using Matlab algorithm (with $n = 1$ and $p = 1$) and CST simulation.	53
Table 4.2	Results of the reflection coefficient with $f = 10$ GHz to $f = 15$ GHz and $\epsilon_2 = 2\epsilon_1$, using Matlab algorithm (with $n = 1$ and $p = 1$) and CST simulation.	54
Table 4.3	Results of the reflection coefficient with $f = 10$ GHz to $f = 15$ GHz and $\epsilon_2 = 3\epsilon_1$, using Matlab algorithm (with $n = 1$ and $p = 1$) and CST simulation.	55
Table 4.4	Results of the reflection coefficient with $f = 10$ GHz to $f = 15$ GHz and $\epsilon_2 = 4\epsilon_1$, using Matlab algorithm (with $n = 1$ and $p = 1$) and CST simulation.	55
Table 4.5	Results of the reflection coefficient with $f = 10$ GHz to $f = 15$ GHz and $\epsilon_2 = 5\epsilon_1$, using Matlab algorithm (with $n = 1$ and $p = 1$) and CST simulation.	56
Table 4.6	Results of the reflection coefficient with $f = 13.4$ GHz to $f = 18.0$ GHz and $\epsilon_2 = 2\epsilon_1$, using Matlab algorithm (with $n = 1$ and $p = 1$) and CST simulation.	57
Table 4.7	Results of the reflection coefficient with $f = 13.4$ GHz to $f = 18.0$ GHz and $\epsilon_2 = 3\epsilon_1$, using Matlab algorithm (with $n = 1$ and $p = 1$) and CST simulation.	58
Table 4.8	Results of the reflection coefficient with $f = 13.4$ GHz to $f = 18.0$ GHz and $\epsilon_2 = 4\epsilon_1$, using Matlab algorithm (with $n = 1$ and $p = 1$) and CST simulation.	58
Table 4.9	Results of the reflection coefficient with $f = 13.4$ GHz to $f = 18.0$ GHz and $\epsilon_2 = 5\epsilon_1$, using Matlab algorithm (with $n = 1$ and $p = 1$) and CST simulation.	59
Table 4.10	Results from Matlab algorithm (with $n = 1$ and $p = 1$) and CST simulation for the reflection coefficient with frequency ranging from 10 GHz to 15 GHz, $\epsilon_2 = 2\epsilon_0$ and L equals to 5 mm and 10 mm.	61
Table 4.11	Results from Matlab algorithm (with $n = 1$ and $p = 1$) and CST simulation for the reflection coefficient with frequency ranging from 10 GHz to 15 GHz, $\epsilon_2 = 2\epsilon_0$ and L equals to 15 mm and 20 mm.	62
Table 4.12	Results from Matlab algorithm (with $n = 1$ and $p = 1$) and CST simulation for the reflection coefficient with frequency ranging from 10 GHz to 15 GHz, $\epsilon_2 = 2\epsilon_0$ and L equals to 25 mm and 30 mm.	63

Table 4.13 Results from Matlab algorithm (with $n = 1$ and $p = 1$) and CST simulation for the reflection coefficient with frequency ranging from 10 GHz to 15 GHz, $\epsilon_2 = 4\epsilon_0$ and L equals to 5 mm and 10 mm	64
Table 4.14 Results from Matlab algorithm (with $n = 1$ and $p = 1$) and CST simulation for the reflection coefficient with frequency ranging from 10 GHz to 15 GHz, $\epsilon_2 = 4\epsilon_0$ and L equals to 15 mm and 20 mm.	65
Table 4.15 Results from Matlab algorithm (with $n = 1$ and $p = 1$) and CST simulation for the reflection coefficient with frequency ranging from 10 GHz to 15 GHz, $\epsilon_2 = 4\epsilon_0$ and L equals to 25 mm and 30 mm.	66
Table 4.16 Results of the reflection coefficient for TE_{11}^z mode as a $\cos(n\phi)$ with $f = 10$ GHz and θ ($2\theta_{12}$) ranging from 10° to 90° , using Matlab algorithm (with $n = 1$ and $p = 1, 2,$ and 3) and comparing with CST simulation.	69
Table 4.17 Results of the reflection coefficient for TE_{11}^z mode as a $\cos(n\phi)$ with $f = 10$ GHz and θ ($2\theta_{12}$) ranging from 10° to 90° , using Matlab algorithm (with $n = 2$ and $p = 1, 2,$ and 3) and comparing with CST simulation.	70
Table 4.18 Results of the reflection coefficient for TE_{11}^z mode as a $\cos(n\phi)$ with $f = 10$ GHz and θ ($2\theta_{12}$) ranging from 10° to 90° , using Matlab algorithm (with $n = 3$ and $p = 1, 2,$ and 3) and comparing with CST simulation.	71
Table 4.19 Results of the reflection coefficient for TE_{11}^z mode as a $\sin(n\phi)$ with $f = 10$ GHz and θ ($2\theta_{12}$) ranging from 10° to 90° , using Matlab algorithm (with $n = 1$ and $p = 1, 2,$ and 3) and comparing with CST simulation.	72
Table 4.20 Results of the reflection coefficient for TE_{11}^z mode as a $\sin(n\phi)$ with $f = 10$ GHz and θ ($2\theta_{12}$) ranging from 10° to 90° , using Matlab algorithm (with $n = 2$ and $p = 1, 2,$ and 3) and comparing with CST simulation.	73
Table 4.21 Results of the reflection coefficient for TE_{11}^z mode as a $\sin(n\phi)$ with $f = 10$ GHz and θ ($2\theta_{12}$) ranging from 10° to 90° , using Matlab algorithm (with $n = 3$ and $p = 1, 2,$ and 3) and comparing with CST simulation.	74
Table 4.22 Results of the reflection coefficient for TE_{11}^z mode as a $\cos(n\phi)$ with $f = 10$ GHz and θ ($2\theta_{12}$) ranging from 5° to 30° , using Matlab algorithm (with $n = 1, 2,$ and 3 and $p = 1$) and comparing with CST simulation.	76
Table 4.23 Results of the reflection coefficient for TE_{11}^z mode as a $\cos(n\phi)$ with $f = 10.5$ GHz and θ ($2\theta_{12}$) ranging from 5° to 30° , using Matlab algorithm (with $n = 1, 2,$ and 3 and $p = 1$) and comparing with CST simulation.	77
Table 4.24 Results of the reflection coefficient for TE_{11}^z mode as a $\cos(n\phi)$ with $f = 11$ GHz and θ ($2\theta_{12}$) ranging from 5° to 30° , using Matlab algorithm (with $n = 1, 2,$ and 3 and $p = 1$) and comparing with CST simulation.	78

Table 4.25 Results of the reflection coefficient for TE_{11}^z mode as a $\cos(n\phi)$ with $f = 11.5$ GHz and θ ($2\theta_{12}$) ranging from 5° to 30° , using Matlab algorithm (with $n = 1, 2$, and 3 and $p = 1$) and comparing with CST simulation.	79
Table 4.26 Results of the reflection coefficient for TE_{11}^z mode as a $\cos(n\phi)$ with $f = 12$ GHz and θ ($2\theta_{12}$) ranging from 5° to 30° , using Matlab algorithm (with $n = 1, 2$, and 3 and $p = 1$) and comparing with CST simulation.	80
Table 4.27 Results of the reflection coefficient for TE_{11}^z mode as a $\cos(n\phi)$ with $f = 12.5$ GHz and θ ($2\theta_{12}$) ranging from 5° to 30° , using Matlab algorithm (with $n = 1, 2$, and 3 and $p = 1$) and comparing with CST simulation.	81
Table 4.28 Results of the reflection coefficient for TE_{11}^z mode as a $\cos(n\phi)$ with $f = 13$ GHz and θ ($2\theta_{12}$) ranging from 5° to 30° , using Matlab algorithm (with $n = 1, 2$, and 3 and $p = 1$) and comparing with CST simulation.	82
Table 4.29 Results of the reflection coefficient for TE_{11}^z mode as a $\cos(n\phi)$ with $f = 13.5$ GHz and θ ($2\theta_{12}$) ranging from 5° to 30° , using Matlab algorithm (with $n = 1, 2$, and 3 and $p = 1$) and comparing with CST simulation.	83
Table 4.30 Results of the reflection coefficient for TE_{11}^z mode as a $\cos(n\phi)$ with $f = 14$ GHz and θ ($2\theta_{12}$) ranging from 5° to 30° , using Matlab algorithm (with $n = 1, 2$, and 3 and $p = 1$) and comparing with CST simulation.	84
Table 4.31 Results of the reflection coefficient for TE_{11}^z mode as a $\cos(n\phi)$ with $f = 14.5$ GHz and θ ($2\theta_{12}$) ranging from 5° to 30° , using Matlab algorithm (with $n = 1, 2$, and 3 and $p = 1$) and comparing with CST simulation.	85
Table 4.32 Results of the reflection coefficient for TE_{11}^z mode as a $\cos(n\phi)$ with $f = 15$ GHz and θ ($2\theta_{12}$) ranging from 5° to 30° , using Matlab algorithm (with $n = 1, 2$, and 3 and $p = 1$) and comparing with CST simulation.	86
Table 4.33 Results of the reflection coefficient for TE_{11}^z mode as a $\sin(n\phi)$ with $f = 10$ GHz and θ ($2\theta_{12}$) ranging from 5° to 30° , using Matlab algorithm (with $n = 1, 2$, and 3 and $p = 1$) and comparing with CST simulation.	87
Table 4.34 Results of the reflection coefficient for TE_{11}^z mode as a $\sin(n\phi)$ with $f = 10.5$ GHz and θ ($2\theta_{12}$) ranging from 5° to 30° , using Matlab algorithm (with $n = 1, 2$, and 3 and $p = 1$) and comparing with CST simulation.	88
Table 4.35 Results of the reflection coefficient for TE_{11}^z mode as a $\sin(n\phi)$ with $f = 11$ GHz and θ ($2\theta_{12}$) ranging from 5° to 30° , using Matlab algorithm (with $n = 1, 2$, and 3 and $p = 1$) and comparing with CST simulation.	89
Table 4.36 Results of the reflection coefficient for TE_{11}^z mode as a $\sin(n\phi)$ with $f = 11.5$ GHz and θ ($2\theta_{12}$) ranging from 5° to 30° , using Matlab algorithm (with $n = 1, 2$, and 3 and $p = 1$) and comparing with CST simulation.	90

Table 4.37 Results of the reflection coefficient for TE_{11}^z mode as a $\sin(n\phi)$ with $f = 12$ GHz and θ ($2\theta_{12}$) ranging from 5° to 30° , using Matlab algorithm (with $n = 1, 2$, and 3 and $p = 1$) and comparing with CST simulation.	91
Table 4.38 Results of the reflection coefficient for TE_{11}^z mode as a $\sin(n\phi)$ with $f = 12.5$ GHz and θ ($2\theta_{12}$) ranging from 5° to 30° , using Matlab algorithm (with $n = 1, 2$, and 3 and $p = 1$) and comparing with CST simulation.	92
Table 4.39 Results of the reflection coefficient for TE_{11}^z mode as a $\sin(n\phi)$ with $f = 13$ GHz and θ ($2\theta_{12}$) ranging from 5° to 30° , using Matlab algorithm (with $n = 1, 2$, and 3 and $p = 1$) and comparing with CST simulation.	93
Table 4.40 Results of the reflection coefficient for TE_{11}^z mode as a $\sin(n\phi)$ with $f = 13.5$ GHz and θ ($2\theta_{12}$) ranging from 5° to 30° , using Matlab algorithm (with $n = 1, 2$, and 3 and $p = 1$) and comparing with CST simulation.	94
Table 4.41 Results of the reflection coefficient for TE_{11}^z mode as a $\sin(n\phi)$ with $f = 14$ GHz and θ ($2\theta_{12}$) ranging from 5° to 30° , using Matlab algorithm (with $n = 1, 2$, and 3 and $p = 1$) and comparing with CST simulation.	95
Table 4.42 Results of the reflection coefficient for TE_{11}^z mode as a $\sin(n\phi)$ with $f = 14.5$ GHz and θ ($2\theta_{12}$) ranging from 5° to 30° , using Matlab algorithm (with $n = 1, 2$, and 3 and $p = 1$) and comparing with CST simulation.	96
Table 4.43 Results of the reflection coefficient for TE_{11}^z mode as a $\sin(n\phi)$ with $f = 15$ GHz and θ ($2\theta_{12}$) ranging from 5° to 30° , using Matlab algorithm (with $n = 1, 2$, and 3 and $p = 1$) and comparing with CST simulation.	97

1 Introduction

1.1 General Introduction

The demand for compact microwave devices has been on the rise due to the increasing use of high-frequency systems in electrical engineering. However, propagating 3D guided waves within structures that have some curvature, such as the connections between a signal generator and the feeder of some antennas (as shown in Fig. 1.1), has posed a challenge. At higher frequencies, curved dielectric waveguides are fundamental building blocks in many optical devices [4]. Thus, studying the behavior of guided waves that propagate in curved transmission lines has become important in recent years. However, the existing literature on the theory of propagation in curved waveguides is limited compared to that on straight waveguides with rectangular and circular cross-section. Analytical techniques that use equivalent circuits to represent isolated discontinuities are commonly used to analyze this type of situation, but they have limitations related to the size of the structure being analyzed, making it difficult to model unconventional structures. Some of these approaches are discussed in [5], [6], and [7].

To analyze problems with complex geometries, numerical methods such as the finite element method, finite volume method, or finite difference method are commonly used. These methods are highly versatile and allow for the rigorous solution of Maxwell's equations to obtain satisfactory solutions for 3D structures. However, one drawback is the large computational cost involved. In [8], a frequency-domain finite-difference method formulated in an orthogonal curvilinear coordinate system was used for the analysis of curved waveguides. In [9] and [10], the method of moments (MoM) as used with the Galerkin's procedure for solving a similar problem. In [11], a system of generalized telegrapher's equations was formulated for E- and H-plane bend waveguide configurations, where the corresponding fields in the curved section were expanded as a superposition of the modes of a straight waveguide. A matrix representation of the coupling mode equations was used to extract a GSM of a bent waveguide region. A similar method was used in [12] for the analysis of

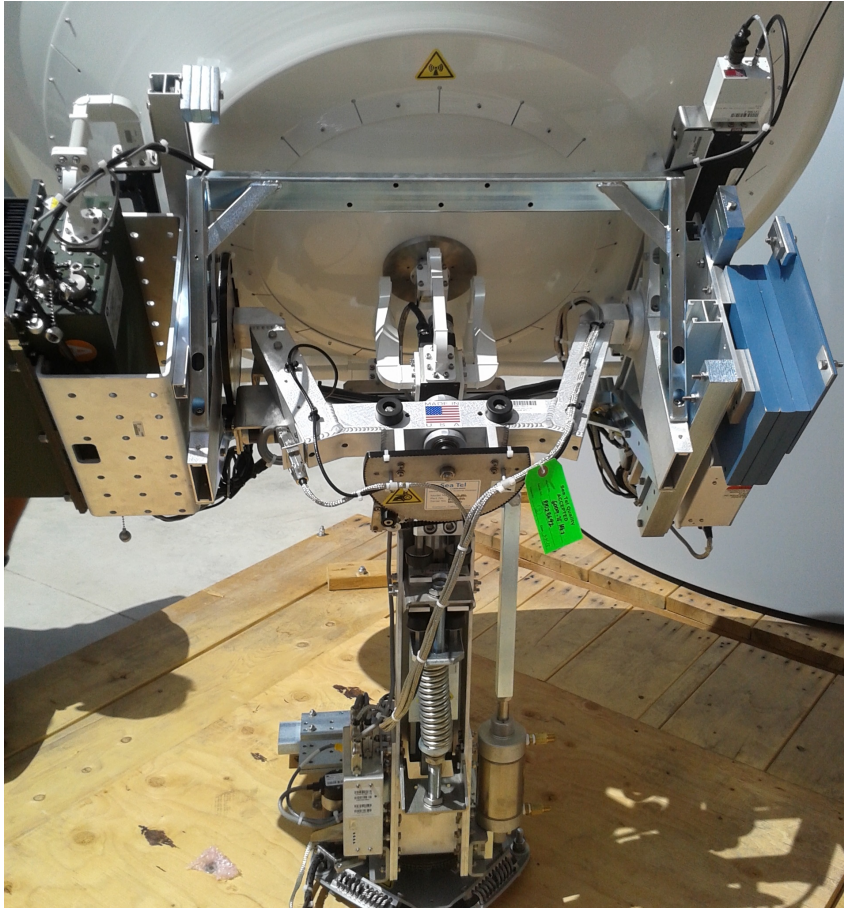


Figure 1.1: X-Band antenna structure with curved waveguides.

curved waveguide mode converters.

For problems with less complex 3D geometries, where wave functions of the constituent waveguide sections are known, an alternative approach is the mode-matching method (MMT). This semi-analytical method involves expanding electromagnetic fields in terms of modal fields in a 2D uniform waveguide and determining coupling integrals to enforce modal field continuity at the junction of adjacent waveguide segments. Since these integrals are generally analytic, the computational cost of solving problems is lower than that of purely numerical methods. By calculating coupling integrals for all modes in the problem, a generalized scattering matrix (GSM) can be obtained for each discontinuity of the analyzed geometry. The cascading of GSMs can then be used to describe complex 3D geometries formed by several connected waveguides.

MMT is widely used for analyzing discontinuity problems in waveguides. For example, in [13], the MMT was used to analyze the transition from substrate integrated waveguides (SIWs) to substrate-mounted waveguides (SMWs) mounted on top and/or at the bottom of the substrate. In [14], an MMT-based formulation was presented for the electromagnetic characterization of

measuring cells for uniaxial anisotropic materials. [15] used MMT to obtain the generalized scattering properties of cascaded H-plane discontinuity in a rectangular waveguide operating in X-band frequencies. In [16], the mode-coupling theory was used for the analysis of fields in curved and twisted waveguides.

In this work, we present a mathematical formulation of MMT for analyzing discontinuities caused by different medium parameters at straight junctions between waveguide sections and by bends implemented in waveguides forming sections with oblique junctions between them. The fields inside each (straight and longitudinally uniform) waveguide region will be derived through the analytical solutions of Maxwell's equations in cylindrical coordinates. Additionally, a set of coupling integrals will be established to match field continuity along oblique surfaces that connect two circular waveguides, and the corresponding scattering parameters for each waveguide junction will be obtained.

1.2

Scientific Contributions

We propose a mode-matching-based methodology for the electromagnetic analysis of the junction of circular-cross-section waveguides. We will be working with cylindrical homogeneous waveguides, but all the mathematical procedures can be easily adapted for coaxial cables (with an inner concentric conductor) or rectangular structures. We introduce here a formulation able to describe the behavior of fields in curved waveguides using the mode-matching technique.

The scientific contributions of this work are listed below:

- The development of a mathematical formulation using a semi-analytical mode-matching method (MMT) to describe the scattering characteristics of waveguide circular junctions along oblique surfaces;
- The development of an algorithm to obtain the reflection and transmission parameters of oblique waveguide junctions, and the derivations of the corresponding generalized scattering matrix (GSM).

1.3

Dissertation Organization

In Chapter 2, we present the electromagnetic field solution of a uniform cylindrical waveguide. The modal fields and the characteristic equations for the associated eigenvalues are formulated in terms of pure transverse electric (TE) and magnetic (TM) modes.

In Chapter 3, we explore the use of rotation matrices and coordinate conversions to analyze the fields on a surface defined by a junction between two waveguide segments with an angular offset between them. Finally, we present a methodology for applying the mode-matching method to these oblique junctions in order to model curved waveguides.

In Chapter 4, we explore a numerical algorithm implemented in Matlab based on the formulation presented in Chapter 3, and we validate it for the case of straight junctions of homogeneous guides. The results of the algorithm are validated by comparison with those obtained using commercial electromagnetic simulation software, using the finite element method. In addition, the MMT is applied in the modeling of the junctions of straight segments of cylindrical waveguides with different electromagnetic characteristics. Finally, we evaluate the ability of the present methodology to model the scattering parameters of oblique waveguide junctions.

In Chapter 5, we provide final considerations and analyze the most important results obtained in this work, as well as suggest future research directions.

2

Electromagnetic Fields in Cylindrical Waveguides

2.1

Introduction

Cylindrical transmission lines, such as coaxial cables and circular waveguides, are widely used in telecommunication systems due to their easy machinability and uniform cross-sectional profile. Examples of cylindrical transmission lines are shown in Fig. 2.1. These structures are suitable for long-distance communications.

Homogeneous cylindrical structures can support several field configurations, including TE, TM, and Hybrid modes. However, for communication applications, single-mode waveguides are typically used, where the entire field propagation can be characterized by the *fundamental mode*. In this configuration, all modes except the fundamental one can be discarded, as they are evanescent fields and mostly disappear along the waveguide. While this practice is sufficient for studying fundamental mode propagation, we cannot ignore the higher order modes when studying field distributions near oblique junctions or other waveguide discontinuities.

This chapter presents the mathematical formulation for representing electromagnetic fields inside a uniform circular waveguide. Initially, cylindrical coordinates are used to solve boundary problems involving structures with this particular shape. As we focus on circular waveguides, it is convenient to express the fields in a cylindrical coordinate system. Later, we also use the rectangular coordinate system and require vector transformations from rectangular-to-cylindrical, as described in [2, App. 7]. The coordinate systems



Figure 2.1: Cylindrical waveguides. [1]

used in this work are depicted in Fig. 2.2.

Various techniques can be used to solve the cylindrical boundary problem. For example, direct numerical integration, as used in [17], and perturbation methods, as described in [18], can be employed to approximate solutions to the wave equation. In our approach, we start with Maxwell's Equations to obtain solutions for the TE and TM fields in a sourceless, homogeneous circular waveguide. This allows us to use the MMT in specific situations and compare the expected solutions.

2.2 Circular Wave functions

Maxwell's equations for a source-free, homogeneous, isotropic, and linear medium can be written as follows:

$$\nabla \times \mathbf{E} = -\tilde{z} \mathbf{H} \quad (2-1)$$

$$\nabla \times \mathbf{H} = \tilde{y} \mathbf{E} \quad (2-2)$$

$$\nabla \cdot \mathbf{E} = 0 \quad (2-3)$$

$$\nabla \cdot \mathbf{H} = 0, \quad (2-4)$$

where $\tilde{z} = j\omega\tilde{\mu}$ and $\tilde{y} = (\tilde{\sigma} + j\omega\tilde{\epsilon})$. The complex permeability and complex permittivity are given by $\tilde{\mu}$ and $\tilde{\epsilon}$, respectively. At this work, the time-harmonic dependence in the form $e^{-i\omega t}$ is assumed and omitted. Since we are working at a homogeneous and isotropic medium, $\tilde{\mu}$ and $\tilde{\epsilon}$ are not dependent from position, they are scalar and independent from \mathbf{E} and \mathbf{H} . Applying the curl operator in (2-1) we can obtain:

$$\nabla \times \nabla \times \mathbf{E} = -\tilde{z} \nabla \times \mathbf{H} \quad (2-5)$$

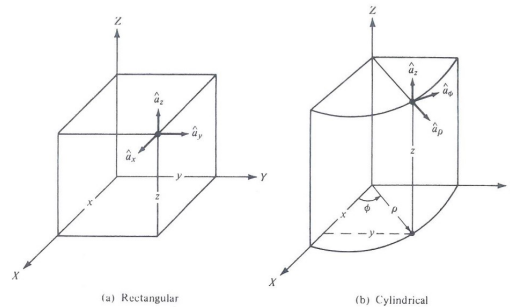


Figure 2.2: Rectangular and Cylindrical coordinate systems. [2]

Using (2-2), we can replace $\nabla \times \mathbf{H}$ and obtain a vector Helmholtz equation for the electric field as

$$\nabla \times \nabla \times \mathbf{E} - k^2 \mathbf{E} = \mathbf{0}, \quad (2-6)$$

where k is the wavenumber defined by $k = \sqrt{-\tilde{z}\tilde{y}}$. Applying the same procedures to (2-2), we can obtain:

$$\nabla \times \nabla \times \mathbf{H} - k^2 \mathbf{H} = \mathbf{0}. \quad (2-7)$$

From (2-3) and (2-4), we know that the divergence of electric and magnetic fields are null. Since we have the vector identity $\nabla \cdot (\nabla \times \mathbf{A}) = 0$, we can define auxiliary vector potentials such that

$$-\nabla \times \mathbf{F} = \mathbf{E} \quad (2-8)$$

$$\nabla \times \mathbf{A} = \mathbf{H}. \quad (2-9)$$

For completeness, we can scalar potentials in view of the Lorenz gauge, i.e.,

$$\nabla \cdot \mathbf{F} = -\tilde{z}\Phi^f \quad (2-10)$$

$$\nabla \cdot \mathbf{A} = -\tilde{y}\Phi^a \quad (2-11)$$

where Φ^f and Φ^a are arbitrary scalar functions. Replacing (2-8) and (2-9) in (2-1) and (2-2), respectively, it is possible to write the following relations between the fields and the vector potentials:

$$\mathbf{E} = \frac{1}{\tilde{y}} \nabla \times \nabla \times \mathbf{A} \quad (2-12)$$

$$\mathbf{H} = \frac{1}{\tilde{x}} \nabla \times \nabla \times \mathbf{F}. \quad (2-13)$$

We can now represent the total fields, express in terms of a superposition from the vector potentials \mathbf{A} and \mathbf{F} :

$$\mathbf{E} = -\nabla \times \mathbf{F} + \frac{1}{\tilde{y}} \nabla \times \nabla \times \mathbf{A} \quad (2-14)$$

$$\mathbf{H} = \nabla \times \mathbf{A} + \frac{1}{\tilde{x}} \nabla \times \nabla \times \mathbf{F} \quad (2-15)$$

Accordingly, (2-6) and (2-7) can be written in terms of potentials [19,

Ch. 3]:

$$\nabla \times \nabla \times \mathbf{F} - k^2 \mathbf{F} = -\tilde{z} \nabla \Phi^f \quad (2-16)$$

$$\nabla \times \nabla \times \mathbf{A} - k^2 \mathbf{A} = -\tilde{y} \nabla \Phi^a. \quad (2-17)$$

Using the vector identity $\nabla \times \nabla \times \mathbf{A} = \nabla(\nabla \cdot \mathbf{A}) - \nabla^2 \mathbf{A}$ we can reduce the general equations to the following wave potentials:

$$\nabla^2 \mathbf{F} - k^2 \mathbf{F} = 0 \quad (2-18)$$

$$\nabla^2 \mathbf{A} - k^2 \mathbf{A} = 0 \quad (2-19)$$

where the solutions to these equations are called *wave potentials*. If we consider a cylindrical waveguide with circular cross section align with \hat{z} direction, as depicted in Fig. 2.3, we can take some particular choices for \mathbf{A} and \mathbf{F} as:

$$\mathbf{A} = \hat{z} \psi^a \quad (2-20)$$

$$\mathbf{F} = \hat{z} \psi^f \quad (2-21)$$

where ψ^a and ψ^f are solutions for equations (2-18) and (2-19). For a particular case where $\mathbf{A} = \hat{z} \psi^a$ and $\mathbf{F} = \mathbf{0}$, (2-15) show us that the magnetic field will not have the H_z component, characteristic of a *transverse magnetic to z* (TM^z) field. Similarly, for electric field, the particular case $\mathbf{F} = \hat{z} \psi^f$ and $\mathbf{A} = \mathbf{0}$ lead us to a field with no E_z component, and characterizes a *transverse electric to z* (TE^z) field.

Assuming that, in cylindrical coordinates, $\psi = \{\psi^a, \psi^f\}$ will have solutions according to:

$$\psi = R(\rho)\Phi(\phi)Z(z). \quad (2-22)$$

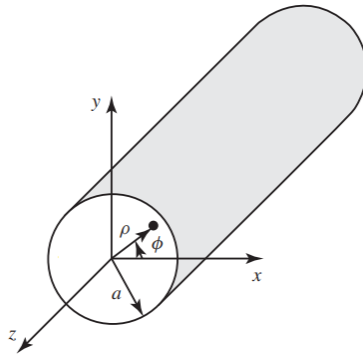


Figure 2.3: Cylindrical waveguide in \hat{z} direction [2]

We can now solve (2-18) and (2-19) in view of the unified scalar Helmholtz equation:

$$\nabla^2\psi - k^2\psi = 0, \quad (2-23)$$

where the Laplacian operator, in cylindrical coordinates, can be write as

$$\frac{1}{\rho} \frac{\partial}{\partial \rho} \left(\rho \frac{\partial \psi}{\partial \rho} \right) + \frac{1}{\rho^2} \frac{\partial^2 \psi}{\partial \phi^2} + \frac{\partial^2 \psi}{\partial z^2} + k^2 \psi = 0. \quad (2-24)$$

By multiplying the above by $1/\psi$, replacing the value of ψ from (2-22) and applying the method of separation of variables, it is possible to write

$$\frac{1}{\rho R} \frac{d}{d\rho} \left(\rho \frac{dR}{d\rho} \right) + \frac{1}{\rho^2 \Phi} \frac{d^2 \Phi}{d\phi^2} + \frac{1}{Z} \frac{d^2 Z}{dz^2} + k^2 = 0, \quad (2-25)$$

where the third term it not dependent of ρ and ϕ . Also, the equation must be null for all values of ρ , ϕ and z , so this term must be independent of z too. Accordingly, we can define a constant k_z such as

$$\frac{1}{Z} \frac{d^2 Z}{dz^2} = -k_z^2. \quad (2-26)$$

Making the above substitution in (2-25) and taking the produt with ρ^2 we obtain

$$\frac{\rho}{R} \frac{d}{d\rho} \left(\rho \frac{dR}{d\rho} \right) + \frac{1}{\Phi} \frac{d^2 \Phi}{d\phi^2} + (k^2 - k_z^2) \rho^2 = 0. \quad (2-27)$$

Now we have the second term of the equation as a function that is not dependent from ρ and z , and all other terms are independent from ϕ . Again, since the equation must be null for all values of ρ , ϕ and z , we can pose a solution as

$$\frac{1}{\Phi} \frac{d^2 \Phi}{d\phi^2} = -n^2 \quad (2-28)$$

where n is a constant. We can rewrite (2-27) as

$$\frac{\rho}{R} \frac{d}{d\rho} \left(\rho \frac{dR}{d\rho} \right) - n^2 + (k^2 - k_z^2) \rho^2 = 0. \quad (2-29)$$

The original second order differential Helmholtz equation in terms of

(ρ, ϕ, z) was spitted into three ordinary equations:

$$\rho \frac{d}{d\rho} \left(\rho \frac{dR}{d\rho} \right) + [(k_\rho \rho)^2 - n^2]R = 0 \quad (2-30)$$

$$\frac{d^2\Phi}{d\phi^2} + n^2\Phi = 0 \quad (2-31)$$

$$\frac{d^2Z}{dz^2} + k_z^2 Z = 0, \quad (2-32)$$

where $k_\rho^2 = k^2 - k_z^2$. Equation (2-30) is a Bessel equation of order n , with the general solution given by the linear combination of Bessel and Hankel functions of first kind, i.e., $J_n(k_\rho \rho)$ and $H_n(k_\rho \rho)$, respectively. According to the analyzed problem, the solution can be given by one of these functions, or by a linear combination of them. At this work, considering all the characteristics of the problem, we will work with a solution given by $J_n(k_\rho \rho)$ since the origin $\rho = 0$ is inside the domain of interest. Equations (2-31) and (2-32) have harmonic functions as a solution, where the general solution was chosen by the problem analyzed. We will consider the elementary wave function in the form

$$\psi_{k_\rho, n, k_z} = J_n(k_\rho \rho) e^{in\phi} e^{ik_z z} \quad (2-33)$$

and the final solution for the Helmholtz equation is given by a linear combination of all elementary wave functions that attend as a solution for the problem. We can sum over all possible values of n and k_ρ (or k_z). For example, we can write

$$\psi = \sum_n \sum_{k_\rho} A_{n, k_\rho} J_n(k_\rho \rho) e^{in\phi} e^{ik_z z} \quad (2-34)$$

where the A_{n, k_ρ} are the constants associated to a particular $\{n, k_\rho\}$ solution.

Now, the solution ψ is known, we can calculate the value of the field components replacing equations (2-20) and (2-21) in (2-14) and (2-15). Letting $\mathbf{A} = \hat{z}\psi$ and $\mathbf{F} = \mathbf{0}$, TM^z fields are given by [19, p. 202]:

$$\begin{aligned} E_\rho &= \frac{1}{y} \frac{\partial^2 \psi}{\partial \rho \partial z} & H_\rho &= \frac{1}{\rho} \frac{\partial \psi}{\partial \phi} \\ E_\phi &= \frac{1}{y\rho} \frac{\partial^2 \psi}{\partial \phi \partial z} & H_\phi &= -\frac{\partial \psi}{\partial \rho} \\ E_z &= \frac{1}{y} \left(\frac{\partial^2}{\partial z^2} + k^2 \right) \psi & H_z &= 0. \end{aligned} \quad (2-35)$$

Similarly, we can obtain a TE^z field by letting $\mathbf{F} = \hat{z}\psi$ and $\mathbf{A} = \mathbf{0}$ where,

according to [19, p. 202], we have:

$$\begin{aligned}
 E_\rho &= -\frac{1}{\rho} \frac{\partial \psi}{\partial \phi} & H_\rho &= \frac{1}{z} \frac{\partial^2 \psi}{\partial \rho \partial z} \\
 E_\phi &= \frac{\partial \psi}{\partial \rho} & H_\phi &= \frac{1}{z\rho} \frac{\partial^2 \psi}{\partial \phi \partial z} \\
 E_z &= 0 & H_z &= \frac{1}{z} \left(\frac{\partial^2}{\partial z^2} + k^2 \right) \psi.
 \end{aligned} \tag{2-36}$$

2.3

Propagation Modes in Circular Waveguide

We can use the cylindrical wave functions, as described in above section, to study the propagation of waves in a hollow circular waveguide. Considering the waveguide depicted in Fig. 2.3, where the field is finite at $\rho = 0$, and the wave function given by (2-33). Assuming that the radial walls that truncate the circular waveguide are *Perfect electric Conductor* (PEC), we need to impose that the tangential electric field is null at the waveguide walls, i.e.,

$$\hat{n} \times \mathbf{E} = \mathbf{0}, \quad \text{at PEC}, \tag{2-37}$$

where \hat{n} is the unit vector that is orthogonal to the PEC wall. So, once we are working with a waveguide a longitudinal axis with the z -orientation, we can force that the components E_z and E_ϕ are null at $\rho = a$.

Now, for TM^z modes, we can express the fields in terms of \mathbf{A} having only a z component ψ , where this field is found from equations (2-35) applied to (2-33). The E_z and E_ϕ components are given by

$$E_z = \frac{1}{\tilde{y}} \left(\frac{\partial^2}{\partial z^2} + k^2 \right) \psi \tag{2-38}$$

$$E_\phi = \frac{1}{\tilde{y}\rho} \frac{\partial^2 \psi}{\partial \phi \partial z} \tag{2-39}$$

if we want then to vanish them at $\rho = a$, the wave function must be null. We can observe that the only component at the wave function who depends from ρ is the Bessel function $J_n(k_\rho \rho)$. Hence, we obtain the characteristic equation

$$J_n(k_\rho a) = 0 \tag{2-40}$$

from which eigenvalues for k_ρ may be determined. The Bessel functions $J_n(x)$ are show at [19, Appendix. D], where we can observe that for each n there are an infinite number of zeros. These are ordered and designated by x_{np} , with n

referring to the order of the Bessel function and p to the order in which the zero appears. Table 2.1 shows the firsts x_{np} .

The equations (2-40) is satisfied if we choose

$$k_\rho = \frac{x_{np}}{a} \quad (2-41)$$

Substituting the above into (2-33), we have the TM_{np} mode functions

$$\psi_{np}^{TM} = J_n\left(\frac{x_{np}\rho}{a}\right) e^{in\phi} e^{ik_z z} \quad (2-42)$$

where $n = 0, 1, 2, \dots$, and $p = 1, 2, 3, \dots$. In view of (2-30), the longitudinal wavenumber k_z is determinate according to

$$\left(\frac{x_{np}}{a}\right)^2 + k_z^2 = k^2 \quad (2-43)$$

The *cutoff wave number* of the np mode is that for which the mode propagation constant vanishes, i.e., $k_z = 0$, and we can define as

$$(k_c)_{np}^{TM} = \frac{x_{np}}{a}. \quad (2-44)$$

If $k > k_c$, the mode propagates, otherwise, if $k < k_c$ the mode is bellow the cutoff and is said evanescent. Letting $k_c = 2\pi f_c \sqrt{\epsilon\mu}$, we obtain the cutoff frequency as

$$(f_c)_{np}^{TM} = \frac{x_{np}}{2\pi a \sqrt{\epsilon\mu}} \quad (2-45)$$

or, setting $k_c = \frac{2\pi}{\lambda_c}$, we obtain the cutoff wavelength as

$$(\lambda_c)_{np}^{TM} = \frac{2\pi a}{x_{np}} \quad (2-46)$$

We observe that the cutoff frequencies are proportional to the x_{np} for TM modes.

Using the same logic for TE^z modes, we can calculate the fields in terms

Table 2.1: Ordered zeros x_{np} of $J_n(x)$.

$p \setminus n$	0	1	2	3	4	5
1	2.405	3.832	5.136	6.380	7.588	8.771
2	5.520	7.016	8.417	9.761	11.065	12.339
3	8.654	10.173	11.620	13.015	14.372	15.700
4	11.792	13.324	14.796	15.700	17.616	18.980

of \mathbf{F} having only a non-null z -component potential ψ . Since E_z is null for TE modes, we need to analyze E_ϕ component, given in (2-33), namely:

$$E_\phi = \frac{\partial\psi}{\partial\rho} \quad (2-47)$$

To vanish the E_ϕ component at $\rho = a$, we must satisfy the condition

$$J'_n(k_\rho a) = 0. \quad (2-48)$$

As well as $J_n(x)$, $J'_n(x)$ is a oscillatory functions, with an infinite number of zeros denoted as x'_{np} . The lower order zeros are present in Table 2.2. Accordingly, the radial wave number is given by

$$k_\rho = \frac{x'_{np}}{a} \quad (2-49)$$

By substituting the above into (2-33), we have the TE_{np} wave potentials given by

$$\psi_{np}^{TE} = J_n\left(\frac{x'_{np}\rho}{a}\right) e^{in\phi} e^{ik_z z}. \quad (2-50)$$

The associated longitudinal wavenumber k_z is given by

$$\left(\frac{x'_{np}}{a}\right)^2 + k_z^2 = k^2. \quad (2-51)$$

Also, the *cutoff wave number* of the np mode is given by

$$(k_c)_{np}^{TE} = \frac{x'_{np}}{a}. \quad (2-52)$$

As before, if $k > k_c$ the mode propagate, and if $k < k_c$ the mode is evanescent. We can also obtain the cutoff frequencies via

$$(f_c)_{np}^{TE} = \frac{x'_{np}}{2\pi a \sqrt{\epsilon\mu}}, \quad (2-53)$$

Table 2.2: Ordered zeros x'_{np} of $J'_n(x)$.

$p \setminus n$	0	1	2	3	4	5
1	3.832	1.841	3.054	4.201	5.317	6.416
2	7.016	5.331	6.706	8.015	9.282	10.520
3	10.173	8.536	9.969	11.346	12.682	13.987
4	13.324	11.706	13.170	14.585	15.964	17.312

and the cutoff wavelength

$$(\lambda_c)_{np}^{TE} = \frac{2\pi a}{x_{np'}}. \quad (2-54)$$

We can observe that the cutoff frequencies are proportional to x'_{np} in the TE configuration.

Taking zeros of Tables 2.1 and 2.2 in ascending order of magnitude, we can observe that the modes in order of ascending cutoff frequencies are TE_{11} , TM_{01} , TE_{21} , TM_{11} , TE_{01} , etc. Some mode patterns of lower order modes are depicted in Fig. 2.4. It is apparent that the cutoff frequencies of the TE_{0n} and TM_{1n} modes are identical; therefore, they are referred as degenerate modes. We also observe that, except for degenerate modes, TE and TM modes have different cutoff frequencies and hence different propagation constants.

As previously mentioned, we will utilize lower order modes to model a problem involving a discontinuity caused by a bent circular waveguide. Initially, we will characterize the problem with an oblique junction that connects two sections of circular waveguide. Subsequently, we will apply the matching mode technique to analyze the interactions between the modes.

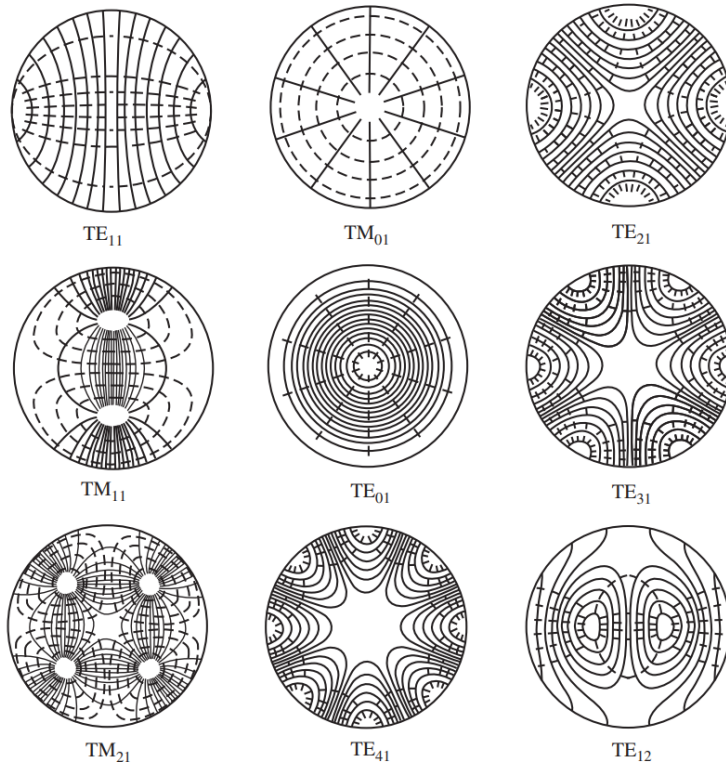


Figure 2.4: Fields configuration of first 9 lower order modes. [2]

3

Mode-Matching Technique Along Oblique Junctions

3.1

Introduction

This chapter presents the formulation of the mode-matching technique (MMT) for modeling the junctions of circular waveguides along an oblique plane. The study of discontinuities in waveguides is a prevalent topic in microwave engineering because any interruption in the uniformity of a waveguide leads to impedance mismatch. This results in a set of reflections that reduce the performance of the propagation of guided modes, specifically at the junctions formed. However, this effect can be exploited positively to design some guided devices, such as filters, couplers, transformers, etc. Therefore, overcoming and controlling scattering in bends has been of significant interest over the years.

Since discontinuities involve a sudden change in the boundary conditions of the waveguide, it is essential to use an appropriate methodology to deal with the physical characteristics of the problem. Over the years, several studies have investigated discontinuities in waveguide junctions using different techniques. For example, in [20], a metagrating-inspired semi-analytical methodology is employed to eliminate reflections in waveguide bends. In [5], a mode-matching approach is utilized to analyze the electric field in a bend parallel-plate waveguide. In [21], the finite element method (FEM) is used to study transitions between coaxial lines. Moreover, in [22], the FEM is applied to study waveguide discontinuities caused by junctions.

We can observe that there are several numerical methods used to handle with various types of discontinuity problems. However, most of them lead to a high cost of computational processing, according to the complexity of the problem. To contour this high cost of processing problem, we need to explore reliable approaches based on semi-analytic methods.

The mode-matching technique (MMT) involves matching the eigenmodes of each region at the junction discontinuity to satisfy the boundary conditions [23]. The MMT is then used to obtain the generalized scattering matrix (GSM) at every discontinuity. By cascading the GSM matrices, we

can determine the equivalent GSM matrix for an entire structure of interest. Therefore, to analyze waveguide discontinuities, the GSM representation will be employed to capture the coupling between adjacent sections of waveguides. Fig. 3.1 shows an example of two adjacent sections of a coaxial waveguide with a longitudinal step discontinuity between regions defined as 1 and 2. Here, \bar{a}_1^+ and \bar{a}_1^- indicate the amplitudes of the forward and backward propagation modes, respectively, from region 1. The same notation is used for \bar{a}_2^+ and \bar{a}_2^- from region 2. This sub-domain decomposition allows us to obtain a low-cost computational method through a robust form, because the associated GSM matrices are inherently stable.

In this chapter, we present a MMT-based method that will be used to analyze homogeneous circular waveguides with bends represented by oblique junctions. The methodology presented herein is inspired by recent works in [24–26].

3.2 MMT Formulation

In this chapter, we will consider the coupling of two straight circular waveguides over a tilted plane described by the angle θ . This common coupling surface will serve as the junction where MMT will be implemented to study the discontinuity caused by the angular displacement. First, we will obtain the GSM matrix at the junction. Then, we will calculate the GSM matrix of a smooth waveguide for regions 1 and 2. To obtain the complete GSM matrix for the entire structure, we need to progressively cascade the GSM matrix of the discontinuity and the smooth waveguide GSM. Finally, with the complete

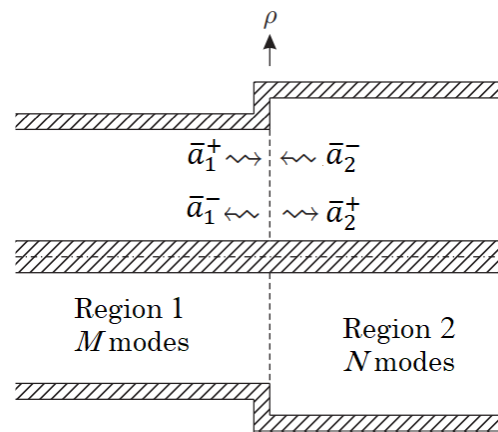


Figure 3.1: Representation of transmitted and reflected waves at a coaxial waveguide discontinuity.

GSM matrix, we can compare the amplitudes of guided modes between the first and last parts of the waveguide analyzed.

3.3 Waveguides with Oblique Junction

Considering a circular waveguide represented in the Cartesian coordinates (x_1, y_1, z_1) , and align with the longitudinal direction, according depicted in Fig. 3.2. We can represent a curve in any point of this structure just defining the center of the coordinate system at the chosen point and applying a rotation at one or more of your axis. We will analyze curvatures by coupling strait waveguides along a oblique plane. In view of that, we first consider the rotation of the initial coordinate system around at y_1 -axis. According to [27], we can use the rotation matrix $\bar{\bar{R}}_{y,\theta}$ to express an angular displacement of θ degrees around y -axis, given by

$$\bar{\bar{R}}_{y,\theta} = \begin{bmatrix} \cos(\theta) & 0 & -\sin(\theta) \\ 0 & 1 & 0 \\ \sin(\theta) & 0 & \cos(\theta) \end{bmatrix}. \quad (3-1)$$

Considering the coordinate system express in Fig. 3.2, when we implement a curvature at the waveguide, that is align with the z_1 -axis, by taking one single rotation of θ_{12} around the y_1 -axis, we obtain a second coordinate system defined by (x_J, y_J, z_J) , where the junction surface between regions 1 and 2 will be define. Again, if we apply another single rotation of θ_{12} around the y_j -axis, we now will get a third coordinate system defined by (x_2, y_2, z_2) , that will be related to the waveguide at region 2. The Fig. 3.3 represent the problem described. We can now relate the three coordinate systems using

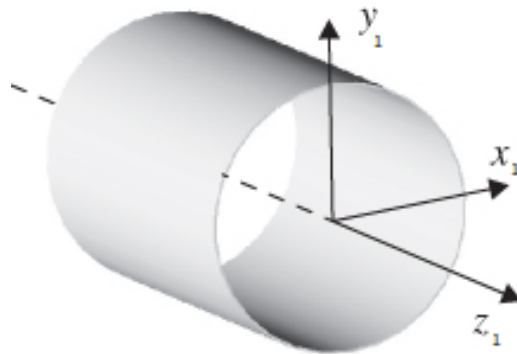


Figure 3.2: Uniform circular waveguide with the longitudinal axis align with the z -axis.

rotation matrices as

$$\begin{bmatrix} x_J \\ y_J \\ z_J \end{bmatrix} = \begin{bmatrix} \cos(\theta_{12}) & 0 & -\sin(\theta_{12}) \\ 0 & 1 & 0 \\ \sin(\theta_{12}) & 0 & \cos(\theta_{12}) \end{bmatrix} \begin{bmatrix} x_1 \\ y_1 \\ z_1 \end{bmatrix} \quad (3-2)$$

$$\begin{bmatrix} x_2 \\ y_2 \\ z_2 \end{bmatrix} = \begin{bmatrix} \cos(\theta_{12}) & 0 & -\sin(\theta_{12}) \\ 0 & 1 & 0 \\ \sin(\theta_{12}) & 0 & \cos(\theta_{12}) \end{bmatrix} \begin{bmatrix} x_J \\ y_J \\ z_J \end{bmatrix} \quad (3-3)$$

We can see that the plane defined by $z_J = 0$ is the common surface connecting the two regions of the waveguide. The oblique junction, which is common to both regions, is defined as the area S_J located on this plane. Fig. 3.4 illustrates the two sections of a curved waveguide, shifted by an angle of $\theta = 2, \theta_{12}$, as well as the oblique junction that connects the two regions.

Since we will work with a junction located at the $z_j = 0$ plan, in order to make easier the mathematics involved at the problem, we can express the regions 1 and 2, with coordinates (x_1, y_1, z_1) and (x_2, y_2, z_2) , respectively, as their projections in $z_J = 0$ plan, at the (x_J, y_J, z_J) coordinate system. This can be achieved using the rotation matrix $\bar{\bar{R}}_{y,\theta}$, in the form:

$$\begin{bmatrix} x_1 \\ y_1 \\ z_1 \end{bmatrix} = \bar{\bar{R}}_{y,\theta}^{-1} \begin{bmatrix} x_J \\ y_J \\ z_J \end{bmatrix} \quad (3-4)$$

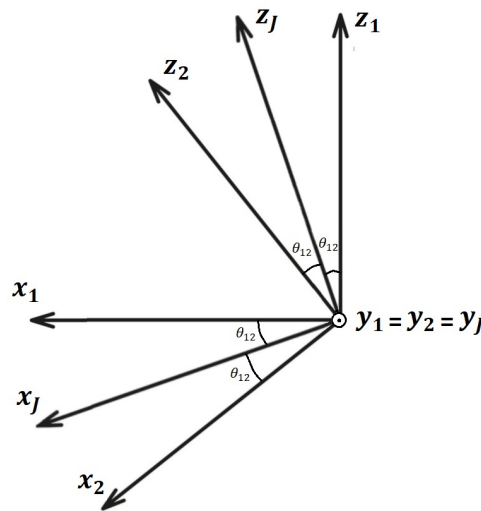


Figure 3.3: View of (x_1, y_1, z_1) and (x_2, y_2, z_2) coordinate systems.

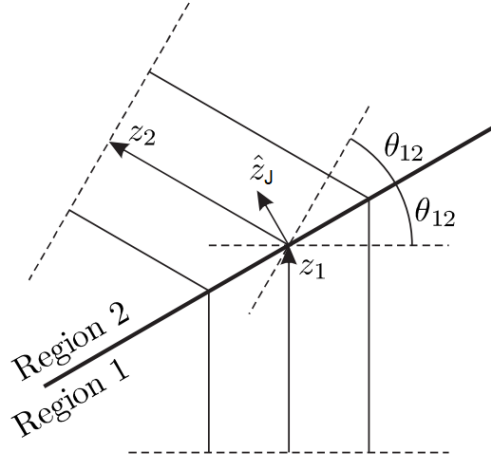


Figure 3.4: Junction of two straight waveguides along a oblique surface described by the tilt angle θ_{12} .

$$\begin{bmatrix} x_2 \\ y_2 \\ z_2 \end{bmatrix} = \bar{\bar{R}}_{y,\theta} \begin{bmatrix} x_J \\ y_J \\ z_J \end{bmatrix} \quad (3-5)$$

where,

$$\bar{\bar{R}}_{y,\theta}^{-1} = \begin{bmatrix} \cos(\theta_{12}) & 0 & \sin(\theta_{12}) \\ 0 & 1 & 0 \\ -\sin(\theta_{12}) & 0 & \cos(\theta_{12}) \end{bmatrix} \quad (3-6)$$

Based on equations (3-4) and (3-5), we can express the unit vector of coordinate systems 1 and 2 as their projections at the oblique junction S_J in the form:

$$\hat{x}_1 = \cos(\theta_{12})\hat{x}_J + \sin(\theta_{12})\hat{z}_J \quad (3-7)$$

$$\hat{y}_1 = \hat{y}_J \quad (3-8)$$

$$\hat{z}_1 = -\sin(\theta_{12})\hat{x}_J + \cos(\theta_{12})\hat{z}_J \quad (3-9)$$

and,

$$\hat{x}_2 = \cos(\theta_{12})\hat{x}_J - \sin(\theta_{12})\hat{z}_J \quad (3-10)$$

$$\hat{y}_2 = \hat{y}_J \quad (3-11)$$

$$\hat{z}_2 = \sin(\theta_{12})\hat{x}_J + \cos(\theta_{12})\hat{z}_J \quad (3-12)$$

The equations of propagating electric and magnetic fields for the waveg-

uide regions 1 and 2, can be written as

$$\mathbf{E}_1 = \sum_p^{\infty} a_{1,p}^+ e^{ik_{1z,p}z_1} \mathbf{E}_{1,p}^+ + a_{1,p}^- e^{-ik_{1z,p}z_1} \mathbf{E}_{1,p}^- \quad (3-13)$$

$$\mathbf{H}_1 = \sum_p^{\infty} a_{1,p}^+ e^{ik_{1z,p}z_1} \mathbf{H}_{1,p}^+ + a_{1,p}^- e^{-ik_{1z,p}z_1} \mathbf{H}_{1,p}^- \quad (3-14)$$

$$\mathbf{E}_2 = \sum_p^{\infty} a_{2,p}^+ e^{ik_{2z,p}z_2} \mathbf{E}_{2,p}^+ + a_{2,p}^- e^{-ik_{2z,p}z_2} \mathbf{E}_{2,p}^- \quad (3-15)$$

$$\mathbf{H}_2 = \sum_p^{\infty} a_{2,p}^+ e^{ik_{2z,p}z_2} \mathbf{H}_{2,p}^+ + a_{2,p}^- e^{-ik_{2z,p}z_2} \mathbf{H}_{2,p}^- \quad (3-16)$$

where the 1 and 2 index refer to the waveguides fields and characteristics of regions. Also, the p th modal field is given by:

$$\mathbf{E}_{i,p}^{\pm} = E_{ix,p} \hat{x}_i + E_{iy,p} \hat{y}_i \pm E_{iz,p} \hat{z}_i \quad (3-17)$$

$$\mathbf{H}_{i,p}^{\pm} = \pm H_{ix,p} \hat{x}_i \pm H_{iy,p} \hat{y}_i + H_{iz,p} \hat{z}_i \quad (3-18)$$

where $i = \{1, 2\}$.

Taking the relations between the coordinates from regions 1 and 2 and the coordinates from the region of the oblique junctions, as seen in equations (3-7) to (3-12), and replacing at the coordinates in (3-17) and (3-18), we can obtain the equations from electric and magnetic fields from regions 1 and 2 expressed in terms of (x_J, y_J, z_J) coordinate system. Accordingly, we can write:

$$\begin{aligned} \mathbf{E}_{1,p}^{\pm} &= (\cos(\theta_{12}) \hat{x}_J + \sin(\theta_{12}) \hat{z}_J) E_{1x,p} \\ &\quad + \hat{y}_J E_{1y,p} \pm (-\sin(\theta_{12}) \hat{x}_J + \cos(\theta_{12}) \hat{z}_J) E_{1z,p} \end{aligned} \quad (3-19)$$

$$\begin{aligned} \mathbf{H}_{1,p}^{\pm} &= \pm(\cos(\theta_{12}) \hat{x}_J + \sin(\theta_{12}) \hat{z}_J) H_{1x,p} \\ &\quad \pm \hat{y}_J H_{1y,p} + (-\sin(\theta_{12}) \hat{x}_J + \cos(\theta_{12}) \hat{z}_J) H_{1z,p} \end{aligned} \quad (3-20)$$

$$\begin{aligned} \mathbf{E}_{2,p}^{\pm} &= (\cos(\theta_{12}) \hat{x}_J - \sin(\theta_{12}) \hat{z}_J) E_{2x,p} \\ &\quad + \hat{y}_J E_{2y,p} \pm (\sin(\theta_{12}) \hat{x}_J + \cos(\theta_{12}) \hat{z}_J) E_{2z,p} \end{aligned} \quad (3-21)$$

$$\begin{aligned} \mathbf{H}_{2,p}^{\pm} &= \pm(\cos(\theta_{12}) \hat{x}_J - \sin(\theta_{12}) \hat{z}_J) H_{2x,p} \\ &\quad \pm \hat{y}_J H_{2y,p} + (\sin(\theta_{12}) \hat{x}_J + \cos(\theta_{12}) \hat{z}_J) H_{2z,p}. \end{aligned} \quad (3-22)$$

Rearranging the terms according to coordinates x_J , y_J and z_J , we have:

$$\begin{aligned} \mathbf{E}_{1,p}^{\pm} &= (\cos(\theta_{12})E_{1x,p} \mp \sin(\theta_{12})E_{1z,p}) \hat{x}_J \\ &\quad + E_{1y,p} \hat{y}_J \pm (\cos(\theta_{12})E_{1z,p} \pm \sin(\theta_{12})E_{1x,p}) \hat{z}_J \end{aligned} \quad (3-23)$$

$$\begin{aligned} \mathbf{H}_{1,p}^{\pm} &= \pm(\cos(\theta_{12})H_{1x,p} \mp \sin(\theta_{12})H_{1z,p}) \hat{x}_J \\ &\quad \pm H_{1y,p} \hat{y}_J + (\cos(\theta_{12})H_{1z,p} \pm \sin(\theta_{12})H_{1x,p}) \hat{z}_J \end{aligned} \quad (3-24)$$

$$\begin{aligned} \mathbf{E}_{2,p}^{\pm} &= (\cos(\theta_{12})E_{2x,p} \pm \sin(\theta_{12})E_{2z,p}) \hat{x}_J \\ &\quad + E_{2y,p} \hat{y}_J \pm (\cos(\theta_{12})E_{2z,p} \mp \sin(\theta_{12})E_{2x,p}) \hat{z}_J \end{aligned} \quad (3-25)$$

$$\begin{aligned} \mathbf{H}_{2,p}^{\pm} &= \pm(\cos(\theta_{12})H_{2x,p} \pm \sin(\theta_{12})H_{2z,p}) \hat{x}_J \\ &\quad \pm H_{2y,p} \hat{y}_J + (\cos(\theta_{12})H_{2z,p} \mp \sin(\theta_{12})H_{2x,p}) \hat{z}_J. \end{aligned} \quad (3-26)$$

After defining the fields at the oblique surface S_J , we can consider a more general situation where the waveguides in regions 1 and 2 have different radii, r_1 and r_2 , respectively, with $r_1 > r_2$. When the cross-sectional sizes of the waveguides are different, we will have a discontinuity defined by a step transition, as shown in Fig. 3.5. Accordingly, from the continuity of the transversal fields at the junction, we must match the fields transversal to z_J such that

$$\left. \begin{aligned} \hat{z}_J \times \mathbf{E}_1 &= \hat{z}_J \times \mathbf{E}_2 \\ \hat{z}_J \times \mathbf{H}_1 &= \hat{z}_J \times \mathbf{H}_2 \end{aligned} \right\} \text{inside } S_J \quad (3-27)$$

$$\hat{z}_J \times \mathbf{E}_1 = \mathbf{0}, \text{ inside } \tilde{S}_1 - S_J \quad (3-28)$$

i.e., we must guarantee that the fields tangential to the interface S_J (transversal to the normal component z_J of S_J) must be equal for both regions of the waveguide. We can observe that, except when $\theta_{12} = 0$, the size from cross section S_J will be different from the size of cross sections S_1 and S_2 , because it will be considering a inclined region common to both waveguide regions. In addition, we can also observe that the inclined surface \tilde{S}_1 will be different from S_1 .

Considering M modes in the region 1 and N modes in the region 2, and taking the equations described at (3-13) to (3-16), we can expand the equations

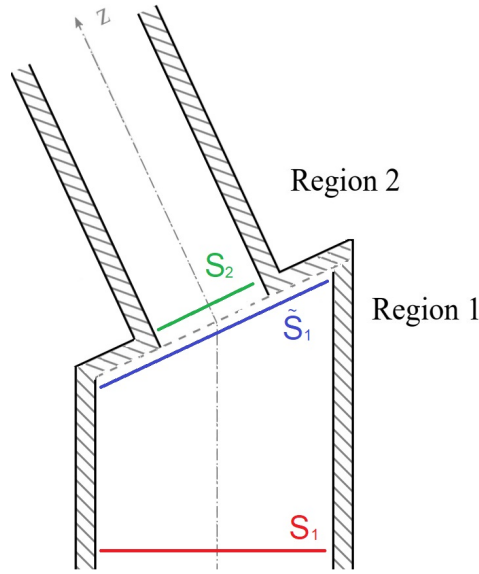


Figure 3.5: Waveguide junctions showing the surfaces S_1 , S_2 , and \tilde{S}_1 .

of (3-27) as

$$\sum_{m=1}^M a_{1,m}^+ e^{ik_{1z,m}z_1} \hat{z}_J \times \mathbf{E}_{1,m}^+ + a_{1,m}^- e^{-ik_{1z,m}z_1} \hat{z}_J \times \mathbf{E}_{1,m}^- = \sum_{n=1}^N a_{2,n}^+ e^{ik_{2z,n}z_2} \hat{z}_J \times \mathbf{E}_{2,n}^+ + a_{2,n}^- e^{-ik_{2z,n}z_2} \hat{z}_J \times \mathbf{E}_{2,n}^- \quad (3-29)$$

$$\sum_{m=1}^M a_{1,m}^+ e^{ik_{1z,m}z_1} \hat{z}_J \times \mathbf{H}_{1,m}^+ + a_{1,m}^- e^{-ik_{1z,m}z_1} \hat{z}_J \times \mathbf{H}_{1,m}^- = \sum_{n=1}^N a_{2,n}^+ e^{ik_{2z,n}z_2} \hat{z}_J \times \mathbf{H}_{2,n}^+ + a_{2,n}^- e^{-ik_{2z,n}z_2} \hat{z}_J \times \mathbf{H}_{2,n}^-. \quad (3-30)$$

The S_J plane was defined with $z_J = 0$, and since we are working exactly at the oblique junction, the following conditions must be considered at the fields equations:

$$z_1 = -x_J \sin(\theta_{12}) \quad (3-31)$$

$$z_2 = x_J \sin(\theta_{12}). \quad (3-32)$$

Taking these values at the exponentials in terms of z_1 and z_2 , we have:

$$e^{ik_{1z,m}z_1} = e^{-ik_{1z,m}x_J \sin(\theta_{12})} \quad (3-33)$$

$$e^{ik_{2z,n}z_2} = e^{ik_{2z,n}x_J \sin(\theta_{12})}. \quad (3-34)$$

Then, equations (3-29) and (3-30) can be rewritten as:

$$\begin{aligned} \sum_{m=1}^M a_{1,m}^+ e^{-ik_{1z,m}x_J \sin(\theta_{12})} \hat{z}_J \times \mathbf{E}_{1,m}^+ + a_{1,m}^- e^{ik_{1z,m}x_J \sin(\theta_{12})} \hat{z}_J \times \mathbf{E}_{1,m}^- = \\ \sum_{n=1}^N a_{2,n}^+ e^{ik_{2z,n}x_J \sin(\theta_{12})} \hat{z}_J \times \mathbf{E}_{2,n}^+ + a_{2,n}^- e^{-ik_{2z,n}x_J \sin(\theta_{12})} \hat{z}_J \times \mathbf{E}_{2,n}^- \end{aligned} \quad (3-35)$$

$$\begin{aligned} \sum_{m=1}^M a_{1,m}^+ e^{-ik_{1z,m}x_J \sin(\theta_{12})} \hat{z}_J \times \mathbf{H}_{1,m}^+ + a_{1,m}^- e^{ik_{1z,m}x_J \sin(\theta_{12})} \hat{z}_J \times \mathbf{H}_{1,m}^- = \\ \sum_{n=1}^N a_{2,n}^+ e^{ik_{2z,n}x_J \sin(\theta_{12})} \hat{z}_J \times \mathbf{H}_{2,n}^+ + a_{2,n}^- e^{-ik_{2z,n}x_J \sin(\theta_{12})} \hat{z}_J \times \mathbf{H}_{2,n}^-. \end{aligned} \quad (3-36)$$

Taking the dot product of the above vector equation with the term $e^{ik_{2z,n'}x_J \sin(\theta_{12})} \mathbf{H}_{2,n'}^+$ (for $n' = 1, 2, 3, \dots, N$) and integrating the result over the cross-section S_J , and employing the vector identity

$$(\hat{n} \times \mathbf{A}_1) \cdot \mathbf{A}_2 = (\mathbf{A}_1 \times \mathbf{A}_2) \cdot \hat{n}, \quad (3-37)$$

we can obtain a set of N equations defined by:

$$\begin{aligned} \sum_{m=1}^M \int \int_{S_J} \left\{ a_{1,m}^+ e^{-i(k_{1z,m} - k_{2z,n'})x_J \sin(\theta_{12})} \left[(\mathbf{E}_{1,m}^+ \times \mathbf{H}_{2,n'}^+) \cdot \hat{z}_J \right] \right. \\ \left. + a_{1,m}^- e^{i(k_{1z,m} + k_{2z,n'})x_J \sin(\theta_{12})} \left[(\mathbf{E}_{1,m}^- \times \mathbf{H}_{2,n'}^+) \cdot \hat{z}_J \right] \right\} dS = \\ \sum_{n=1}^N \int \int_{S_J} \left\{ a_{2,n}^+ e^{i(k_{2z,n} + k_{2z,n'})x_J \sin(\theta_{12})} \left[(\mathbf{E}_{2,n}^+ \times \mathbf{H}_{2,n'}^+) \cdot \hat{z}_J \right] \right. \\ \left. + a_{2,n}^- e^{-i(k_{2z,n} - k_{2z,n'})x_J \sin(\theta_{12})} \left[(\mathbf{E}_{2,n}^- \times \mathbf{H}_{2,n'}^+) \cdot \hat{z}_J \right] \right\} dS. \end{aligned} \quad (3-38)$$

We can now define the following reaction integral

$$X_{i(m)j(n)}^\pm = \int \int_{S_J} e^{\pm iv(k_{iz,m} \pm vk_{jz,n})x_J \sin(\theta_{12})} (\mathbf{E}_{i,m}^\pm \times \mathbf{H}_{j,n}^+) \cdot \hat{z}_J dS, \quad (3-39)$$

with $v = (-1)^{(2-i)}$, and the above can be rewritten in matrix form as

$$\bar{\bar{X}}_{i,j}^\pm |_{n,m} = X_{i(m)j(n)}^\pm. \quad (3-40)$$

Equation (3-38) can be written in a matrix form as

$$\bar{X}_{1,2}^+ \bar{a}_1^+ + \bar{X}_{1,2}^- \bar{a}_1^- = \bar{X}_{2,2}^+ \bar{a}_2^+ + \bar{X}_{2,2}^- \bar{a}_2^- \quad (3-41)$$

where the modal amplitudes were depicted as the column vector

$$\bar{a}_j^\pm |_m = a_{j,m}^\pm. \quad (3-42)$$

Similarly, from the continuity of transversal magnetic field we can find reaction integrals to relate magnetic fields from regions 1 and 2. Taking the dot product of the equation (3-36) with the term $e^{ik_{1z,m'}x_J \sin(\theta_{12})} \mathbf{E}_{1,m'}^+$ (for $m' = 1, 2, 3, \dots, M$) and integrating the result over the cross-section S_J , we can obtain a set of M equations:

$$\begin{aligned} \sum_{m=1}^M \int \int_{S_J} \left\{ a_{1,m}^+ e^{-i(k_{1z,m} - k_{1z,m'})x_J \sin(\theta_{12})} \left[(\mathbf{H}_{1,m}^+ \times \mathbf{E}_{1,m'}^+) \cdot \hat{z}_J \right] \right. \\ \left. + a_{1,m}^- e^{i(k_{1z,m} + k_{1z,m'})x_J \sin(\theta_{12})} \left[(\mathbf{H}_{1,m}^- \times \mathbf{E}_{1,m'}^+) \cdot \hat{z}_J \right] \right\} dS = \\ \sum_{n=1}^N \int \int_{S_2} \left\{ a_{2,n}^+ e^{i(k_{2z,n} + k_{1z,m'})x_J \sin(\theta_{12})} \left[(\mathbf{H}_{2,n}^+ \times \mathbf{E}_{1,m'}^+) \cdot \hat{z}_J \right] \right. \\ \left. + a_{2,n}^- e^{-i(k_{2z,n} - k_{1z,m'})x_J \sin(\theta_{12})} \left[(\mathbf{H}_{2,n}^- \times \mathbf{E}_{1,m'}^+) \cdot \hat{z}_J \right] \right\} dS \quad (3-43) \end{aligned}$$

Now, by applying the following vector identity

$$\mathbf{A} \times \mathbf{B} = -\mathbf{B} \times \mathbf{A}, \quad (3-44)$$

and by introducing the reaction integral

$$Y_{i(m)j(n)}^\pm = \int \int_{S_J} e^{\pm ib(k_{jz,n} \pm bk_{iz,m})x_J \sin(\theta_{12})} \left(\mathbf{E}_{i,m}^+ \times \mathbf{H}_{j,n}^\pm \right) \cdot \hat{z}_J dS \quad (3-45)$$

where $b = (-1)^{(2-j)}$, we can rewrite (3-43) in a matrix form as

$$\bar{Y}_{1,1}^+ \bar{a}_1^+ + \bar{Y}_{1,1}^- \bar{a}_1^- = \bar{Y}_{1,2}^+ \bar{a}_2^+ + \bar{Y}_{1,2}^- \bar{a}_2^-. \quad (3-46)$$

Note that, the modal amplitudes were again depicted as the column vector depicted in (3-42).

3.4 Reaction Integrals

We can note that at the reaction integrals showed in equations (3-39) and (3-45) it is necessary to realize a cross product of the \mathbf{E} field with the \mathbf{H} field at the surface S_J . Considering the fields equations for regions 1 and 2,

taking on the (x_J, y_J, z_J) coordinate system, we can express the cross product as

$$\begin{aligned} (\mathbf{E}_{i,m}^{s_i} \times \mathbf{H}_{j,n}^{s_j}) &= (E_{iy,m}H_{jz,n} - s_i s_j E_{iz,m}H_{jy,n})\hat{x}_J \\ &\quad + (s_i s_j E_{iz,m}H_{jx,n} - E_{ix,m}H_{jz,n})\hat{y}_J \\ &\quad + s_j(E_{ix,m}H_{jy,n} - E_{iy,m}H_{jx,n})\hat{z}_J. \end{aligned} \quad (3-47)$$

Now, taking the dot product of the above equation with the unit vector \hat{z}_J , because of the orthogonality between the unit vector, only the third term will remain. So, we can simplify the above to

$$(\mathbf{E}_{i,m}^{s_i} \times \mathbf{H}_{j,n}^{s_j}) \cdot \hat{z}_J = s_j(E_{ix,m}H_{jy,n} - E_{iy,m}H_{jx,n}), \quad (3-48)$$

where $i = \{1, 2\}$ and $j = \{1, 2\}$ refer to the regions, and $s_i = \{1, -1\}$ and $s_j = \{1, -1\}$ refer to the field propagation direction.

We can rewrite all field components of regions 1 and 2, as their projections in coordinates (x_J, y_J, z_J) , using equations (3-23) to (3-26). Namely:

$$E_{1Jx,p}^\pm = E_{1x,p} \cos(\theta_{12}) \mp E_{1z,p} \sin(\theta_{12}) \quad (3-49)$$

$$H_{1Jx,p}^\pm = H_{1x,p} \cos(\theta_{12}) \mp H_{1z,p} \sin(\theta_{12}) \quad (3-50)$$

$$E_{1Jy,p}^\pm = E_{1y,p} \quad (3-51)$$

$$H_{1Jy,p}^\pm = H_{1y,p} \quad (3-52)$$

$$E_{2Jx,p}^\pm = E_{2x,p} \cos(\theta_{12}) \pm E_{2z,p} \sin(\theta_{12}) \quad (3-53)$$

$$H_{2Jx,p}^\pm = H_{2x,p} \cos(\theta_{12}) \pm H_{2z,p} \sin(\theta_{12}) \quad (3-54)$$

$$E_{2Jy,p}^\pm = E_{2y,p} \quad (3-55)$$

$$H_{2Jy,p}^\pm = H_{2y,p}. \quad (3-56)$$

The above expressions describe the field components in regions 1 and 2, expressed in the Cartesian coordinates of the oblique surface S_J .

Now, we can expand the cross product from (3-48) for all possible combinations of i and j . Accordingly, we obtain

1. for $i = 1$ and $j = 1$:

$$\begin{aligned} (\mathbf{E}_{1,m}^{s_i} \times \mathbf{H}_{1,n}^{s_j}) \cdot \hat{z}_J &= s_j \left\{ [E_{1x,m} \cos(\theta_{12}) - s_i E_{1z,m} \sin(\theta_{12})] H_{1y,n} \right. \\ &\quad \left. - E_{1y,m} [H_{1x,n} \cos(\theta_{12}) - s_j H_{1z,n} \sin(\theta_{12})] \right\} \end{aligned} \quad (3-57)$$

2. For $i = 1$ and $j = 2$:

$$(\mathbf{E}_{1,m}^{s_i} \times \mathbf{H}_{2,n}^{s_j}) \cdot \hat{z}_J = s_j \left\{ [E_{1x,m} \cos(\theta_{12}) - s_i E_{1z,m} \sin(\theta_{12})] H_{2y,n} - E_{1y,m} [H_{2x,p} \cos(\theta_{12}) + s_j H_{2z,p} \sin(\theta_{12})] \right\} \quad (3-58)$$

3. For $i = 2$ and $j = 2$:

$$(\mathbf{E}_{2,m}^{s_i} \times \mathbf{H}_{2,n}^{s_j}) \cdot \hat{z}_J = s_j \left\{ [E_{2x,m} \cos(\theta_{12}) + s_i E_{2z,m} \sin(\theta_{12})] H_{2y,n} - E_{2y,m} [H_{2x,p} \cos(\theta_{12}) + s_j H_{2z,p} \sin(\theta_{12})] \right\} \quad (3-59)$$

Since we are working with cylindrical waveguides, the surface of the oblique plane S_J will be characterized by an ellipse with radius $r_J(\phi, \theta_{12})$, that will be proportional to the radius of region 2 waveguide, the tilt angle θ_{12} and the ϕ angle over the surface, as depicted in Fig. 3.6. In view of that, we can express the fields at this surface in cylindrical coordinates formed by a linear combination of the Cartesian coordinates of the fields. This can be done using transformation matrices. According [2, Appendix 7], we can express the following relations between the fields components:

$$\begin{bmatrix} A_x \\ A_y \\ A_z \end{bmatrix} = \begin{bmatrix} \cos(\phi) & -\sin(\phi) & 0 \\ \sin(\phi) & \cos(\phi) & 0 \\ 0 & 0 & 1 \end{bmatrix} \begin{bmatrix} A_\rho \\ A_\phi \\ A_z \end{bmatrix} \quad (3-60)$$

Using the above relation, the fields on the oblique junction in cylindrical

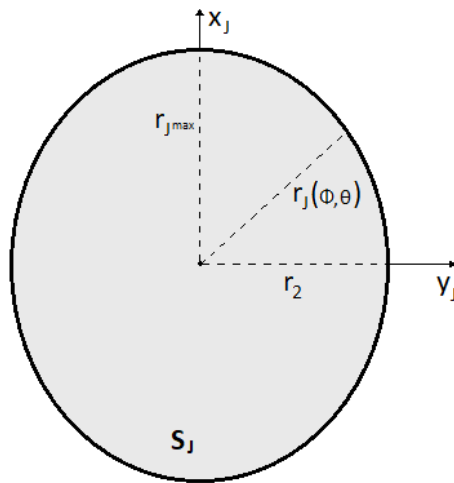


Figure 3.6: View of the S_J surface over the plane $z_J = 0$.

coordinates can be achieved directly as

$$A_{Jx} = A_{J\rho} \cos(\phi_J) - A_{J\phi} \sin(\phi_J) \quad (3-61)$$

$$A_{Jy} = A_{J\rho} \sin(\phi_J) + A_{J\phi} \cos(\phi_J) \quad (3-62)$$

$$A_{Jz} = A_{Jz} \quad (3-63)$$

where $A = \{E, H\}$ when describing electric and magnetic field components.

For the fields from regions 1 and 2, we must define a way to relate the cylindrical coordinates (ρ_1, ϕ_1, z_1) and (ρ_2, ϕ_2, z_2) with their projection at the oblique region S_J , so we can apply the mode-matching technique at our proposed problem.

Considering a position vector on plane $z_J = 0$, that will be define by coordinates $(\rho_J, \phi_J, 0)$, we can convert to cartesian coordinates by

$$x_J = \rho_J \cos(\phi_J) \quad (3-64)$$

$$y_J = \rho_J \sin(\phi_J) \quad (3-65)$$

$$z_J = z_J. \quad (3-66)$$

Now, using the relations depicted in (3-7) to (3-12), we can write the coordinates (x_1, y_1, z_1) and (x_2, y_2, z_2) in the form

$$x_1 = x_J \cos(\theta_{12}) \quad (3-67)$$

$$y_1 = y_J \quad (3-68)$$

$$z_1 = -x_J \sin(\theta_{12}) \quad (3-69)$$

$$x_2 = x_J \cos(\theta_{12}) \quad (3-70)$$

$$y_2 = y_J \quad (3-71)$$

$$z_2 = x_J \sin(\theta_{12}). \quad (3-72)$$

From the above, coordinates (x_1, y_1, z_1) and (x_2, y_2, z_2) , we can calculate the conversion to their cylindrical format (ρ_1, ϕ_1, z_1) and (ρ_2, ϕ_2, z_2) , respectively, that will define the position vector projected at the oblique junction and will make possible the use of mode-matching technique. We have then

$$\rho_i = \sqrt{x_i^2 + y_i^2} \quad (3-73)$$

$$\phi_i = \arctan\left(\frac{y_i}{x_i}\right) \quad (3-74)$$

$$z_i = -x_i \sin(\theta_{12}) \quad (3-75)$$

where $i = \{1, 2\}$. Taking equations (3-64) and (3-65), we can rewrite the above

relations as

$$\rho_1 = \rho_J \sqrt{\cos(\phi_J)^2 \cos(\theta_{12})^2 + \sin(\phi_J)^2} \quad (3-76)$$

$$\phi_1 = \arctan \left(\frac{\sin(\phi_J)}{\cos(\phi_J) \cos(\theta_{12})} \right) \quad (3-77)$$

$$z_1 = -\rho_J \cos(\phi_J) \sin(\theta_{12}) \quad (3-78)$$

$$\rho_2 = \rho_J \sqrt{\cos(\phi_J)^2 \cos(\theta_{12})^2 + \sin(\phi_J)^2} \quad (3-79)$$

$$\phi_2 = \arctan \left(\frac{\sin(\phi_J)}{\cos(\phi_J) \cos(\theta_{12})} \right) \quad (3-80)$$

$$z_2 = \rho_J \cos(\phi_J) \sin(\theta_{12}) \quad (3-81)$$

Then, we can relate a vector with coordinates (ρ_J, ϕ_J, z_J) to their respective vectors from region 1, (ρ_1, ϕ_1, z_1) , and region 2, (ρ_2, ϕ_2, z_2) .

Now we can use the transformation matrix from equation (3-60) to write the values from fields of region 1 that relate to the fields from region 2, on S_J .

$$A_{ix} = A_{i\rho} \cos(\phi_i) - A_{i\phi} \sin(\phi_i) \quad (3-82)$$

$$A_{iy} = A_{i\rho} \sin(\phi_i) + A_{i\phi} \cos(\phi_i) \quad (3-83)$$

$$A_{iz} = A_{iz} \quad (3-84)$$

where $A = E, H$ and $i = \{1, 2\}$.

According equations (39), (50) e (51) from [24, Ch. 3], we can write the following solutions for propagating fields inside a cylindrical waveguide:

1. For TM^z fields:

$$E_{\rho n}(\rho, \phi) = e^{in\phi} \frac{1}{k_\rho^2 \rho} ik_z k_\rho \rho J'_n(k_\rho \rho) \quad (3-85)$$

$$E_{\phi n}(\rho, \phi) = -e^{in\phi} \frac{1}{k_\rho^2 \rho} nk_z J_n(k_\rho \rho) \quad (3-86)$$

$$E_{zn}(\rho, \phi) = e^{in\phi} J_n(k_\rho \rho) \quad (3-87)$$

$$H_{\rho n}(\rho, \phi) = e^{in\phi} \frac{1}{k_\rho^2 \rho} n\omega\epsilon J_n(k_\rho \rho) \quad (3-88)$$

$$H_{\phi n}(\rho, \phi) = e^{in\phi} \frac{1}{k_\rho^2 \rho} i\omega\epsilon k_\rho \rho J'_n(k_\rho \rho) \quad (3-89)$$

$$H_{zn}(\rho, \phi) = 0 \quad (3-90)$$

2. For TE^z fields:

$$E_{\rho n}(\rho, \phi) = -e^{in\phi} \frac{1}{k_\rho^2 \rho} n \omega \mu J_n(k_\rho \rho) \quad (3-91)$$

$$E_{\phi n}(\rho, \phi) = -e^{in\phi} \frac{1}{k_\rho^2 \rho} i \omega \mu k_\rho \rho J'_n(k_\rho \rho) \quad (3-92)$$

$$E_{zn}(\rho, \phi) = 0 \quad (3-93)$$

$$H_{\rho n}(\rho, \phi) = e^{in\phi} \frac{1}{k_\rho^2 \rho} i k_z k_\rho \rho J'_n(k_\rho \rho) \quad (3-94)$$

$$H_{\phi n}(\rho, \phi) = -e^{in\phi} \frac{1}{k_\rho^2 \rho} n k_z J_n(k_\rho \rho) \quad (3-95)$$

$$H_{zn}(\rho, \phi) = e^{in\phi} J_n(k_\rho \rho) \quad (3-96)$$

Based on the above field solutions, we can take equations (3-82)–(3-84) and express the results of the cross products in (3-57)–(3-59) as cylindrical functions. So, the reaction integrals presented in equations (3-39) and (3-45) can be solved via numerical integration over the S_J surface as a function of ρ_J and ϕ_J via

$$\int \int_{S_J} \cdots dS = \int_{\rho_J} \int_{\phi_J} \cdots \rho_J d\rho_J d\phi_J, \quad (3-97)$$

where we have the limits of integration defined by $\phi_J = [0, 2\pi]$ and

$$\rho_J = \left[0, \frac{r_2}{\cos(\theta_{12})} \frac{1}{\sqrt{\cos(\phi_J)^2 + \frac{\sin(\phi_J)^2}{\cos(\theta_{12})^2}}} \right]. \quad (3-98)$$

We can note that, because the elliptical format of the surface S_J , the upper limit of ρ_J is a function of ϕ_J . We cannot found closed-form solution for the reaction integrals.

Finally, after solving the reaction integral, the coupling matrices $\bar{\bar{X}}_{i,j}^\pm$ and $\bar{\bar{Y}}_{i,j}^\pm$ can be filled properly. Such matrices have the dimensions according to the number of modes for each region:

$$\dim(\bar{\bar{X}}_{1,2}^\pm) = (N, M) \quad (3-99)$$

$$\dim(\bar{\bar{X}}_{2,2}^\pm) = (N, N) \quad (3-100)$$

$$\dim(\bar{\bar{Y}}_{1,1}^\pm) = (M, M) \quad (3-101)$$

$$\dim(\bar{\bar{Y}}_{1,2}^\pm) = (M, N). \quad (3-102)$$

3.4.1 Special Case of a Straight Junction

We can study the special case of the junction of two straight waveguides, as depicted in Fig. 3.7 by using the above formulation. For that, we just need to set $\theta_{12} = 0$ into the above equations. First, we can verify that the equations (3-7)-(3-12), with $\theta_{12} = 0$, reduce to

$$\hat{x}_1 = \hat{x}_2 = \hat{x}_J \quad (3-103)$$

$$\hat{y}_1 = \hat{y}_2 = \hat{y}_J \quad (3-104)$$

$$\hat{z}_1 = \hat{z}_2 = \hat{z}_J. \quad (3-105)$$

Accordingly, we can verify that all coordinate systems share the same unit vector directions. To simplify, we will just consider a unified Cartesian system denoted as (x, y, z) .

Also, with $\theta_{12} = 0$, we will simplify some components from equations (3-23)–(3-26), since we have $\cos(\theta_{12}) = 1$ e $\sin(\theta_{12}) = 0$. So, the p th modal fields of regions 1 and 2 can be written as

$$\mathbf{E}_{i,p}^{\pm} = E_{ix,p} \hat{x} + E_{iy,p} \hat{y} \pm E_{iz,p} \hat{z} \quad (3-106)$$

$$\mathbf{H}_{i,p}^{\pm} = \pm H_{ix,p} \hat{x} \pm H_{iy,p} \hat{y} + H_{iz,p} \hat{z}. \quad (3-107)$$

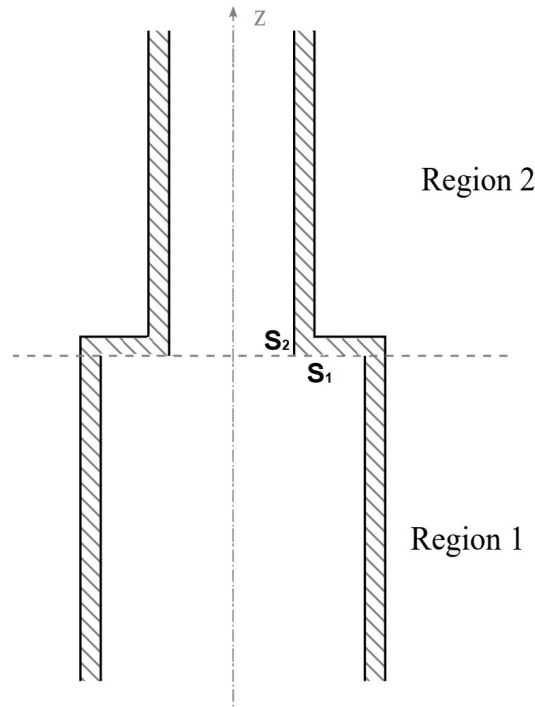


Figure 3.7: Junction of two straight waveguides.

where $i = \{1, 2\}$.

Considering the same interface S_J between the two regions of the waveguide, that now is over $z = 0$, we have that the exponential forms from (3-33) and (3-34) will be unitary. So, working again with M modes in region 1 and N modes in region 2, based on the fields continuity equations, we can rewrite (3-38) and (3-43) as

$$\begin{aligned} \sum_{m=1}^M \int \int_{S_J} \left\{ a_{1,m}^+ \left[(\mathbf{E}_{1,m}^+ \times \mathbf{H}_{2,n'}^+) \cdot \hat{z} \right] + a_{1,m}^- \left[(\mathbf{E}_{1,m}^- \times \mathbf{H}_{2,n'}^+) \cdot \hat{z} \right] \right\} dS = \\ \sum_{n=1}^N \int \int_{S_J} \left\{ a_{2,n}^+ \left[(\mathbf{E}_{2,n}^+ \times \mathbf{H}_{2,n'}^+) \cdot \hat{z} \right] + a_{2,n}^- \left[(\mathbf{E}_{2,n}^- \times \mathbf{H}_{2,n'}^+) \cdot \hat{z} \right] \right\} dS \quad (3-108) \end{aligned}$$

$$\begin{aligned} \sum_{m=1}^M \int \int_{S_J} \left\{ a_{1,m}^+ \left[(\mathbf{H}_{1,m}^+ \times \mathbf{E}_{1,m'}^+) \cdot \hat{z} \right] + a_{1,m}^- \left[(\mathbf{H}_{1,m}^- \times \mathbf{E}_{1,m'}^+) \cdot \hat{z} \right] \right\} dS = \\ \sum_{n=1}^N \int \int_{S_J} \left\{ a_{2,n}^+ \left[(\mathbf{H}_{2,n}^+ \times \mathbf{E}_{1,m'}^+) \cdot \hat{z} \right] + a_{2,n}^- \left[(\mathbf{H}_{2,n}^- \times \mathbf{E}_{1,m'}^+) \cdot \hat{z} \right] \right\} dS, \quad (3-109) \end{aligned}$$

with $n' = 0, 1, 2, \dots, N$ and $m' = 0, 1, 2, \dots, M$.

The reaction integrals become

$$X_{i(m)j(n)}^\pm = \int \int_{S_2} (\mathbf{E}_{i,m}^\pm \times \mathbf{H}_{j,n}^+) \cdot \hat{z} dS \quad (3-110)$$

$$Y_{i(m)j(n)}^\pm = \int \int_{S_2} (\mathbf{E}_{i,m}^+ \times \mathbf{H}_{j,n}^\pm) \cdot \hat{z} dS, \quad (3-111)$$

where

$$(\mathbf{E}_{i,m}^{s_i} \times \mathbf{H}_{j,n}^{s_j}) \cdot \hat{z} = s_j (E_{ix,m} H_{jy,n} - E_{iy,m} H_{jx,n}) \quad (3-112)$$

for $i = \{1, 2\}$ and $j = \{1, 2\}$.

We can also use the coordinates transformation showed in (3-61) and (3-62), and then we can express the cross product in cylindrical coordinates in the form

$$\begin{aligned} (\mathbf{E}_{i,m}^{s_i} \times \mathbf{H}_{j,n}^{s_j}) \cdot \hat{z} = \\ s_j [(E_{i\rho,m} \cos(\phi) - E_{i\phi,m} \sin(\phi))(H_{j\rho,n} \sin(\phi) + H_{j\phi,n} \cos(\phi)) \\ - (E_{i\rho,m} \sin(\phi) + E_{i\phi,m} \cos(\phi))(H_{j\rho,n} \cos(\phi) - H_{j\phi,n} \sin(\phi))] \\ = s_j (E_{i\rho,m} H_{j\phi,n} - E_{i\phi,m} H_{j\rho,n}). \quad (3-113) \end{aligned}$$

Therefore, all reaction integrals can be written as

$$\int \int_{S_2} (\mathbf{E}_{i,m}^{s_i} \times \mathbf{H}_{j,n}^{s_j}) \cdot \hat{z} dS = \int_{\phi} \int_{\rho} s_j (E_{i\rho,m} H_{j\phi,n} - E_{i\phi,m} H_{j\rho,n}) \rho d\rho d\phi, \quad (3-114)$$

where the above expression is the expected form for straight waveguides analysis [24].

3.5

Generalized Scattering Matrix

Once we define the coupling matrices $\bar{X}_{i,j}^{\pm}|_{n,m}$ and $\bar{Y}_{i,j}^{\pm}|_{n,m}$, we can use (3-41) and (3-46) to establish a relation between the amplitudes of modal fields that propagates in the positive z -direction and the amplitudes of modal fields that propagates in the negative z -direction. Accordingly, we can write

$$\begin{bmatrix} \bar{a}_1^- \\ \bar{a}_2^+ \end{bmatrix} = \bar{S} \begin{bmatrix} \bar{a}_1^+ \\ \bar{a}_2^- \end{bmatrix}, \quad (3-115)$$

where \bar{S} is the generalized scattering matrix (GSM), defined as

$$\bar{S} = \begin{bmatrix} \bar{S}_{11} & \bar{S}_{12} \\ \bar{S}_{21} & \bar{S}_{22} \end{bmatrix} = \begin{bmatrix} \bar{R}_{12} & \bar{T}_{21} \\ \bar{T}_{12} & \bar{R}_{21} \end{bmatrix}, \quad (3-116)$$

and, according [24, Ch. 5], the sub-matrices are given by

$$\bar{R}_{12} = -[\bar{Y}_{11}^- - \bar{Y}_{12}^+(\bar{X}_{22}^+)^{-1}\bar{X}_{12}^-]^{-1}[\bar{Y}_{11}^+ - \bar{Y}_{12}^+(\bar{X}_{22}^+)^{-1}\bar{X}_{12}^+] \quad (3-117)$$

$$\bar{T}_{12} = [\bar{X}_{22}^+ - \bar{X}_{12}^-(\bar{Y}_{11}^-)^{-1}\bar{Y}_{12}^+]^{-1}[\bar{X}_{12}^- - \bar{X}_{12}^-(\bar{Y}_{11}^-)^{-1}\bar{Y}_{11}^+] \quad (3-118)$$

$$\bar{R}_{21} = -[\bar{X}_{22}^+ - \bar{X}_{12}^-(\bar{Y}_{11}^-)^{-1}\bar{Y}_{12}^+]^{-1}[\bar{X}_{22}^- - \bar{X}_{12}^-(\bar{Y}_{11}^-)^{-1}\bar{Y}_{12}^-] \quad (3-119)$$

$$\bar{T}_{21} = [\bar{Y}_{11}^- - \bar{Y}_{12}^+(\bar{X}_{22}^+)^{-1}\bar{X}_{12}^-]^{-1}[\bar{Y}_{12}^- - \bar{Y}_{12}^+(\bar{X}_{22}^+)^{-1}\bar{X}_{22}^-]. \quad (3-120)$$

The sub-matrix \bar{R}_{12} relates the reflected amplitudes observed from region 1 due to incident fields in this region. Likewise, \bar{R}_{21} relates the reflected amplitudes observed from region 2 due to incident fields in this region. The sub-matrix \bar{T}_{21} relates reflected amplitudes observed from region 1, due to incident fields from region 2, and vice versa for \bar{T}_{12} .

3.6

Cascading Generalized Scattering Matrices

Considering a situation where we have two or more discontinuities in a waveguide device. To calculate the equivalent GMS of this device it will be

necessary to progressively cascade all the GSMs of each segment of waveguide and the GSM representing each junction. Considering then two discontinuities with their GSMs given by $\bar{\bar{S}}^a$ and $\bar{\bar{S}}^b$. The cascaded GSM of the problem will be denoted as $\bar{\bar{S}}^c$, and is given by

$$\bar{\bar{S}}^c = \begin{bmatrix} \bar{\bar{R}}_{12}^c & \bar{\bar{T}}_{21}^c \\ \bar{\bar{T}}_{12}^c & \bar{\bar{R}}_{21}^c \end{bmatrix} \quad (3-121)$$

where

$$\bar{\bar{R}}_{12}^c = \bar{\bar{T}}_{21}^a (\bar{\bar{I}} - \bar{\bar{R}}_{12}^b \bar{\bar{R}}_{21}^a)^{-1} \bar{\bar{R}}_{12}^b \bar{\bar{T}}_{12}^a + \bar{\bar{R}}_{12}^a \quad (3-122)$$

$$\bar{\bar{T}}_{21}^c = \bar{\bar{T}}_{21}^a (\bar{\bar{I}} - \bar{\bar{R}}_{12}^b \bar{\bar{R}}_{21}^a)^{-1} \bar{\bar{T}}_{21}^b \quad (3-123)$$

$$\bar{\bar{T}}_{12}^c = \bar{\bar{T}}_{12}^b (\bar{\bar{I}} - \bar{\bar{R}}_{21}^a \bar{\bar{R}}_{12}^b)^{-1} \bar{\bar{T}}_{12}^a \quad (3-124)$$

$$\bar{\bar{R}}_{21}^c = \bar{\bar{T}}_{12}^b (\bar{\bar{I}} - \bar{\bar{R}}_{21}^a \bar{\bar{R}}_{12}^b)^{-1} \bar{\bar{R}}_{21}^a \bar{\bar{T}}_{21}^b + \bar{\bar{R}}_{21}^b. \quad (3-125)$$

To calculate the complete GSM of a cascade problem, we need to consider the scattering matrices associated with the sections of smooth (uniform) waveguides between each discontinuity. The scattering matrix of the smooth waveguide is related to the phase shift or attenuation that each mode experiences when propagating through a certain longitudinal length. The determination of this matrix is directly related to the length of the guide and the propagation constant k_z associated with each mode. Fig. 3.8 shows a linear waveguide structure with three different regions.

For a waveguide with a length of L , we can express the smooth GSM as follows:

$$\bar{\bar{S}}^g = \begin{bmatrix} 0 & \bar{\bar{S}}_{12}^g \\ \bar{\bar{S}}_{12}^g & 0 \end{bmatrix} \quad (3-126)$$

where $\bar{\bar{S}}_{12}^g$ is a $N \times N$ diagonal matrix with elements given by

$$(\bar{\bar{S}}_{12}^g)_{nn} = e^{ik_{z,n}L}. \quad (3-127)$$

In view of (3-122)–(3-125), we can write the solution of the cascading between the GSM from a junction discontinuities, $\bar{\bar{S}}^a$, and the GSM from a

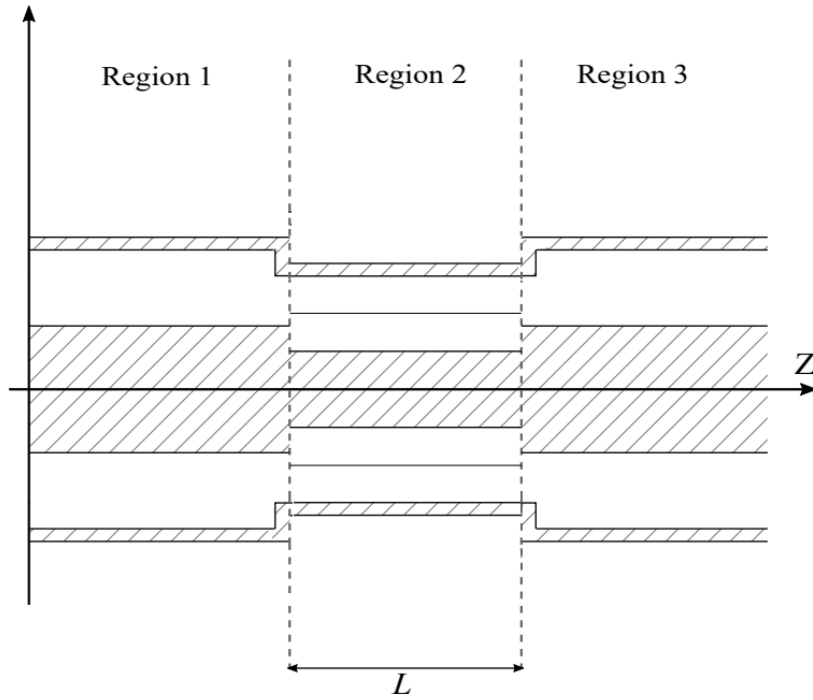


Figure 3.8: Waveguide with three different regions.

smooth section, $\bar{\bar{S}}^g$, via

$$\bar{\bar{R}}_{12}^{cg} = \bar{\bar{R}}_{12}^a \quad (3-128)$$

$$\bar{\bar{T}}_{21}^{cg} = \bar{\bar{T}}_{21}^a \bar{\bar{S}}_{12}^g \quad (3-129)$$

$$\bar{\bar{T}}_{12}^{cg} = \bar{\bar{S}}_{12}^g \bar{\bar{T}}_{12}^a \quad (3-130)$$

$$\bar{\bar{R}}_{21}^{cg} = \bar{\bar{S}}_{12}^g \bar{\bar{R}}_{21}^a \bar{\bar{S}}_{12}^g \quad (3-131)$$

Using the above formulation, we can simulate a curved section of a circular waveguide by a sequence of oblique junctions, with the final result obtained by cascading all the corresponding GSM matrices. We assume that all sections have the same angular offset and size, given by L . Fig. 3.9 shows an example of a 90-degree curve and its approximation using five cascaded oblique surfaces.

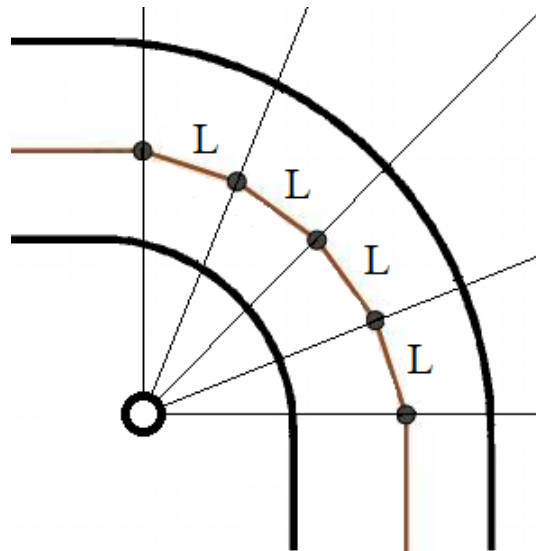


Figure 3.9: A 90-degree curved waveguide discretized into 5 regions.

4

MMT Algorithm Validation and Results

4.1

Introduction

In this chapter, we will present results that validate the algorithm developed from the above formulation, implemented in the Matlab platform, for mode-matching of cylindrical waveguides with oblique junctions. To verify both the numerical algorithm and the mathematical methodology, we will compare the results obtained from simulations generated by the CST Studio Suite program, which uses the finite element method (FEM). First, we will consider a circular waveguide with a simple horizontal junction having two regions with different characteristics. Subsequently, we will work with oblique junction structures to demonstrate the convergence of the algorithm by varying the bend angle of the waveguide and the operating frequency.

4.2

Algorithm Structure

The first step of the implemented algorithm is to set up the program input parameters. This requires to provide the physical and electromagnetic properties of the analyzed regions, as well as the operating frequency and the waveguide's bend angle (θ_{12}). After entering this information, we can define the maximum number of modes to be included in the program. Since the number of modes is given by $\sum_n \sum_p$, we can specify this by choosing a value for the maximum order of the Bessel function (n) and for the maximum number of zeros (p) for each order. The total number of modes is then given by $[(2n) + 1]p$.

Using the input information, the algorithm calculates the propagation characteristics of all TE^z and TM^z modes, following the mathematical theory presented in Chapter 2, and their respective fields using equations (3-85)–(3-96). Next, the algorithm calculates the reaction integrals as defined in (3-39) and (3-45). These results are then used to obtain the GSM matrix for the analyzed problem.

Our primary interest is in the reflection coefficients given by the sub-matrix $\bar{\bar{R}}_{12}$, specifically the reflection coefficient in decibels of the fundamental

propagation mode TE_{11}^z . We will validate the algorithm by comparing these results with those obtained from simulations generated by the CST Studio Suite program using FEM. We will begin by analyzing a circular waveguide with a simple horizontal junction in two regions with different characteristics. Later, we will work with oblique junction structures to verify the algorithm's convergence by changing the waveguide's bend angle and the operation frequency.

4.3 Straight Junctions Validation Results

4.3.1 Case 1

The first example will consider a junction of two circular waveguides with no curves, as depicted in Fig. 4.1 with electromagnetic parameters given by ϵ_1 and μ_1 , for region 1, and ϵ_2 and μ_2 , for region 2. The purpose of this simulation is to demonstrate that our algorithm can produce accurate results and analyze modal convergence. To achieve this objective, we will calculate the reflection coefficient in decibels, considering the following situation:

1. Frequency $f = 10$ GHz;
2. $r_1 = r_2 = 10$ mm;
3. $\mu_1 = \mu_2 = \mu_0$; and
4. $\epsilon_2 = g \epsilon_1$, for $g = 2, 3, \dots, 10$, and $\epsilon_1 = \epsilon_0$

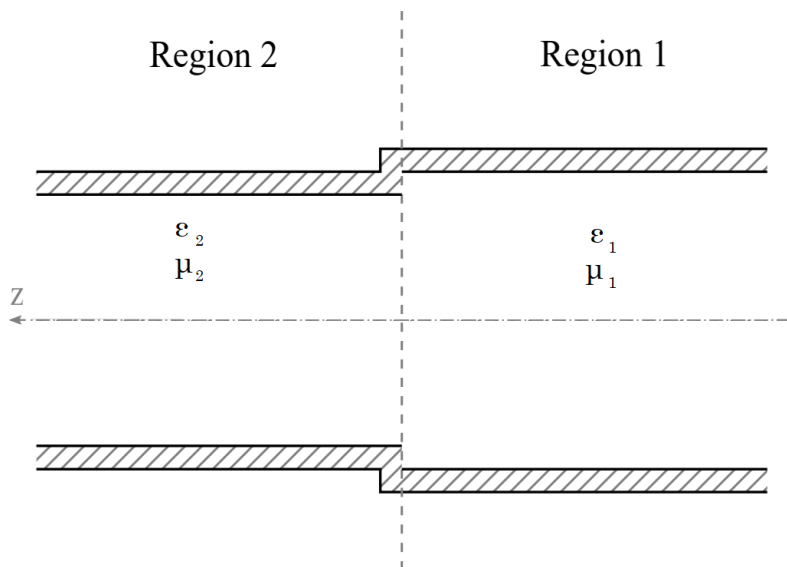


Figure 4.1: Geometry of a straight waveguide junction.

Fig. 4.2 shows the results obtained from CST simulation and from our algorithm considering only 3 modes (using $n = 1$ and $p = 1$ in our Matlab algorithm). Also, we compare the result values for the reflection coefficient in decibel from CST and from our algorithm in Table 4.1.

Table 4.1: Results of the reflection coefficient with $f = 10$ GHz and relative permittivity ϵ_2 varying with $g = 2$ to $g = 10$, using Matlab algorithm (with $n = 1$ and $p = 1$) and CST simulation.

g	$20 \log_{10}(R_{12})$ - Matlab	$20 \log_{10}(R_{12})$ - CST	Error($\Delta\%$)
2	-8.0123617	-8.0126680	0.00382%
3	-5.7623628	-5.7622099	0.00265%
4	-4.7329356	-4.7329191	0.00034%
5	-4.1112540	-4.1110499	0.00496%
6	-3.6839653	-3.6841670	0.00547%
7	-3.3671254	-3.3644770	0.07871%
8	-3.1201061	-3.1199581	0.00474%
9	-2.9205319	-2.9185736	0.06709%
10	-2.7549310	-2.7557616	0.03018%

It is worth noting that even with a minimal number of modes ($n = 1$ and $p = 1$), the algorithm achieves excellent convergence for the straight junction case. Table 4.1 demonstrates that the largest error between all values is below 0.08%, which occurs when $\epsilon_2 = 7, \epsilon_1$.

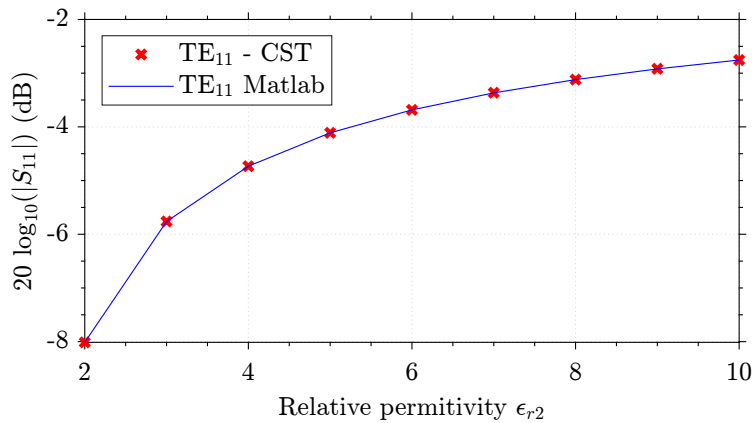


Figure 4.2: Reflection coefficient from $g = 2$ to $g = 10$. Results from CST and Matlab.

4.3.2

Case 2

To verify that convergence over the frequency, we repeat the above simulation varying the frequency in a range from 10 GHz to 15 GHz and keeping $\epsilon_2 = g\epsilon_1$, where $\epsilon_1 = \epsilon_0$ and for $g = 2, 3, 4$ and 5. Tables 4.2–4.5 compares the results from CST simulation and from our algorithm.

Table 4.2: Results of the reflection coefficient with $f = 10$ GHz to $f = 15$ GHz and $\epsilon_2 = 2\epsilon_1$, using Matlab algorithm (with $n = 1$ and $p = 1$) and CST simulation.

Frequency	$20 \log_{10}(R_{12})$ - Matlab	$20 \log_{10}(R_{12})$ - CST	Error($\Delta\%$)
10.0 GHz	-8.0126564	-8.0126680	0.00382%
10.5 GHz	-9.0934203	-9.0938631	0.00486%
11.0 GHz	-9.9090223	-9.9086474	0.00378%
11.5 GHz	-10.550058	-10.549919	0.00131%
12.0 GHz	-11.069810	-11.069560	0.00225%
12.5 GHz	-11.499257	-11.499693	0.00379%
13.0 GHz	-11.860534	-11.861628	0.00922%
13.5 GHz	-12.170113	-12.170224	0.00091%
14.0 GHz	-12.435051	-12.436228	0.00946%
14.5 GHz	-12.668808	-12.667643	0.00919%
15.0 GHz	-12.871082	-12.870571	0.00397%

Table 4.3: Results of the reflection coefficient with $f = 10$ GHz to $f = 15$ GHz and $\epsilon_2 = 3\epsilon_1$, using Matlab algorithm (with $n = 1$ and $p = 1$) and CST simulation.

Frequency	$20 \log_{10}(R_{12})$ - Matlab	$20 \log_{10}(R_{12})$ - CST	Error($\Delta\%$)
10.0 GHz	-5.7628638	-5.7622099	0.00265%
10.5 GHz	-6.5689958	-6.5703043	0.01991%
11.0 GHz	-7.1868232	-7.1859249	0.01249%
11.5 GHz	-7.6755624	-7.6748829	0.00885%
12.0 GHz	-8.0740851	-7.6748829	0.00010%
12.5 GHz	-8.4045590	-8.4065752	0.02398%
13.0 GHz	-8.6873855	-8.6878352	0.00517%
13.5 GHz	-8.9293036	-8.9287267	0.00646%
14.0 GHz	-9.1387338	-9.1371777	0.01702%
14.5 GHz	-9.3156294	-9.3191364	0.03764%
15.0 GHz	-9.4772765	-9.4791685	0.01996%

Table 4.4: Results of the reflection coefficient with $f = 10$ GHz to $f = 15$ GHz and $\epsilon_2 = 4\epsilon_1$, using Matlab algorithm (with $n = 1$ and $p = 1$) and CST simulation.

Frequency	$20 \log_{10}(R_{12})$ - Matlab	$20 \log_{10}(R_{12})$ - CST	Error($\Delta\%$)
10.0 GHz	-4.7329072	-4.7329191	0.00034%
10.5 GHz	-5.4056266	-5.4057817	0.00286%
11.0 GHz	-5.9208564	-5.9207506	0.00178%
11.5 GHz	-6.3308998	-6.3312764	0.00594%
12.0 GHz	-6.6677288	-6.6674762	0.00378%
12.5 GHz	-6.9472783	-6.9482446	0.01390%
13.0 GHz	-7.1868154	-7.1862835	0.00740%
13.5 GHz	-7.3891050	-7.3905570	0.01965%
14.0 GHz	-7.5673970	-7.5676237	0.00299%
14.5 GHz	-7.7222425	-7.7224192	0.00228%
15.0 GHz	-7.8567539	-7.8587422	0.02530%

Table 4.5: Results of the reflection coefficient with $f = 10$ GHz to $f = 15$ GHz and $\epsilon_2 = 5\epsilon_1$, using Matlab algorithm (with $n = 1$ and $p = 1$) and CST simulation.

Frequency	$20 \log_{10}(R_{12})$ - Matlab	$20 \log_{10}(R_{12})$ - CST	Error($\Delta\%$)
10.0 GHz	-4.1114224	-4.1110499	0.00496%
10.5 GHz	-4.6995752	-4.6999197	0.00733%
11.0 GHz	-5.1514611	-5.1515327	0.00138%
11.5 GHz	-5.5120452	-5.5122709	0.00409%
12.0 GHz	-5.8074017	-5.8081980	0.01371%
12.5 GHz	-6.0547225	-5.8081980	0.01602%
13.0 GHz	-6.2654237	-6.2657863	0.00578%
13.5 GHz	-6.4454250	-6.4462759	0.01320%
14.0 GHz	-6.6018981	-6.6028771	0.01482%
14.5 GHz	-6.7384236	-6.7398975	0.02187%
15.0 GHz	-6.8582698	-6.8606578	0.03481%

4.3.3

Case 3

Finally, to test the validity of our algorithm on commercial products, we took specifications for Ku-band circular waveguides from Qualwave company website, [3], as shown in Fig. 4.3, and applied the same test performed above. We checked the reflection coefficient for a circular waveguide with a diameter equal to 15.08 mm working in the middle frequency range (13.4 GHz to 18.0 GHz) when the relative permittivity ϵ_2 changes from 2 to 5 times ϵ_1 , with $\epsilon_1 = \epsilon_0$. The same experiment was simulated on CST and the results are exposed in Tables 4.6–4.9.

It is worth noting that the error between CST and our Matlab simulations remains below 1% for all situations, which demonstrates excellent convergence of our algorithm for straight waveguide cases.



Frequency Band	Frequency (GHz)	Circular Waveguide Size (mm)
Ku	12.4-15.9	17.48
	13.4-18.0	15.08
	15.9-18.0	12.70

Figure 4.3: Qualwave's circular waveguide specifications for Ku-band frequency ranges. [3]

Table 4.6: Results of the reflection coefficient with $f = 13.4$ GHz to $f = 18.0$ GHz and $\epsilon_2 = 2\epsilon_1$, using Matlab algorithm (with $n = 1$ and $p = 1$) and CST simulation.

Frequency	$20 \log_{10}(R_{12})$ - Matlab	$20 \log_{10}(R_{12})$ - CST	Error($\Delta\%$)
13.40 GHz	-8.2655473	-8.2656213	0.00089%
13.86 GHz	-9.0006622	-9.0004269	0.00261%
14.32 GHz	-9.6031741	-9.6033991	0.00234%
14.78 GHz	-10.1084866	-10.108499	0.00012%
15.24 GHz	-10.5395237	-10.539093	0.00408%
15.70 GHz	-10.9120757	-10.912682	0.00555%
16.16 GHz	-11.2375143	-11.238599	0.00965%
16.62 GHz	-11.5243105	-11.523655	0.00568%
17.08 GHz	-11.7789438	-11.777585	0.01153%
17.54 GHz	-12.0064779	-12.006980	0.00418%
18.00 GHz	-12.2109413	-12.211542	0.00491%

Table 4.7: Results of the reflection coefficient with $f = 13.4$ GHz to $f = 18.0$ GHz and $\epsilon_2 = 3\epsilon_1$, using Matlab algorithm (with $n = 1$ and $p = 1$) and CST simulation.

Frequency	$20 \log_{10}(R_{12})$ - Matlab	$20 \log_{10}(R_{12})$ - CST	Error($\Delta\%$)
13.40 GHz	-5.9506051	-5.9507606	0.00261%
13.86 GHz	-6.5002742	-6.5001778	0.00148%
14.32 GHz	-6.9543958	-6.9542147	0.00260%
14.78 GHz	-7.3378709	-7.3373413	0.00721%
15.24 GHz	-7.6669247	-7.6661365	0.01028%
15.70 GHz	-7.9528087	-7.9525814	0.00285%
16.16 GHz	-8.2036818	-8.2034664	0.00262%
16.62 GHz	-8.4256624	-8.4253672	0.00350%
17.08 GHz	-8.6234607	-8.6226805	0.00904%
17.54 GHz	-8.8007804	-8.7980806	0.03068%
18.00 GHz	-8.9605850	-8.9592200	0.01523%

Table 4.8: Results of the reflection coefficient with $f = 13.4$ GHz to $f = 18.0$ GHz and $\epsilon_2 = 4\epsilon_1$, using Matlab algorithm (with $n = 1$ and $p = 1$) and CST simulation.

Frequency	$20 \log_{10}(R_{12})$ - Matlab	$20 \log_{10}(R_{12})$ - CST	Error($\Delta\%$)
13.40 GHz	-4.8894128	-4.8893331	0.00163%
13.86 GHz	-5.3473300	-5.3472780	0.00097%
14.32 GHz	-5.7268329	-5.7265446	0.00503%
14.78 GHz	-6.0481766	-6.0484683	0.00482%
15.24 GHz	-6.3245836	-6.3238602	0.01143%
15.70 GHz	-6.5652439	-6.5647392	0.00768%
16.16 GHz	-6.7768366	-6.7770239	0.00276%
16.62 GHz	-6.9643829	-6.9629404	0.02071%
17.08 GHz	-7.1317573	-7.1313629	0.00553%
17.54 GHz	-7.2820135	-7.2805559	0.02002%
18.00 GHz	-7.4176005	-7.4160605	0.02076%

Table 4.9: Results of the reflection coefficient with $f = 13.4$ GHz to $f = 18.0$ GHz and $\epsilon_2 = 5\epsilon_1$, using Matlab algorithm (with $n = 1$ and $p = 1$) and CST simulation.

Frequency	$20 \log_{10}(R_{12})$ - Matlab	$20 \log_{10}(R_{12})$ - CST	Error($\Delta\%$)
13.40 GHz	-4.2480201	-4.2481091	0.00209%
13.86 GHz	-4.6487199	-4.6484411	0.00599%
14.32 GHz	-4.9813578	-4.9817103	0.00707%
14.78 GHz	-5.2634345	-5.2631336	0.00571%
15.24 GHz	-5.5063844	-5.5061435	0.00437%
15.70 GHz	-5.7181629	-5.7175815	0.01016%
16.16 GHz	-5.9045588	-5.9043653	0.00327%
16.62 GHz	-6.0699289	-6.0700075	0.00129%
17.08 GHz	-6.2176397	-6.2168122	0.01331%
17.54 GHz	-6.3503473	-6.3500015	0.00544%
18.00 GHz	-6.4701846	-6.4689520	0.01905%

4.3.4 Case 4

Having achieved excellent results for straight waveguide cases with two sections, we will now explore a scenario involving three straight waveguide regions. While all three regions share the same radius, the middle section will vary in length and the value of ϵ . To analyze this case, we will consider the cascade GSM situation as studied in Chapter 3. Fig. 4.4 depicts the structure analyzed, with regions *I* and *III* possessing the electromagnetic constants μ_0 and ϵ_0 , respectively, while region *II* has a length L that ranges into (5, 10, 15, 20, 25, 30) millimeters and electromagnetic parameters $\mu_0 = 2 = \mu_0$ and $\epsilon_2 = \epsilon_0 \epsilon_{r2}$, where $\epsilon_{r2} = \{2, 4\}$.

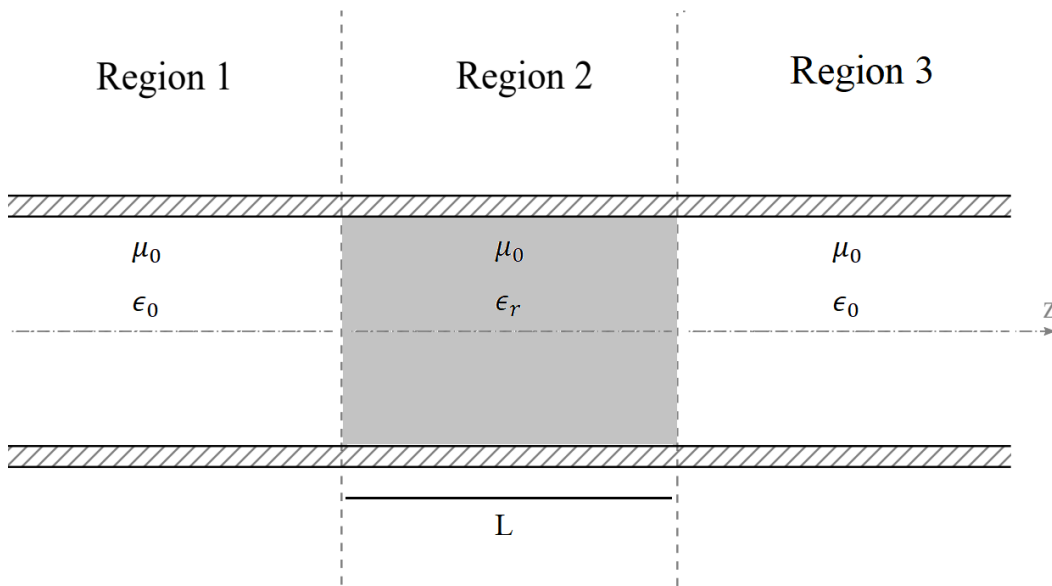


Figure 4.4: Straight waveguide device with three sections.

As with previous cases, we will compare the results obtained from CST simulations with those produced by our algorithm (with $n = 1$ and $p = 1$) for the reflection coefficient in decibels, while considering the cascade GSM problem. Tables 4.10–4.12 present the numerical results for $\epsilon_2 = 2\epsilon_0$, while Tables 4.13–4.15 display the numerical results for $\epsilon_2 = 4\epsilon_0$. Graphical results can be found in Figs. 4.5–4.10.

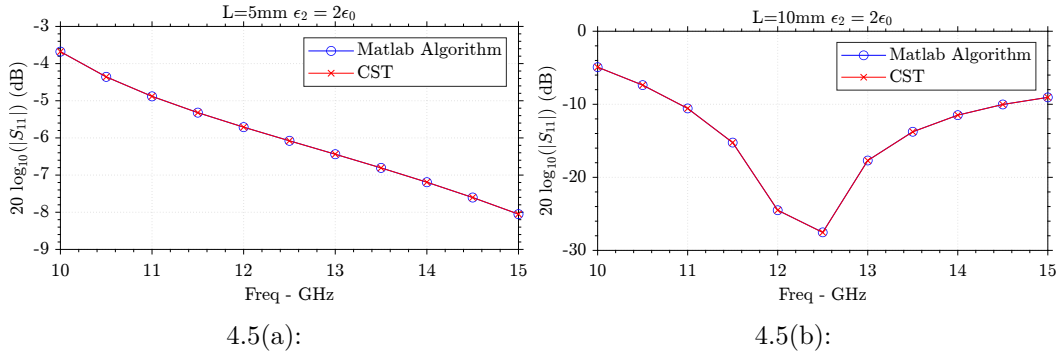


Figure 4.5: Results for (a) $L = 5$ mm $\epsilon_2 = 2\epsilon_0$ and (b) $L = 10$ mm $\epsilon_2 = 2\epsilon_0$.

Table 4.10: Results from Matlab algorithm (with $n = 1$ and $p = 1$) and CST simulation for the reflection coefficient with frequency ranging from 10 GHz to 15 GHz, $\epsilon_2 = 2\epsilon_0$ and L equals to 5 mm and 10 mm.

Freq. (GHz)	$L = 5$ mm CST	$L = 5$ mm Matlab	Error $\Delta\%$	$L = 10$ mm CST	$L = 10$ mm Matlab	Error $\Delta\%$
10	-3.6783	-3.6783	0.0012%	-4.9168	-4.9163	0.0103%
10.5	-4.3569	-4.3569	0.0013%	-7.3752	-7.3745	0.0090%
11	-4.8817	-4.8816	0.0010%	-10.5668	-10.5654	0.0135%
11.5	-5.3199	-5.3199	0.0009%	-15.2426	-15.2401	0.0159%
12	-5.7104	-5.7103	0.0011%	-24.5059	-24.4970	0.0363%
12.5	-6.0777	-6.0778	0.0021%	-27.5312	-27.5466	0.0559%
13	-6.4388	-6.4387	0.0026%	-17.6965	-17.7021	0.0320%
13.5	-6.8068	-6.8065	0.0040%	-13.7616	-13.7654	0.0276%
14	-7.1920	-7.1916	0.0058%	-11.4873	-11.4901	0.0243%
14.5	-7.6038	-7.6032	0.0083%	-10.0247	-10.0266	0.0193%
15	-8.0511	-8.0502	0.0113%	-9.0519	-9.0529	0.0112%

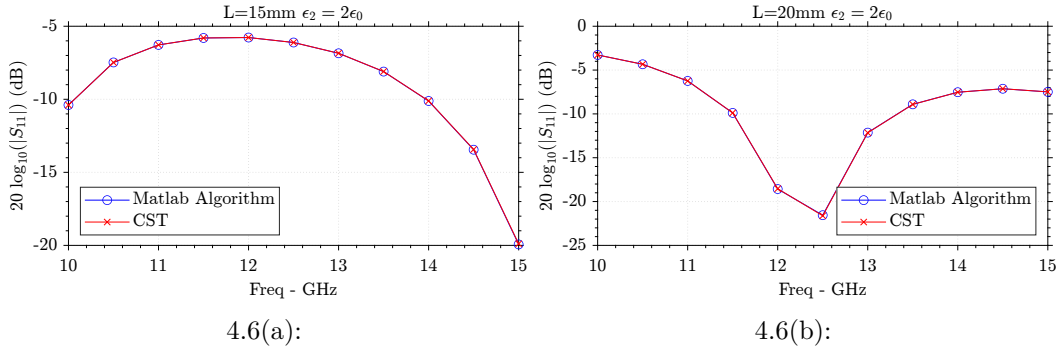


Figure 4.6: Results for (a) $L = 15$ mm $\epsilon_2 = 2\epsilon_0$ and (b) $L = 20$ mm $\epsilon_2 = 2\epsilon_0$.

Table 4.11: Results from Matlab algorithm (with $n = 1$ and $p = 1$) and CST simulation for the reflection coefficient with frequency ranging from 10 GHz to 15 GHz, $\epsilon_2 = 2\epsilon_0$ and L equals to 15 mm and 20 mm.

Freq. (GHz)	$L = 15$ mm CST	$L = 15$ mm Matlab	Error $\Delta\%$	$L = 20$ mm CST	$L = 20$ mm Matlab	Error $\Delta\%$
10	-10.3903	-10.3930	0.0253%	-3.2765	-3.2763	0.0052%
10.5	-7.4773	-7.4782	0.0122%	-4.3385	-4.3379	0.0154%
11	-6.2783	-6.2787	0.0054%	-6.2403	-6.2379	0.0381%
11.5	-5.8027	-5.8025	0.0045%	-9.8882	-9.8802	0.0816%
12	-5.7724	-5.7719	0.0088%	-18.5728	-18.5374	0.1912%
12.5	-6.1131	-6.1119	0.0204%	-21.5568	-21.6193	0.2888%
13	-6.8516	-6.8491	0.0365%	-12.1350	-12.1548	0.1628%
13.5	-8.1034	-8.0987	0.0581%	-8.9075	-8.9178	0.1159%
14	-10.1170	-10.1083	0.0865%	-7.5263	-7.5308	0.0598%
14.5	-13.4516	-13.4342	0.1293%	-7.1314	-7.1303	0.0152%
15	-19.9326	-19.8911	0.2085%	-7.4931	-7.4847	0.1124%

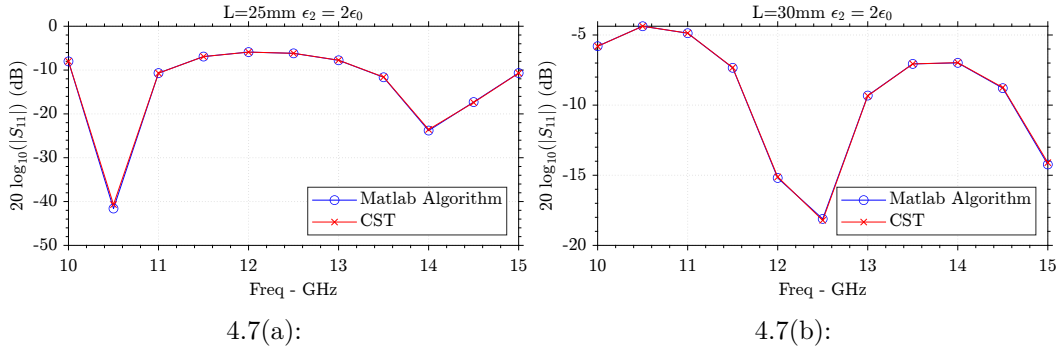


Figure 4.7: Results for (a) $L = 25 \text{ mm}$ $\epsilon_2 = 2\epsilon_0$ and (b) $L = 30 \text{ mm}$ $\epsilon_2 = 2\epsilon_0$.

Table 4.12: Results from Matlab algorithm (with $n = 1$ and $p = 1$) and CST simulation for the reflection coefficient with frequency ranging from 10 GHz to 15 GHz, $\epsilon_2 = 2\epsilon_0$ and L equals to 25 mm and 30 mm.

Freq. (GHz)	$L = 25 \text{ mm}$ CST	$L = 25 \text{ mm}$ Matlab	Error $\Delta\%$	$L = 30 \text{ mm}$ CST	$L = 30 \text{ mm}$ Matlab	Error $\Delta\%$
10	-8.0170	-8.0010	0.2007%	-5.7991	-5.8073	0.1411%
10.5	-41.5900	-40.6823	2.2311%	-4.3760	-4.3771	0.0256%
11	-10.6860	-10.7072	0.1979%	-4.8721	-4.8679	0.0865%
11.5	-6.9192	-6.9262	0.1005%	-7.3401	-7.3235	0.2262%
12	-5.8986	-5.8993	0.0103%	-15.1941	-15.1230	0.4701%
12.5	-6.1848	-6.1784	0.1026%	-18.1114	-18.2113	0.5489%
13	-7.7664	-7.7477	0.2407%	-9.3189	-9.3395	0.2200%
13.5	-11.6450	-11.5958	0.4242%	-7.0623	-7.0624	0.0011%
14	-23.8049	-23.5608	1.0363%	-6.9874	-6.9702	0.2465%
14.5	-17.3045	-17.4055	0.5798%	-8.7907	-8.7438	0.5366%
15	-10.6781	-10.7018	0.2223%	-14.2332	-14.1012	0.9364%

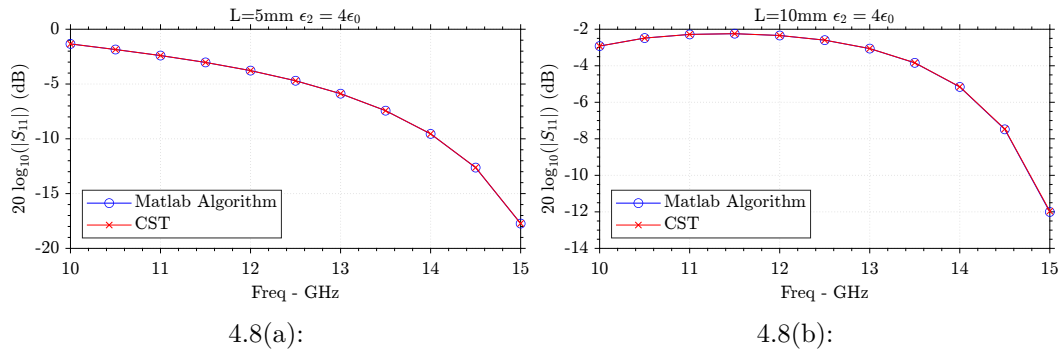


Figure 4.8: Results for (a) $L = 5 \text{ mm}$ $\epsilon_2 = 4\epsilon_0$ and (b) $L = 10 \text{ mm}$ $\epsilon_2 = 4\epsilon_0$.

Table 4.13: Results from Matlab algorithm (with $n = 1$ and $p = 1$) and CST simulation for the reflection coefficient with frequency ranging from 10 GHz to 15 GHz, $\epsilon_2 = 4\epsilon_0$ and L equals to 5 mm and 10 mm

Freq. (GHz)	$L = 5 \text{ mm}$ CST	$L = 5 \text{ mm}$ Matlab	Error $\Delta\%$	$L = 10 \text{ mm}$ CST	$L = 10 \text{ mm}$ Matlab	Error $\Delta\%$
10	-1.3404	-1.3403	0.0080%	-2.9205	-2.9214	0.0297%
10.5	-1.8514	-1.8513	0.0096%	-2.4830	-2.4835	0.0203%
11	-2.4011	-2.4008	0.0121%	-2.2830	-2.2831	0.0068%
11.5	-3.0277	-3.0273	0.0158%	-2.2432	-2.2430	0.0099%
12	-3.7756	-3.7748	0.0207%	-2.3431	-2.3423	0.0317%
12.5	-4.7007	-4.6995	0.0269%	-2.5977	-2.5962	0.0600%
13	-5.8809	-5.8789	0.0327%	-3.0599	-3.0570	0.0963%
13.5	-7.4325	-7.4294	0.0414%	-3.8405	-3.8350	0.1419%
14	-9.5511	-9.5463	0.0501%	-5.1599	-5.1497	0.1980%
14.5	-12.6278	-12.6201	0.0607%	-7.4819	-7.4619	0.2676%
15	-17.7381	-17.7241	0.0788%	-12.0065	-11.9619	0.3727%

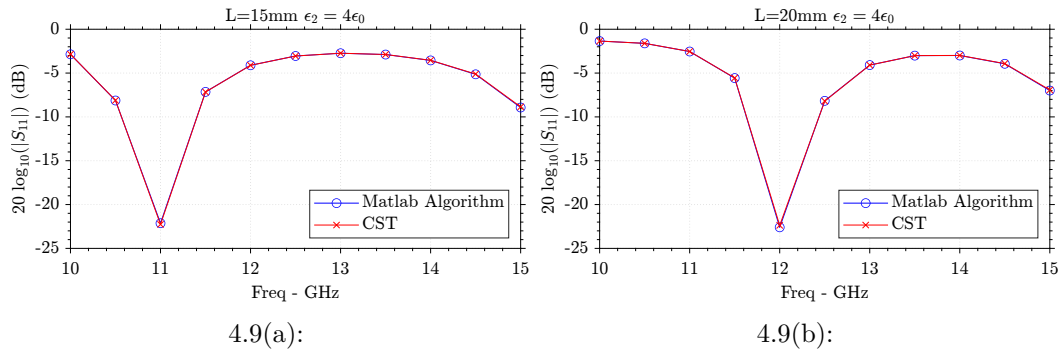


Figure 4.9: Results for (a) $L = 15$ mm $\epsilon_2 = 4\epsilon_0$ (b) $L = 20$ mm $\epsilon_2 = 4\epsilon_0$.

Table 4.14: Results from Matlab algorithm (with $n = 1$ and $p = 1$) and CST simulation for the reflection coefficient with frequency ranging from 10 GHz to 15 GHz, $\epsilon_2 = 4\epsilon_0$ and L equals to 15 mm and 20 mm.

Freq. (GHz)	$L = 15$ mm CST	$L = 15$ mm Matlab	Error $\Delta\%$	$L = 20$ mm CST	$L = 20$ mm Matlab	Error $\Delta\%$
10	-2.8591	-2.8549	0.1480%	-1.3484	-1.3487	0.0224%
10.5	-8.1306	-8.1107	0.2448%	-1.6104	-1.6096	0.0523%
11	-22.1321	-22.2635	0.5902%	-2.5412	-2.5372	0.1574%
11.5	-7.1470	-7.1624	0.2157%	-5.5727	-5.5553	0.3128%
12	-4.1120	-4.1172	0.1250%	-22.5975	-22.3746	0.9961%
12.5	-3.0520	-3.0530	0.0352%	-8.1687	-8.1978	0.3549%
13	-2.7374	-2.7355	0.0695%	-4.0887	-4.0942	0.1339%
13.5	-2.8875	-2.8817	0.2003%	-3.0111	-3.0087	0.0785%
14	-3.5552	-3.5424	0.3633%	-2.9960	-2.9864	0.3217%
14.5	-5.1408	-5.1111	0.5807%	-3.9418	-3.9174	0.6241%
15	-8.9307	-8.8539	0.8672%	-6.9947	-6.9245	1.0136%

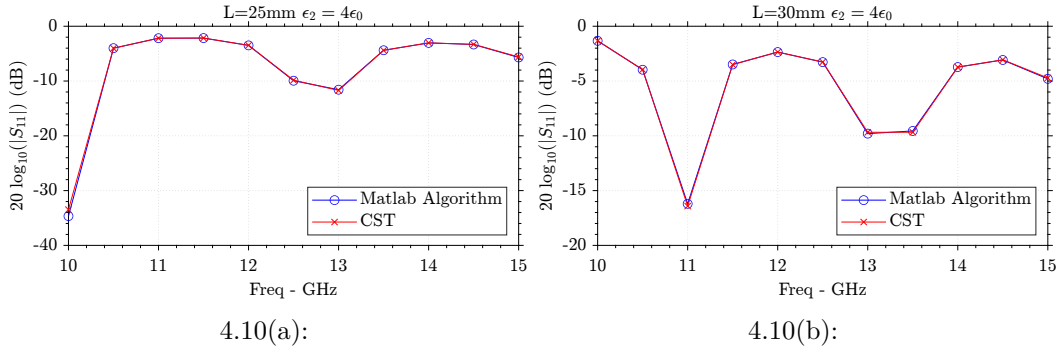


Figure 4.10: Results for (a) $L = 25 \text{ mm}$ $\epsilon_2 = 4\epsilon_0$ and (b) $L = 30 \text{ mm}$ $\epsilon_2 = 4\epsilon_0$.

Table 4.15: Results from Matlab algorithm (with $n = 1$ and $p = 1$) and CST simulation for the reflection coefficient with frequency ranging from 10 GHz to 15 GHz, $\epsilon_2 = 4\epsilon_0$ and L equals to 25 mm and 30 mm.

Freq. (GHz)	$L = 25 \text{ mm}$ CST	$L = 25 \text{ mm}$ Matlab	Error $\Delta\%$	$L = 30 \text{ mm}$ CST	$L = 30 \text{ mm}$ Matlab	Error $\Delta\%$
10	-34.6552	-33.4764	3.5212%	-1.3327	-1.3312	0.1102%
10.5	-4.0036	-4.0175	0.3447%	-3.9709	-3.9520	0.4784%
11	-2.1839	-2.1864	0.1130%	-16.2046	-16.4140	1.2752%
11.5	-2.1623	-2.1596	0.1254%	-3.4876	-3.5032	0.4449%
12	-3.4937	-3.4780	0.4498%	-2.3575	-2.3585	0.0427%
12.5	-9.9449	-9.8455	1.0092%	-3.2756	-3.2608	0.4531%
13	-11.5846	-11.7136	1.1014%	-9.8020	-9.6780	1.2816%
13.5	-4.3843	-4.4027	0.4167%	-9.5559	-9.6752	1.2331%
14	-3.0418	-3.0375	0.1412%	-3.7256	-3.7369	0.3027%
14.5	-3.3303	-3.3040	0.7942%	-3.0791	-3.0610	0.5913%
15	-5.6973	-5.6045	1.6563%	-4.8014	-4.7190	1.7459%

Again, comparing with the results of the simulations in the CST software we can observe a great convergence for the Matlab algorithm even using a minimum number of modes, with $n = 1$ and $p = 1$. We have some occasional cases where the error is about 3%, but in general we can observe an error rate of less than 1%, which demonstrates the effectiveness of the Matlab program for cascaded straight waveguide cases.

4.4 Oblique Junctions Results

The second set of examples that we analyze involves homogeneous to homogeneous oblique junction configurations. In these cases, we work with a circular waveguide having two regions with the same physical and electromagnetic values, i.e., $r_1 = r_2$, $\mu_1 = \mu_2 = \mu_0$, and $\epsilon_1 = \epsilon_2 = \epsilon_0$. These two regions are angularly displaced by $\theta = 2\theta_{12}$, as depicted in Fig. 4.11.

4.4.1 Case 1

At the first example, in order to verify the modal convergence we simulated some situations where θ_{12} varies in a range of 5 to 45 degrees, where the total bend of the waveguide is given by $2\theta_{12}$, i.e. θ will vary from 10 to 90 degrees. For each situation, we worked with n and p ranging from 1 to 3 and we obtained the results values for the reflection coefficient in decibel. We will compare the algorithm data with the results from the CST simulation, using the FEM solver. Tables 4.16–4.18 show the results obtained in CST simulations and comparison with the obtained via our algorithm, considering the TE_{11}^z mode as a $\cos(n\phi)$ configuration. Tables 4.19–4.21 shows the same results considering the TE_{11}^z mode as a $\sin(n\phi)$ configuration. The structures used for the Sine and Cosine configurations are shown in Figs. 4.12 and 4.13, respectively, using CST's CAD software. For brevity, the labels Sin and Cos will be used to refer to these configurations in the following discussion. Moreover, the labels Nn and Pp will indicate the number of harmonics used, with $n = 1, 2, 3, \dots$ and $p = 1, 2, 3, \dots$.

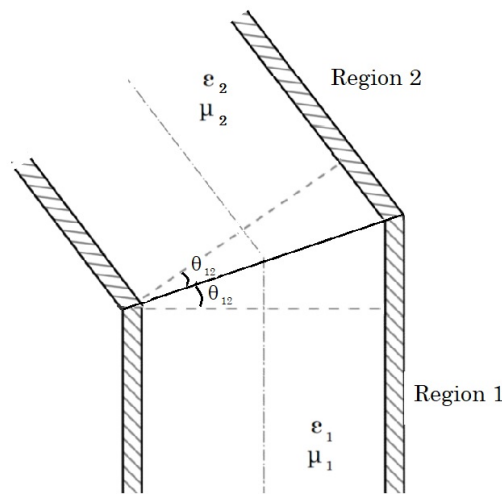


Figure 4.11: Geometry of an oblique waveguide junction.

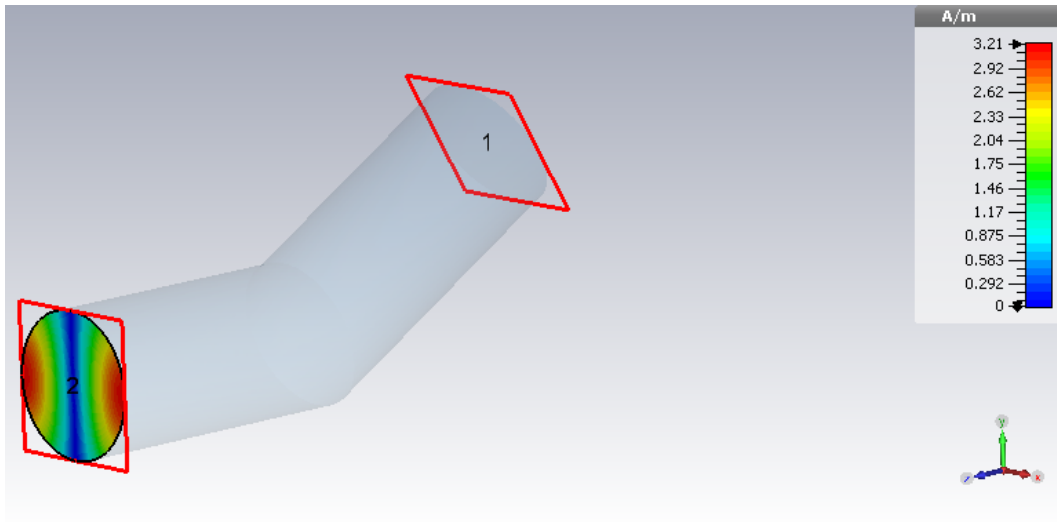


Figure 4.12: CST structure with TE_{11}^z mode excitation as a $\sin(n\phi)$ configuration.

PUC-Rio - Certificação Digital N° 2112302/CA

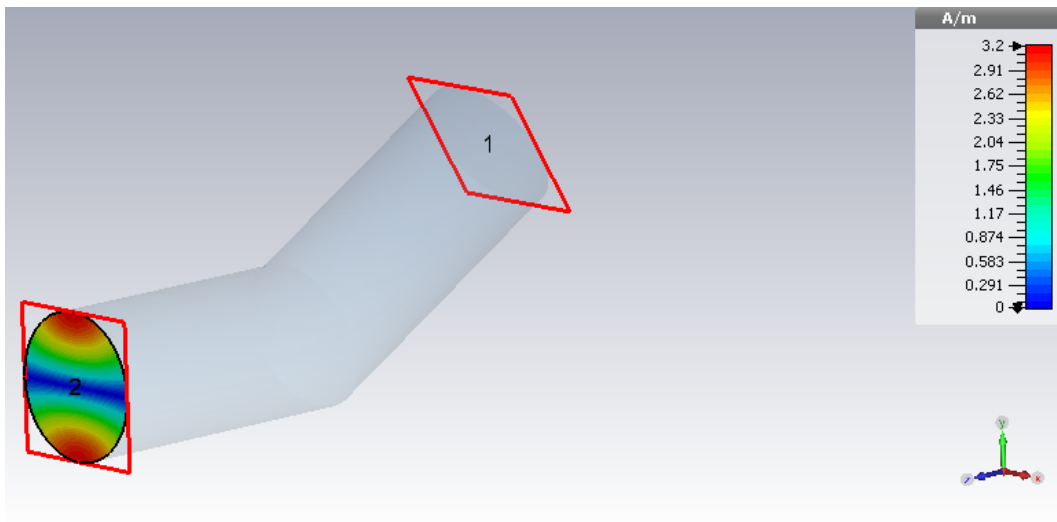


Figure 4.13: CST structure with TE_{11}^z mode excitation as a $\cos(n\phi)$ configuration.

Figs. 4.14–4.19 summarize the results presented in Tables 4.16–4.21 by showing the absolute error (in decibels) between CST results and our algorithm simulations.

Table 4.16: Results of the reflection coefficient for TE_{11}^z mode as a $\cos(n\phi)$ with $f = 10$ GHz and θ ($2\theta_{12}$) ranging from 10° to 90° , using Matlab algorithm (with $n = 1$ and $p = 1, 2,$ and 3) and comparing with CST simulation.

θ	CST	Matlab $n = 1$ $p = 1$	Error $\Delta\%$	Matlab $n = 1$ $p = 2$	Error $\Delta\%$	Matlab $n = 1$ $p = 3$	Error $\Delta\%$
10	-42.5961	-51.5019	20.90%	-50.5872	18.76%	-50.3010	18.08%
20	-30.9162	-39.1725	26.70%	-37.8352	22.38%	-37.3408	20.78%
30	-23.9208	-31.7726	32.82%	-29.7577	24.40%	-29.0164	21.30%
40	-19.0347	-26.5006	39.22%	-23.5643	23.79%	-22.5647	18.54%
50	-15.1783	-22.5910	48.83%	-18.4656	21.65%	-17.2312	13.52%
60	-11.4298	-19.7677	72.94%	-14.1716	23.98%	-12.7049	11.15%
70	-8.0864	-17.8943	121.28%	-10.3535	28.04%	-9.1739	13.44%
80	-5.0637	-16.7853	231.47%	-6.40035	26.39%	-5.1493	1.61%
90	-2.4843	-16.4795	563.33%	-1.83436	26.16%	1.4743	159.34%

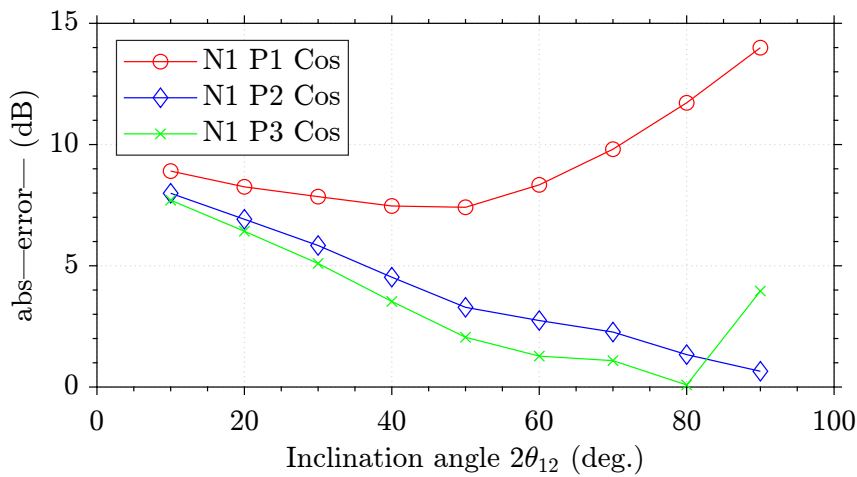


Figure 4.14: Absolute error (dB) between CST simulation and algorithm (with $n = 1$) for TE_{11}^z mode as a $\cos(n\phi)$.

Table 4.17: Results of the reflection coefficient for TE_{11}^z mode as a $\cos(n\phi)$ with $f = 10$ GHz and θ ($2\theta_{12}$) ranging from 10° to 90° , using Matlab algorithm (with $n = 2$ and $p = 1, 2, \text{ and } 3$) and comparing with CST simulation.

θ	CST	Matlab $n = 2$ $p = 1$	Error $\Delta\%$	Matlab $n = 2$ $p = 2$	Error $\Delta\%$	Matlab $n=2$ $p = 3$	Error $\Delta\%$
10	-42.5961	-43.2153	1.45%	-42.6135	0.04%	-42.4146	0.42%
20	-30.9162	-31.6265	2.29%	-30.5979	1.02%	-30.1626	2.43%
30	-23.9208	-25.3114	5.81%	-23.4972	1.77%	-22.5262	5.83%
40	-19.0347	-21.2609	11.69%	-18.3023	3.84%	-16.4910	13.36%
50	-15.1783	-18.5222	22.03%	-14.0207	7.62%	-11.3439	25.26%
60	-11.4298	-16.6749	45.88%	-10.2978	9.90%	-4.46602	60.92%
70	-8.0863	-15.5714	92.56%	-6.23607	22.88%	4.9875	161.67%
80	-5.0637	-15.0445	197.10%	-3.64016	28.11%	11.0938	319.08%
90	-2.4843	-15.7410	533.61%	-1.16958	52.92%	10.8573	537.03%

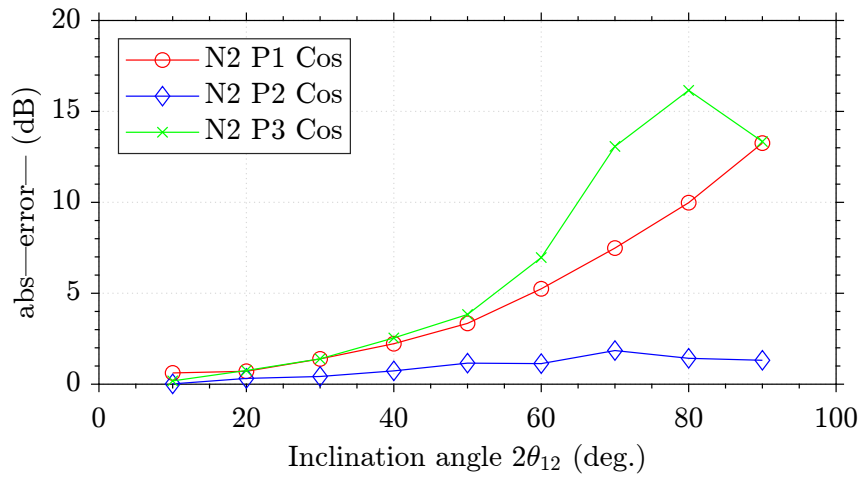


Figure 4.15: Absolute error (dB) between CST simulation and algorithm (with $n = 2$) for TE_{11}^z mode as a $\cos(n\phi)$.

Table 4.18: Results of the reflection coefficient for TE_{11}^z mode as a $\cos(n\phi)$ with $f = 10$ GHz and θ ($2\theta_{12}$) ranging from 10° to 90° , using Matlab algorithm (with $n = 3$ and $p = 1, 2,$ and 3) and comparing with CST simulation.

θ	CST	Matlab $n = 3$ $p = 1$	Error $\Delta\%$	Matlab $n = 3$ $p = 2$	Error $\Delta\%$	Matlab $n=3$ $p = 3$	Error $\Delta\%$
10	-42.5961	-43.0460	1.05%	-42.4367	0.37%	-42.1838	0.96%
20	-30.9162	-30.9276	0.03%	-29.7733	3.69%	-29.1201	5.80%
30	-23.9208	-23.7846	0.56%	-21.6898	9.32%	-20.6333	13.74%
40	-19.0347	-18.9051	0.68%	-16.7198	12.16%	-14.6480	23.04%
50	-15.1783	-15.6239	2.93%	-14.8477	2.17%	-7.0268	53.70%
60	-11.4298	-12.2457	7.13%	-7.2644	36.44%	-14.8474	29.89%
70	-8.0863	-12.2677	51.70%	-5.0766	37.22%	17.8095	320.24%
80	-5.0637	-8.3579	65.05%	-8.9148	76.05%	4.7653	194.10%
90	-2.4843	-11.2766	353.90%	1.0083	140.58%	12.2592	593.46%

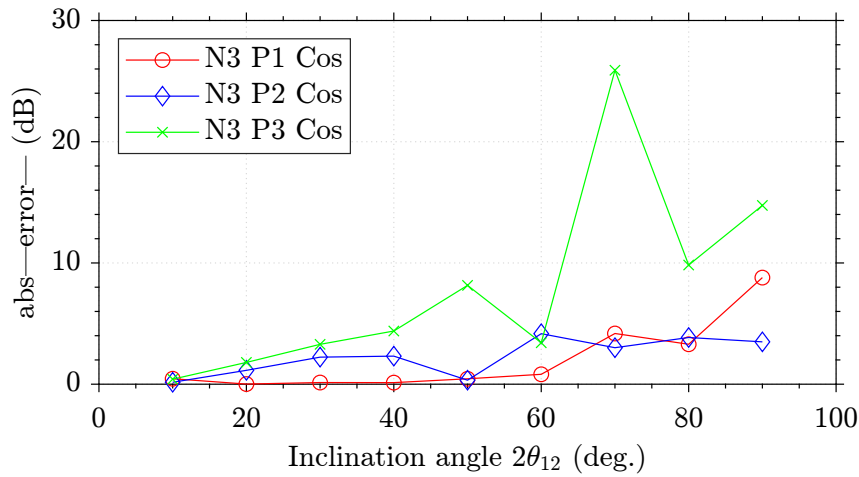


Figure 4.16: Absolute error (dB) between CST simulation and algorithm (with $n = 3$) for TE_{11}^z mode as a $\cos(n\phi)$.

Table 4.19: Results of the reflection coefficient for TE_{11}^z mode as a $\sin(n\phi)$ with $f = 10$ GHz and θ ($2\theta_{12}$) ranging from 10° to 90° , using Matlab algorithm (with $n = 1$ and $p = 1, 2, \text{ and } 3$) and comparing with CST simulation.

θ	CST	Matlab $n = 1$ $p = 1$	Error $\Delta\%$	Matlab $n = 1$ $p = 2$	Error $\Delta\%$	Matlab $n = 1$ $p = 3$	Error $\Delta\%$
10	-44.6418	-39.7949	10.85%	-39.5745	11.35%	-39.5163	11.48%
20	-32.2696	-27.7873	13.89%	-27.5505	14.62%	-27.4890	14.81%
30	-24.9151	-20.7511	16.71%	-20.4884	17.76%	-20.4222	18.03%
40	-19.5429	-15.6842	19.74%	-15.3945	21.22%	-15.3179	21.61%
50	-15.3075	-11.6277	24.03%	-11.3376	25.93%	-11.2683	26.38%
60	-12.3711	-8.16842	33.97%	-7.9202	35.97%	-7.7999	36.95%
70	-10.0023	-5.13030	48.70%	-5.0253	49.75%	-4.9193	50.81%
80	-8.06388	-2.49626	69.04%	-2.5092	68.88%	-2.5828	67.97%
90	-6.45892	-0.40037	93.80%	-1.1329	82.45%	-1.1235	82.60%

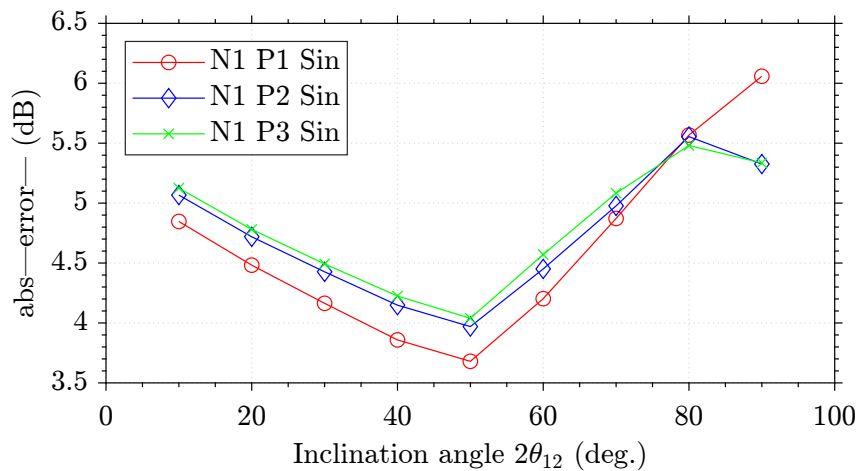


Figure 4.17: Absolute error (dB) between CST simulation and algorithm (with $n = 1$) for TE_{11}^z mode as a $\sin(n\phi)$.

Table 4.20: Results of the reflection coefficient for TE_{11}^z mode as a $\sin(n\phi)$ with $f = 10$ GHz and θ ($2\theta_{12}$) ranging from 10° to 90° , using Matlab algorithm (with $n = 2$ and $p = 1, 2,$ and 3) and comparing with CST simulation.

θ	CST	Matlab $n = 2$ $p = 1$	Error $\Delta\%$	Matlab $n = 2$ $p = 2$	Error $\Delta\%$	Matlab $n = 2$ $p = 3$	Error $\Delta\%$
10	-44.6418	-41.3269	7.42%	-41.0437	8.05%	-40.9440	8.28%
20	-32.2696	-29.1111	9.78%	-28.8059	10.73%	-28.6928	11.08%
30	-24.9151	-21.8106	12.46%	-21.4879	13.75%	-21.3523	14.29%
40	-19.5429	-16.4909	15.61%	-16.1547	17.33%	-16.0329	17.96%
50	-15.3075	-12.2190	20.17%	-11.9019	22.24%	-11.8725	22.44%
60	-12.3711	-8.7006	29.66%	-8.4580	31.63%	-9.3141	24.71%
70	-10.0023	-5.7102	42.91%	-5.2385	47.62%	-5.0100	49.91%
80	-8.0638	-3.3088	58.96%	-2.8404	64.77%	-3.6291	54.99%
90	-6.4589	-1.1983	81.44%	-0.6229	90.35%	-2.7772	57.00%

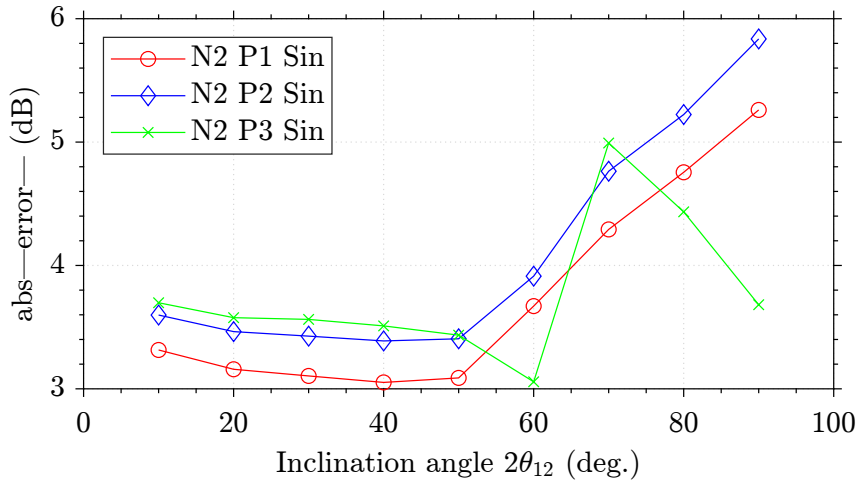


Figure 4.18: Absolute error (dB) between CST simulation and algorithm (with $n = 2$) for TE_{11}^z mode as a $\sin(n\phi)$.

Table 4.21: Results of the reflection coefficient for TE_{11}^z mode as a $\sin(n\phi)$ with $f = 10$ GHz and θ ($2\theta_{12}$) ranging from 10° to 90° , using Matlab algorithm (with $n = 3$ and $p = 1, 2, \text{ and } 3$) and comparing with CST simulation.

θ	CST	Matlab $n = 3$ $p = 1$	Error $\Delta\%$	Matlab $n = 3$ $p = 2$	Error $\Delta\%$	Matlab $n = 3$ $p = 3$	Error $\Delta\%$
10	-44.6418	-41.3356	7.40%	-41.0618	8.01%	-40.9586	8.25%
20	-32.2696	-29.1628	9.62%	-28.8942	10.46%	-28.7787	10.81%
30	-24.9151	-21.8913	12.13%	-21.6260	13.20%	-21.2661	14.64%
40	-19.5429	-16.5379	15.37%	-16.3026	16.58%	-12.3558	36.77%
50	-15.3075	-12.1761	20.45%	-11.8793	22.39%	-11.8324	22.70%
60	-12.3711	-8.3239	32.71%	-8.0147	35.21%	-8.9149	27.93%
70	-10.0023	-5.5639	44.37%	-4.9194	50.81%	-3.7671	62.33%
80	-8.0638	-2.5377	68.52%	-3.2449	59.75%	4.2489	152.69%
90	-6.4589	-0.0647	101.00%	0.2597	104.02%	3.8053	158.91%

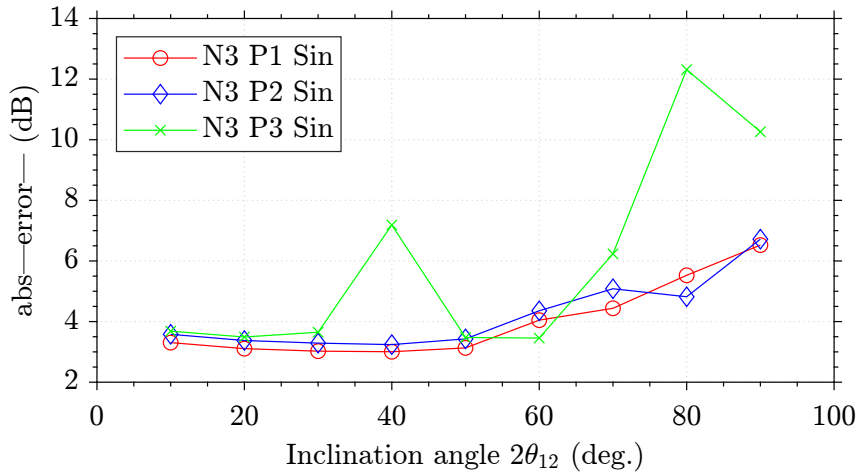


Figure 4.19: Absolute error (dB) between CST simulation and algorithm (with $n = 3$) for TE_{11}^z mode as a $\sin(n\phi)$.

We can observe that for both TE_{11}^z cases, the configuration that presents the minimum error for most of angles analyzed is the one with 14 modes, where $n = 3$ and $p = 1$. In Figs. 4.20 and 4.21 we have a comparative between the results of the reflection coefficient from CST simulation and from our algorithm with $n = 3$ and $p = 1$.

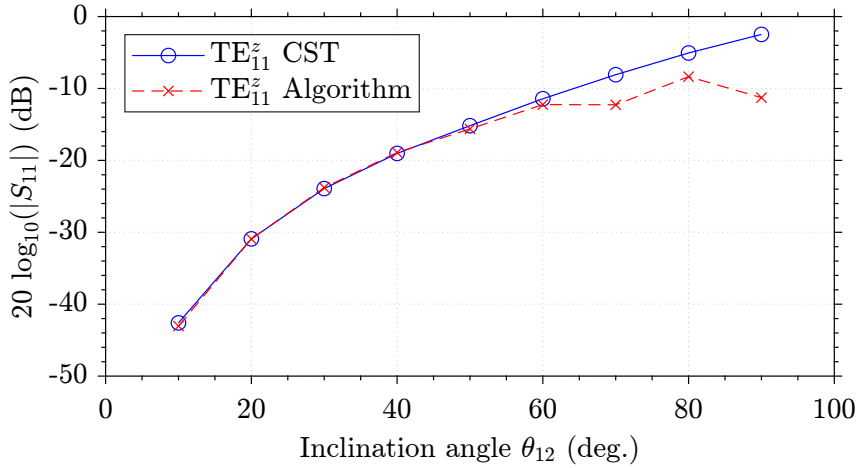


Figure 4.20: Reflection Coefficient TE_{11}^z mode as a $\cos(n\phi)$.

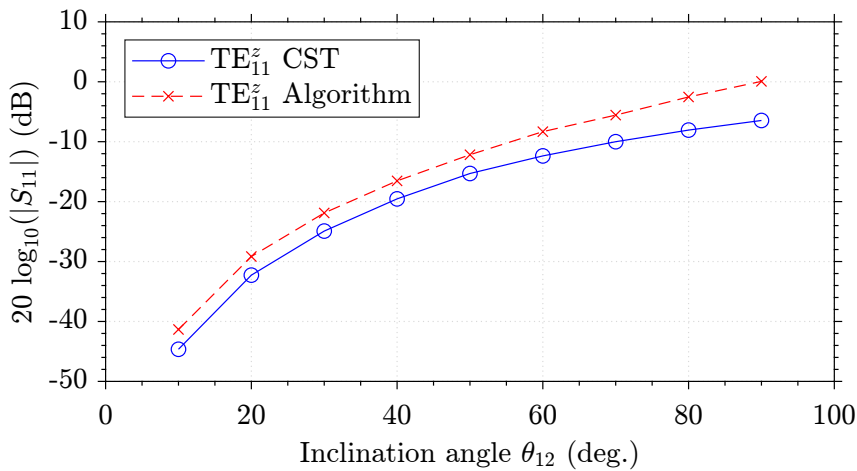


Figure 4.21: Reflection Coefficient for TE_{11}^z mode as a $\sin(n\phi)$.

The plot in Fig. 4.20 indicates that the algorithm achieves excellent convergence for total angles ($2\theta_{12}$) less than 60° . Similarly, from Fig. 4.21, it is evident that the algorithm produces a response with a similar behavior to that of CST, but with a nearly constant difference of approximately 3 dB for angles less than 60° .

4.4.2 Case 2

The second test aimed to evaluate the frequency response of our algorithm in an oblique junction scenario. As the algorithm showed better

convergence for smaller angles, we tested responses for inclination angles ranging from 5 to 30 degrees. For each angle, we recorded the reflection coefficient for frequencies ranging from 10 GHz to 15 GHz with a 0.5 GHz step. Once again, we compared our results with those from CST simulations. Tables 4.22–4.32 present the results for TE_{11}^z mode excitation as a $\cos(n\phi)$ configuration and Tables 4.33–4.43 shows results for TE_{11}^z mode as a $\sin(n\phi)$. The absolute error (in decibel) between solutions are depicted in Figs. 4.22–4.43.

Table 4.22: Results of the reflection coefficient for TE_{11}^z mode as a $\cos(n\phi)$ with $f = 10$ GHz and θ ($2\theta_{12}$) ranging from 5° to 30° , using Matlab algorithm (with $n = 1, 2$, and 3 and $p = 1$) and comparing with CST simulation.

θ	CST	Matlab $n = 1$ $p = 1$	Error $\Delta\%$	Matlab $n = 2$ $p = 1$	Error $\Delta\%$	Matlab $n = 3$ $p = 1$	Error $\Delta\%$
5	-54.9143	-63.6253	13.69%	-55.1429	0.41%	-55.0973	0.33%
10	-42.8499	-51.5019	16.79%	-43.2153	0.84%	-43.0460	0.45%
15	-35.8205	-44.3302	19.19%	-36.3608	1.48%	-35.9809	0.44%
20	-30.8372	-39.1725	21.27%	-31.6265	2.49%	-30.9276	0.29%
25	-26.9905	-35.1189	23.14%	-28.0796	3.87%	-26.9319	0.21%
30	-23.8662	-31.7726	24.88%	-25.3114	5.70%	-23.7846	0.34%

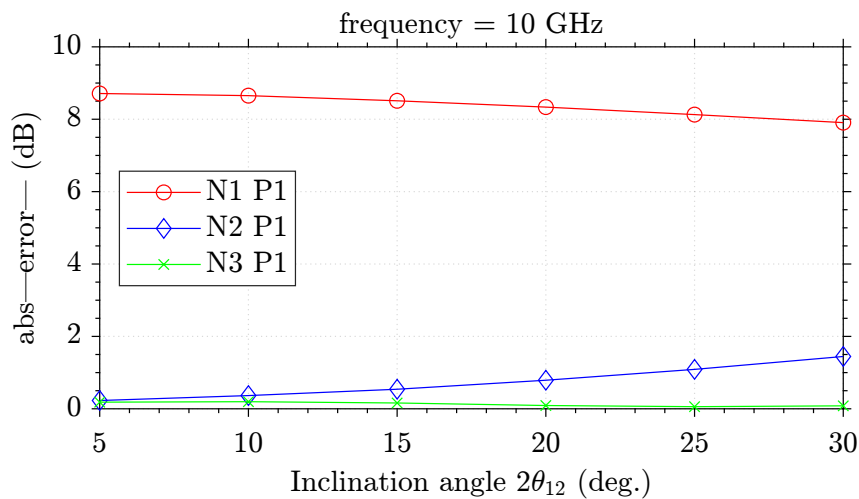


Figure 4.22: Absolute error for the configuration $\cos(n\phi)$, with $f = 10$ GHz.

Table 4.23: Results of the reflection coefficient for TE_{11}^z mode as a $\cos(n\phi)$ with $f = 10.5$ GHz and θ ($2\theta_{12}$) ranging from 5° to 30° , using Matlab algorithm (with $n = 1, 2$, and 3 and $p = 1$) and comparing with CST simulation.

θ	CST	Matlab $n = 1$ $p = 1$	Error $\Delta\%$	Matlab $n = 2$ $p = 1$	Error $\Delta\%$	Matlab $n = 3$ $p = 1$	Error $\Delta\%$
5	-56.5181	-65.0431	13.10%	-56.5432	0.04%	-56.4907	0.04%
10	-44.4929	-52.9234	15.92%	-44.6200	0.28%	-44.4438	0.11%
15	-37.4598	-45.7568	18.13%	-37.7642	0.80%	-37.3822	0.20%
20	-32.4831	-40.6051	20.00%	-33.0241	1.63%	-32.3103	0.53%
25	-28.6301	-36.5577	21.68%	-29.4738	2.86%	-28.3320	1.05%
30	-25.4955	-33.2189	23.24%	-26.6972	4.50%	-25.0230	1.88%

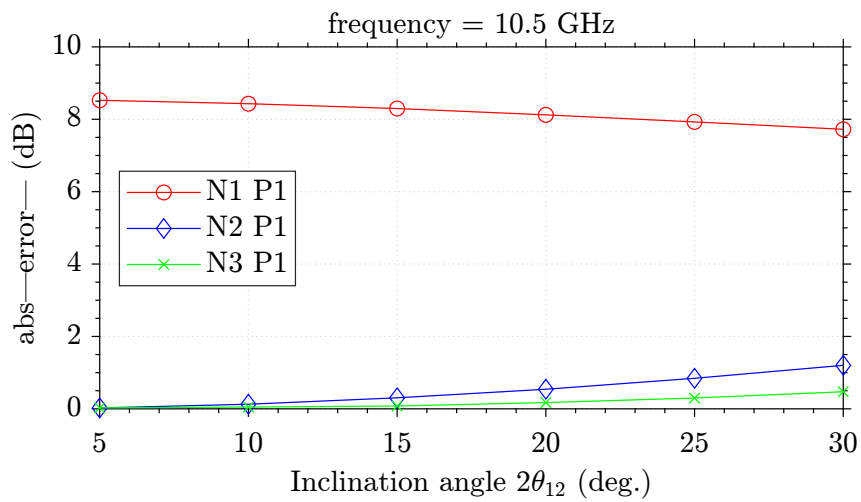


Figure 4.23: Absolute error for the configuration $\cos(n\phi)$, with $f = 10.5$ GHz.

Table 4.24: Results of the reflection coefficient for TE_{11}^z mode as a $\cos(n\phi)$ with $f = 11$ GHz and θ ($2\theta_{12}$) ranging from 5° to 30° , using Matlab algorithm (with $n = 1, 2$, and 3 and $p = 1$) and comparing with CST simulation.

θ	CST	Matlab $n = 1$ $p = 1$	Error $\Delta\%$	Matlab $n = 2$ $p = 1$	Error $\Delta\%$	Matlab $n = 3$ $p = 1$	Error $\Delta\%$
5	-57.7644	-66.0531	12.54%	-57.5290	0.40%	-57.4709	0.51%
10	-45.7473	-53.9368	15.18%	-45.6090	0.30%	-45.4296	0.69%
15	-38.7061	-46.7753	17.25%	-38.7523	0.11%	-38.3717	0.87%
20	-33.7315	-41.6297	18.97%	-34.0068	0.80%	-33.3017	1.29%
25	-29.8715	-37.5886	20.53%	-30.4506	1.90%	-29.3248	1.86%
30	-26.7264	-34.2559	21.98%	-27.6655	3.39%	-26.0228	2.70%

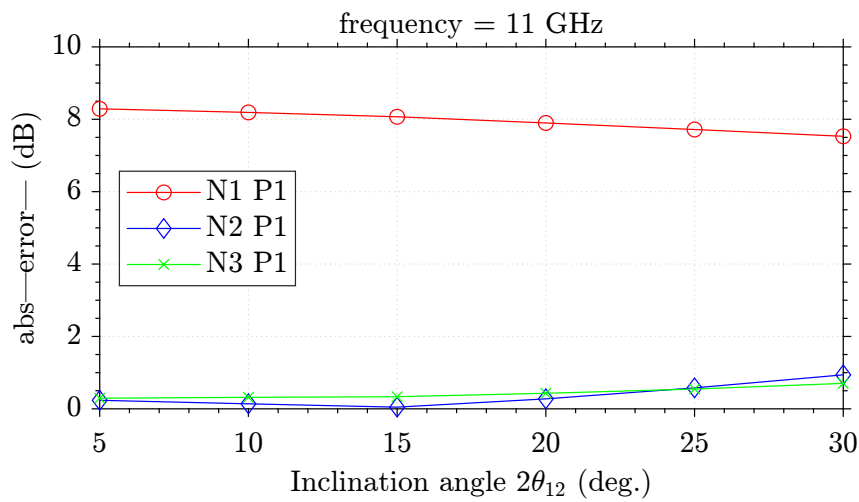


Figure 4.24: Absolute error for the configuration $\cos(n\phi)$, with $f = 11$ GHz.

Table 4.25: Results of the reflection coefficient for TE_{11}^z mode as a $\cos(n\phi)$ with $f = 11.5$ GHz and θ ($2\theta_{12}$) ranging from 5° to 30° , using Matlab algorithm (with $n = 1, 2$, and 3 and $p = 1$) and comparing with CST simulation.

θ	CST	Matlab $n = 1$ $p = 1$	Error $\Delta\%$	Matlab $n = 2$ $p = 1$	Error $\Delta\%$	Matlab $n = 3$ $p = 1$	Error $\Delta\%$
5	-58.7807	-66.81134	12.01%	-58.2520	0.90%	-58.1885	1.01%
10	-46.7493	-54.69773	14.53%	-46.3338	0.89%	-46.1539	1.29%
15	-39.7080	-47.54204	16.47%	-39.4733	0.59%	-39.0978	1.56%
20	-34.7216	-42.40253	18.11%	-34.7236	0.01%	-34.0415	1.99%
25	-30.8573	-38.36758	19.57%	-31.1598	0.97%	-30.0730	2.60%
30	-27.7077	-35.04081	20.92%	-28.3655	2.31%	-26.7882	3.43%

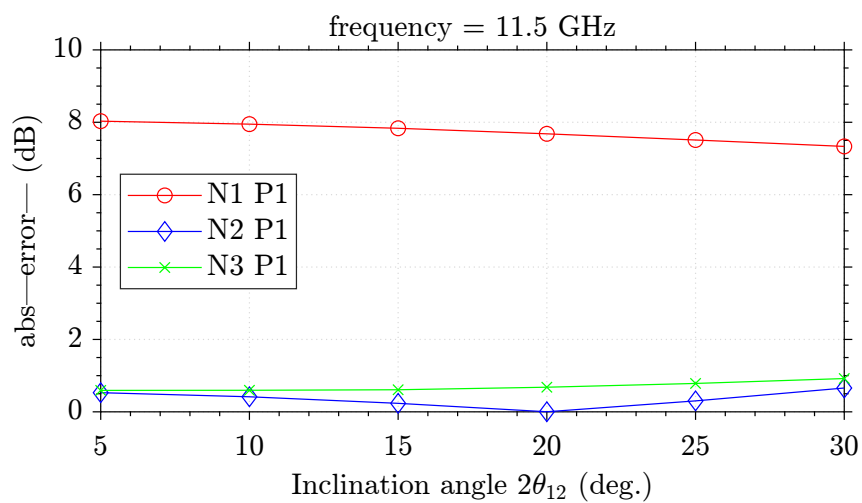


Figure 4.25: Absolute error for the configuration $\cos(n\phi)$, with $f = 11.5$ GHz.

Table 4.26: Results of the reflection coefficient for TE_{11}^z mode as a $\cos(n\phi)$ with $f = 12$ GHz and θ ($2\theta_{12}$) ranging from 5° to 30° , using Matlab algorithm (with $n = 1, 2$, and 3 and $p = 1$) and comparing with CST simulation.

θ	CST	Matlab $n = 1$ $p = 1$	Error $\Delta\%$	Matlab $n = 2$ $p = 1$	Error $\Delta\%$	Matlab $n = 3$ $p = 1$	Error $\Delta\%$
5	-59.5995	-67.3921	11.56%	-58.7789	1.39%	-58.7108	1.51%
10	-47.5619	-55.2818	13.96%	-46.8611	1.49%	-46.6837	1.88%
15	-40.5315	-48.1311	15.78%	-39.9961	1.33%	-39.6375	2.25%
20	-35.5287	-42.9974	17.37%	-35.2414	0.81%	-34.6055	2.66%
25	-31.6592	-38.9685	18.75%	-31.6761	0.05%	-30.6599	3.25%
30	-28.5033	-35.6475	20.04%	-28.8602	1.23%	-27.3586	4.18%

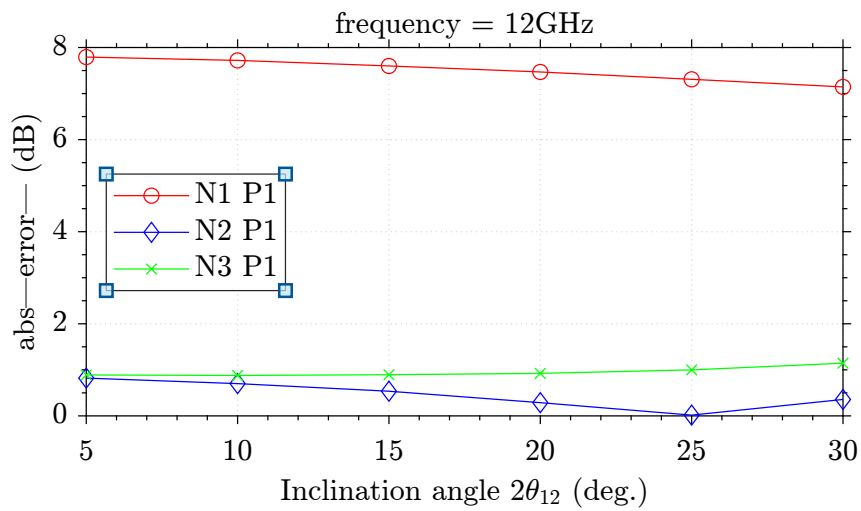


Figure 4.26: Absolute error for the configuration $\cos(n\phi)$, with $f = 12$ GHz.

Table 4.27: Results of the reflection coefficient for TE_{11}^z mode as a $\cos(n\phi)$ with $f = 12.5$ GHz and θ ($2\theta_{12}$) ranging from 5° to 30° , using Matlab algorithm (with $n = 1, 2$, and 3 and $p = 1$) and comparing with CST simulation.

θ	CST	Matlab $n = 1$ $p = 1$	Error $\Delta\%$	Matlab $n = 2$ $p = 1$	Error $\Delta\%$	Matlab $n = 3$ $p = 1$	Error $\Delta\%$
5	-60.2821	-67.8353	11.13%	-59.1346	1.94%	-59.0627	2.06%
10	-48.2440	-55.7282	13.42%	-47.2151	2.17%	-47.0441	2.55%
15	-41.2044	-48.5824	15.18%	-40.3451	2.12%	-40.0094	2.98%
20	-36.1940	-43.4542	16.70%	-35.5792	1.72%	-34.9881	3.44%
25	-32.3104	-39.4311	18.05%	-32.0015	0.96%	-31.0587	4.03%
30	-29.1352	-36.1157	19.32%	-29.1711	0.12%	-27.7759	4.89%

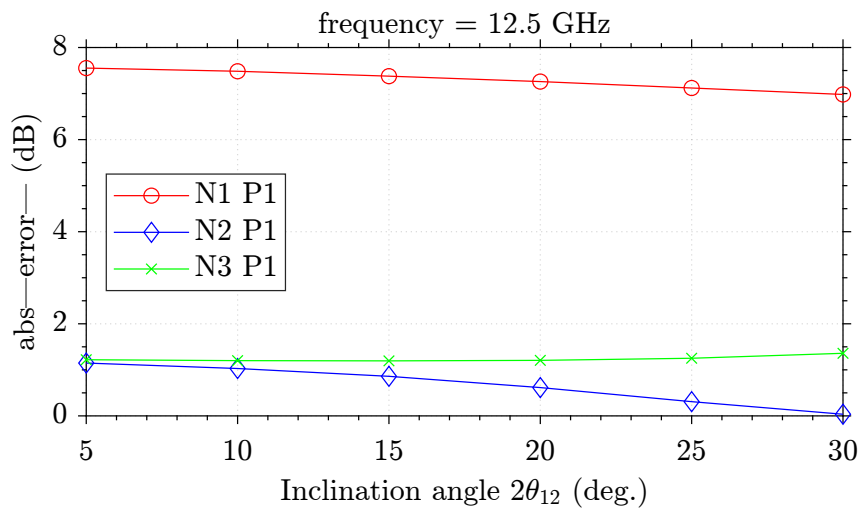


Figure 4.27: Absolute error for the configuration $\cos(n\phi)$, with $f = 12.5$ GHz.

Table 4.28: Results of the reflection coefficient for TE_{11}^z mode as a $\cos(n\phi)$ with $f = 13$ GHz and θ ($2\theta_{12}$) ranging from 5° to 30° , using Matlab algorithm (with $n = 1, 2$, and 3 and $p = 1$) and comparing with CST simulation.

θ	CST	Matlab $n = 1$ $p = 1$	Error $\Delta\%$	Matlab $n = 2$ $p = 1$	Error $\Delta\%$	Matlab $n = 3$ $p = 1$	Error $\Delta\%$
5	-60.8393	-68.1630	10.74%	-59.3099	2.57%	-59.2346	2.70%
10	-48.7895	-56.0589	12.96%	-47.3858	2.96%	-47.2255	3.31%
15	-41.7242	-48.9176	14.70%	-40.5063	3.00%	-40.1968	3.79%
20	-36.7071	-43.7949	16.18%	-35.7267	2.74%	-35.1904	4.30%
25	-32.7972	-39.7773	17.54%	-32.1228	2.09%	-31.2658	4.89%
30	-29.5861	-36.4672	18.86%	-29.2811	1.04%	-28.0165	5.60%

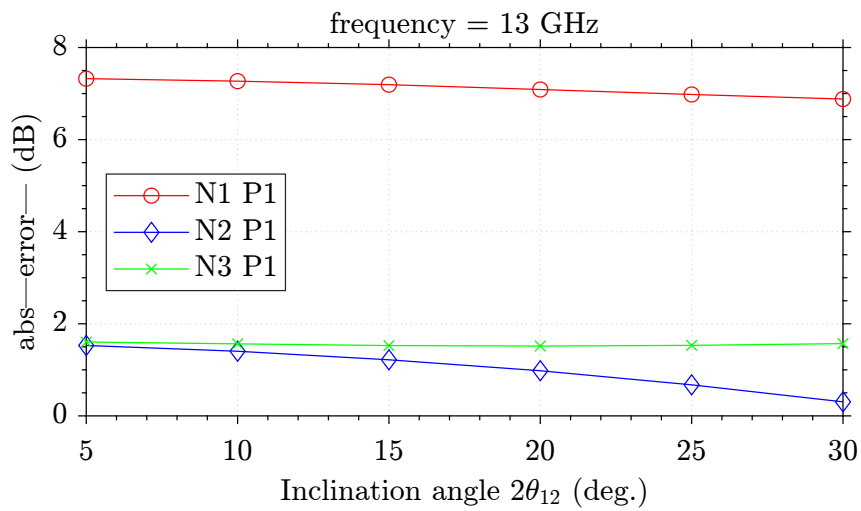


Figure 4.28: Absolute error for the configuration $\cos(n\phi)$, with $f = 13$ GHz.

Table 4.29: Results of the reflection coefficient for TE_{11}^z mode as a $\cos(n\phi)$ with $f = 13.5$ GHz and θ ($2\theta_{12}$) ranging from 5° to 30° , using Matlab algorithm (with $n = 1, 2$, and 3 and $p = 1$) and comparing with CST simulation.

θ	CST	Matlab $n = 1$ $p = 1$	Error $\Delta\%$	Matlab $n = 2$ $p = 1$	Error $\Delta\%$	Matlab $n = 3$ $p = 1$	Error $\Delta\%$
5	-61.1854	-68.3865	11.76%	-59.2348	3.18%	-59.1572	3.31%
10	-49.1113	-56.2852	14.60%	-47.3020	3.68%	-47.1512	3.99%
15	-42.0173	-49.1482	16.97%	-40.4069	3.83%	-40.1258	4.50%
20	-36.9788	-44.0307	19.06%	-35.6080	3.70%	-35.1268	5.00%
25	-33.0284	-40.0182	21.16%	-31.9779	3.18%	-31.2160	5.48%
30	-29.7647	-36.7133	23.34%	-29.1058	2.21%	-27.9816	5.99%

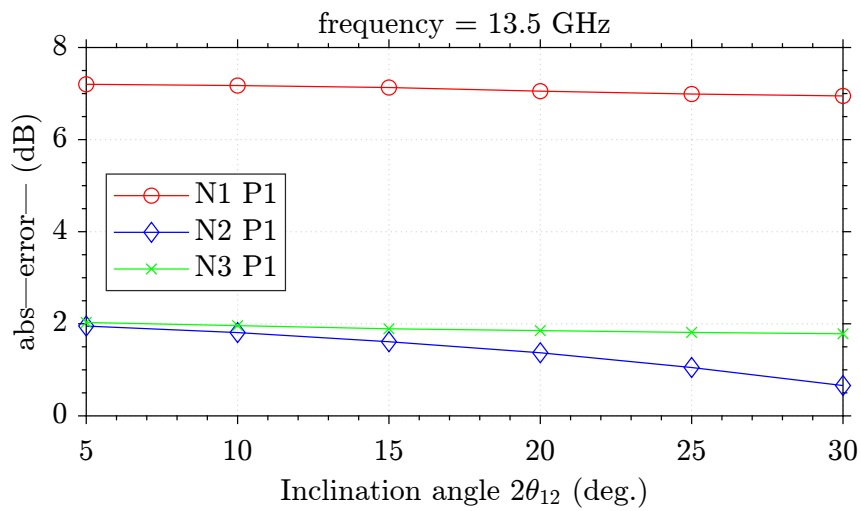


Figure 4.29: Absolute error for the configuration $\cos(n\phi)$, with $f = 13.5$ GHz.

Table 4.30: Results of the reflection coefficient for TE_{11}^z mode as a $\cos(n\phi)$ with $f = 14$ GHz and θ ($2\theta_{12}$) ranging from 5° to 30° , using Matlab algorithm (with $n = 1, 2$, and 3 and $p = 1$) and comparing with CST simulation.

θ	CST	Matlab $n = 1$ $p = 1$	Error $\Delta\%$	Matlab $n = 2$ $p = 1$	Error $\Delta\%$	Matlab $n = 3$ $p = 1$	Error $\Delta\%$
5	-61.0041	-68.5099	12.30%	-58.6114	3.92%	-58.5302	4.05%
10	-48.9130	-56.4113	15.32%	-46.6626	4.60%	-46.5153	4.90%
15	-41.7875	-49.2781	17.92%	-39.7440	4.89%	-39.4726	5.53%
20	-36.6877	-44.1654	20.38%	-34.9122	4.83%	-34.4465	6.10%
25	-32.6627	-40.1580	22.94%	-31.2414	4.35%	-30.5177	6.56%
30	-29.3029	-36.8574	25.78%	-28.3187	3.35%	-27.2640	6.95%

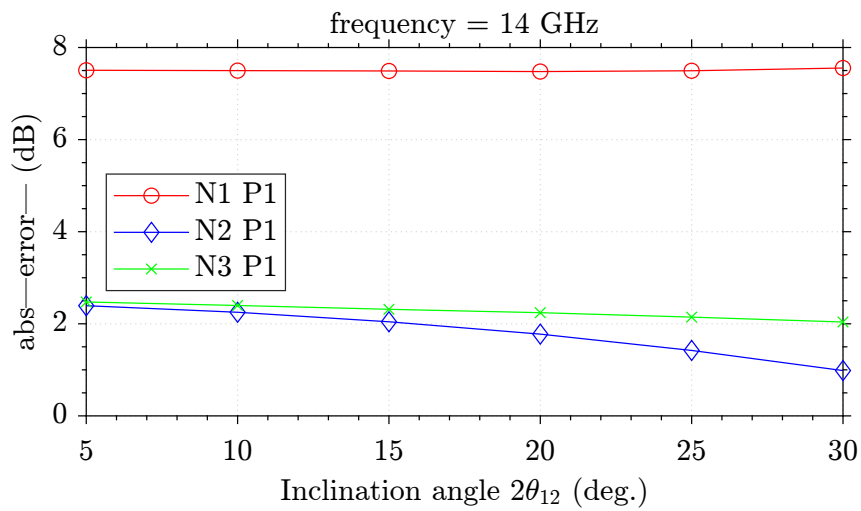


Figure 4.30: Absolute error for the configuration $\cos(n\phi)$, with $f = 14$ GHz.

Table 4.31: Results of the reflection coefficient for TE_{11}^z mode as a $\cos(n\phi)$ with $f = 14.5$ GHz and θ ($2\theta_{12}$) ranging from 5° to 30° , using Matlab algorithm (with $n = 1, 2$, and 3 and $p = 1$) and comparing with CST simulation.

θ	CST	Matlab $n = 1$ $p = 1$	Error $\Delta\%$	Matlab $n = 2$ $p = 1$	Error $\Delta\%$	Matlab $n = 3$ $p = 1$	Error $\Delta\%$
5	-56.9713	-68.5304	20.28%	-53.5585	5.99%	-53.4414	6.19%
10	-44.7625	-56.4340	26.07%	-41.6020	7.06%	-41.2832	7.77%
15	-37.4248	-49.3045	31.74%	-34.6902	7.30%	-34.0093	9.12%
20	-31.9817	-44.1963	38.19%	-29.8624	6.62%	-28.7157	10.21%
25	-27.4924	-40.1935	46.19%	-26.1803	4.77%	-24.4654	11.01%
30	-23.5031	-36.8976	56.99%	-23.2179	1.21%	-20.8390	11.33%

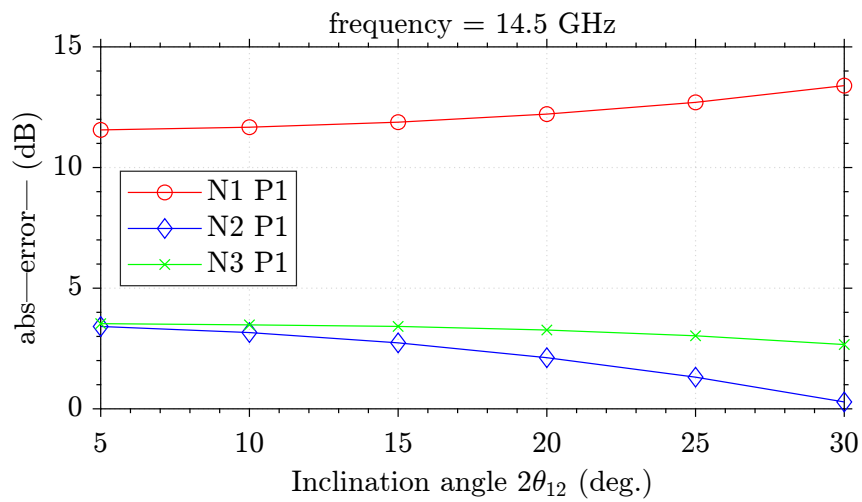


Figure 4.31: Absolute error for the configuration $\cos(n\phi)$, with $f = 14.5$ GHz.

Table 4.32: Results of the reflection coefficient for TE_{11}^z mode as a $\cos(n\phi)$ with $f = 15$ GHz and θ ($2\theta_{12}$) ranging from 5° to 30° , using Matlab algorithm (with $n = 1, 2$, and 3 and $p = 1$) and comparing with CST simulation.

θ	CST	Matlab $n = 1$ $p = 1$	Error $\Delta\%$	Matlab $n = 2$ $p = 1$	Error $\Delta\%$	Matlab $n = 3$ $p = 1$	Error $\Delta\%$
5	-66.1701	-68.4378	3.42%	-53.9895	18.40%	-53.9406	18.48%
10	-54.2230	-56.3432	3.91%	-42.0059	22.53%	-41.9129	22.70%
15	-47.2587	-49.2173	4.14%	-35.0386	25.85%	-34.8743	26.20%
20	-42.3369	-44.1129	4.19%	-30.1426	28.80%	-29.8787	29.42%
25	-38.5865	-40.1146	3.96%	-26.3950	31.59%	-26.0041	32.60%
30	-35.5770	-36.8234	3.50%	-23.3840	34.27%	-22.8417	35.79%

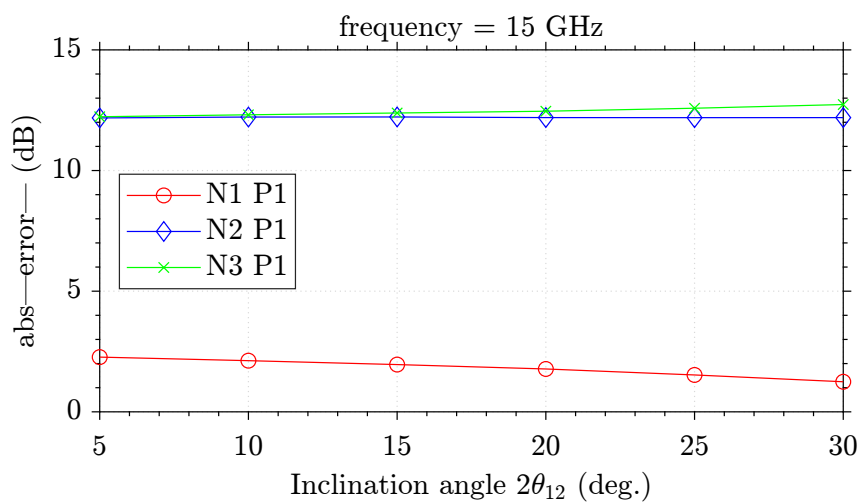


Figure 4.32: Absolute error for the configuration $\cos(n\phi)$, with $f = 15$ GHz.

Table 4.33: Results of the reflection coefficient for TE_{11}^z mode as a $\sin(n\phi)$ with $f = 10$ GHz and θ ($2\theta_{12}$) ranging from 5° to 30° , using Matlab algorithm (with $n = 1, 2$, and 3 and $p = 1$) and comparing with CST simulation.

θ	CST	Matlab $n = 1$ $p = 1$	Error $\Delta\%$	Matlab $n = 2$ $p = 1$	Error $\Delta\%$	Matlab $n = 3$ $p = 1$	Error $\Delta\%$
5	-56.5396	-51.8239	8.34%	-53.4275	5.50%	-53.4221	5.51%
10	-44.3731	-39.7949	10.31%	-41.3269	6.86%	-41.3356	6.84%
15	-37.2632	-32.7682	12.06%	-34.2075	8.20%	-34.2376	8.11%
20	-32.1692	-27.7873	13.62%	-29.1111	9.50%	-29.1628	9.34%
25	-28.1792	-23.9212	15.11%	-25.1144	10.87%	-25.1826	10.63%
30	-24.8764	-20.7511	16.58%	-21.8106	12.32%	-21.8913	11.99%

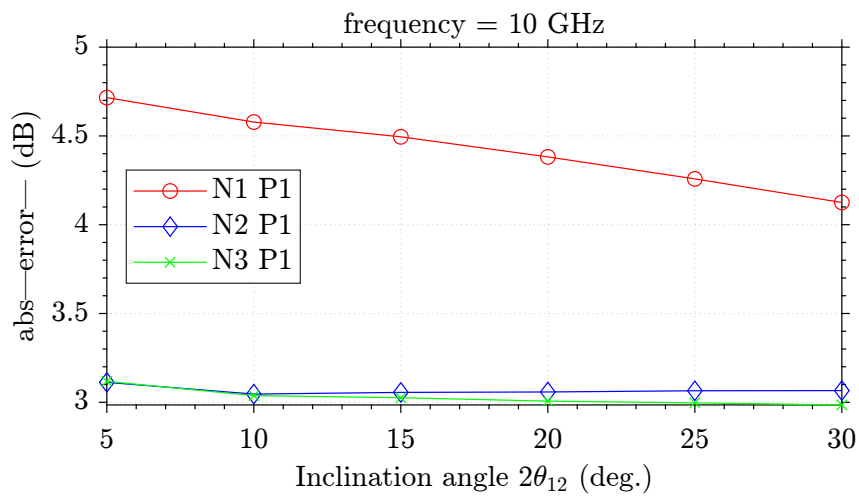


Figure 4.33: Absolute error for the configuration $\sin(n\phi)$, with $f = 10$ GHz.

Table 4.34: Results of the reflection coefficient for TE_{11}^z mode as a $\sin(n\phi)$ with $f = 10.5$ GHz and θ ($2\theta_{12}$) ranging from 5° to 30° , using Matlab algorithm (with $n = 1, 2$, and 3 and $p = 1$) and comparing with CST simulation.

θ	CST	Matlab $n = 1$ $p = 1$	Error $\Delta\%$	Matlab $n = 2$ $p = 1$	Error $\Delta\%$	Matlab $n = 3$ $p = 1$	Error $\Delta\%$
5	-54.0413	-50.9334	5.75%	-51.8786	4.00%	-51.8717	4.01%
10	-41.9789	-38.8678	7.41%	-39.7627	5.27%	-39.7641	5.27%
15	-34.8580	-31.7811	8.82%	-32.6123	6.44%	-32.6256	6.40%
20	-29.7527	-26.7191	10.19%	-27.4735	7.66%	-27.4952	7.58%
25	-25.7346	-22.7540	11.58%	-23.4249	8.97%	-23.4444	8.89%
30	-22.3943	-19.4713	13.05%	-20.0600	10.42%	-20.0815	10.32%

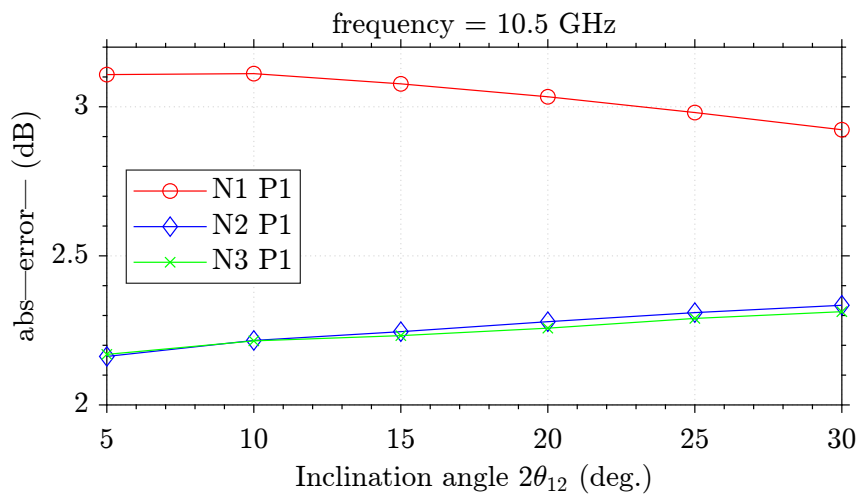


Figure 4.34: Absolute error for the configuration $\sin(n\phi)$, with $f = 10.5$ GHz.

Table 4.35: Results of the reflection coefficient for TE_{11}^z mode as a $\sin(n\phi)$ with $f = 11$ GHz and θ ($2\theta_{12}$) ranging from 5° to 30° , using Matlab algorithm (with $n = 1, 2$, and 3 and $p = 1$) and comparing with CST simulation.

θ	CST	Matlab $n = 1$ $p = 1$	Error $\Delta\%$	Matlab $n = 2$ $p = 1$	Error $\Delta\%$	Matlab $n = 3$ $p = 1$	Error $\Delta\%$
5	-50.1684	-48.4147	3.49%	-48.9597	2.40%	-48.9543	2.42%
10	-38.1259	-36.3091	4.76%	-36.8148	3.43%	-36.8159	3.43%
15	-30.9851	-29.1584	5.89%	-29.6130	4.42%	-29.6212	4.40%
20	-25.8538	-24.0132	7.11%	-24.4077	5.59%	-24.4199	5.54%
25	-21.8014	-19.9522	8.48%	-20.2833	6.96%	-20.2885	6.93%
30	-18.4239	-16.5698	10.06%	-16.8393	8.60%	-16.8305	8.64%

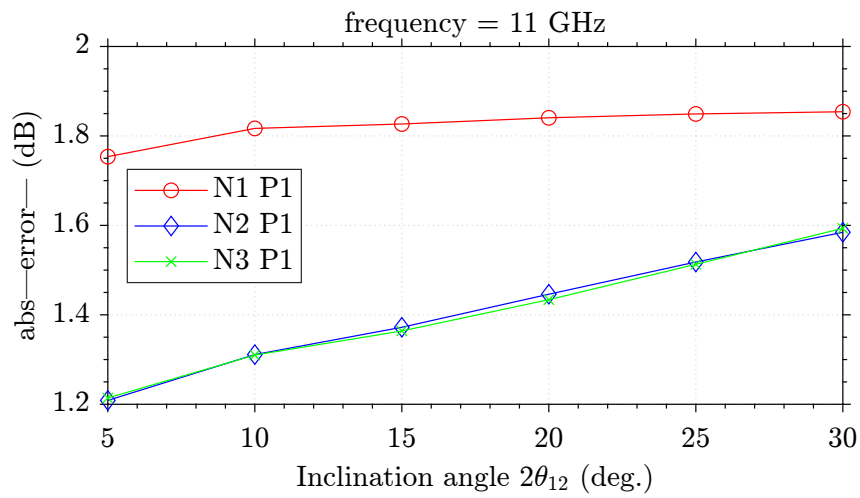


Figure 4.35: Absolute error for the configuration $\sin(n\phi)$, with $f = 11$ GHz.

Table 4.36: Results of the reflection coefficient for TE_{11}^z mode as a $\sin(n\phi)$ with $f = 11.5$ GHz and θ ($2\theta_{12}$) ranging from 5° to 30° , using Matlab algorithm (with $n = 1, 2$, and 3 and $p = 1$) and comparing with CST simulation.

θ	CST	Matlab $n = 1$ $p = 1$	Error $\Delta\%$	Matlab $n = 2$ $p = 1$	Error $\Delta\%$	Matlab $n = 3$ $p = 1$	Error $\Delta\%$
5	-36.3409	-35.9744	1.00%	-35.5954	2.05%	-35.5921	2.06%
10	-24.6505	-24.2345	1.68%	-23.8379	3.29%	-23.8266	3.34%
15	-18.1631	-17.6450	2.85%	-17.2405	5.07%	-17.2103	5.24%
20	-13.8862	-13.1997	4.94%	-12.8323	7.58%	-12.7676	8.05%
25	-10.8593	-9.9511	8.36%	-9.7263	10.43%	-9.6076	11.52%
30	-8.63290	-7.5536	12.50%	-7.6078	11.87%	-7.4393	13.82%

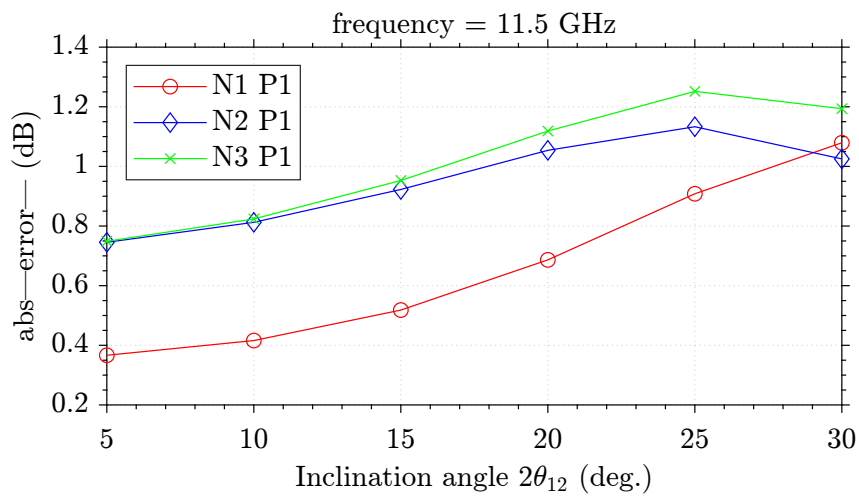


Figure 4.36: Absolute error for the configuration $\sin(n\phi)$, with $f = 11.5$ GHz.

Table 4.37: Results of the reflection coefficient for TE_{11}^z mode as a $\sin(n\phi)$ with $f = 12$ GHz and θ ($2\theta_{12}$) ranging from 5° to 30° , using Matlab algorithm (with $n = 1, 2$, and 3 and $p = 1$) and comparing with CST simulation.

θ	CST	Matlab $n = 1$ $p = 1$	Error $\Delta\%$	Matlab $n = 2$ $p = 1$	Error $\Delta\%$	Matlab $n = 3$ $p = 1$	Error $\Delta\%$
5	-49.4170	-47.9491	2.97%	-46.5507	5.80%	-46.5386	5.82%
10	-37.4759	-35.8998	4.20%	-34.5234	7.87%	-34.4891	7.96%
15	-30.537	-28.8378	5.56%	-27.5084	9.91%	-27.4324	10.16%
20	-25.6888	-23.8071	7.32%	-22.5482	12.22%	-22.4026	12.79%
25	-21.9982	-19.8796	9.63%	-18.7132	14.93%	-18.4782	16.00%
30	-19.0530	-16.6432	12.64%	-15.5899	18.17%	-15.2301	20.06%

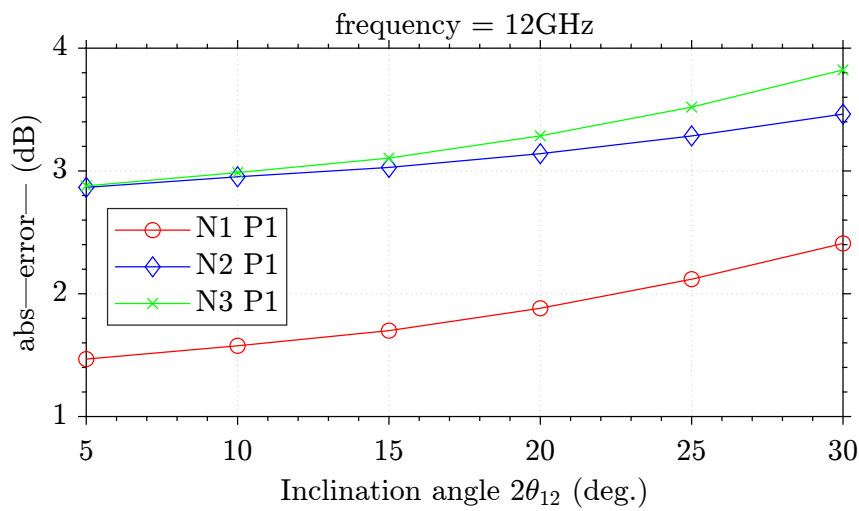


Figure 4.37: Absolute error for the configuration $\sin(n\phi)$, with $f = 12$ GHz.

Table 4.38: Results of the reflection coefficient for TE_{11}^z mode as a $\sin(n\phi)$ with $f = 12.5$ GHz and θ ($2\theta_{12}$) ranging from 5° to 30° , using Matlab algorithm (with $n = 1, 2$, and 3 and $p = 1$) and comparing with CST simulation.

θ	CST	Matlab $n = 1$ $p = 1$	Error $\Delta\%$	Matlab $n = 2$ $p = 1$	Error $\Delta\%$	Matlab $n = 3$ $p = 1$	Error $\Delta\%$
5	-52.4460	-50.3721	3.95%	-48.5765	7.37%	-48.5605	7.40%
10	-40.4250	-38.2832	5.29%	-36.5269	9.64%	-36.4862	9.74%
15	-33.4341	-31.1568	6.81%	-29.4764	11.83%	-29.3900	12.09%
20	-28.5322	-26.0402	8.73%	-24.4674	14.24%	-24.3036	14.82%
25	-24.7777	-22.0097	11.17%	-20.5702	16.98%	-20.3122	18.02%
30	-21.7554	-18.6587	14.23%	-17.3691	20.16%	-16.9765	21.96%

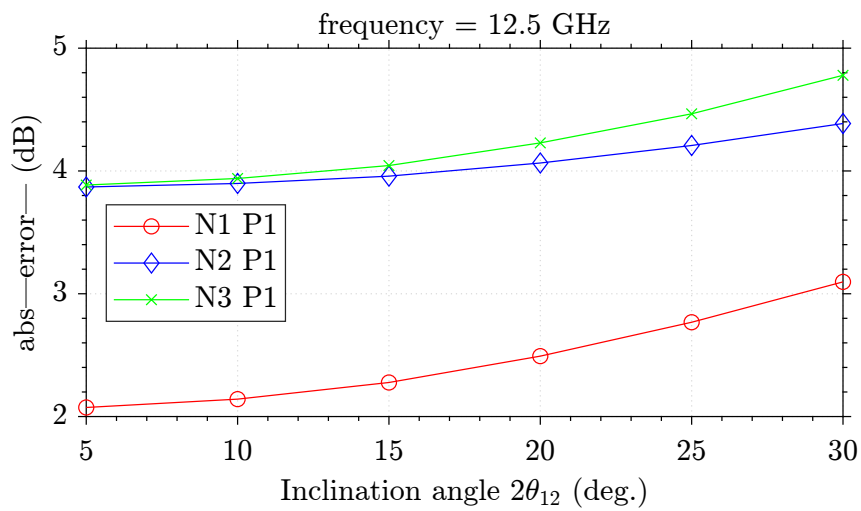


Figure 4.38: Absolute error for the configuration $\sin(n\phi)$, with $f = 12.5$ GHz.

Table 4.39: Results of the reflection coefficient for TE_{11}^z mode as a $\sin(n\phi)$ with $f = 13$ GHz and θ ($2\theta_{12}$) ranging from 5° to 30° , using Matlab algorithm (with $n = 1, 2$, and 3 and $p = 1$) and comparing with CST simulation.

θ	CST	Matlab $n = 1$ $p = 1$	Error $\Delta\%$	Matlab $n = 2$ $p = 1$	Error $\Delta\%$	Matlab $n = 3$ $p = 1$	Error $\Delta\%$
5	-54.2802	-51.7205	4.71%	-49.6568	8.51%	-49.6376	8.55%
10	-42.1496	-39.6047	6.03%	-37.5920	10.81%	-37.5484	10.91%
15	-35.1509	-32.4339	7.72%	-30.5174	13.18%	-30.4280	13.43%
20	-30.2060	-27.2566	9.76%	-25.4748	15.66%	-25.3115	16.20%
25	-26.4087	-23.1516	12.33%	-21.5331	18.46%	-21.2710	19.45%
30	-23.3373	-19.7155	15.51%	-18.2764	21.68%	-17.8874	23.35%

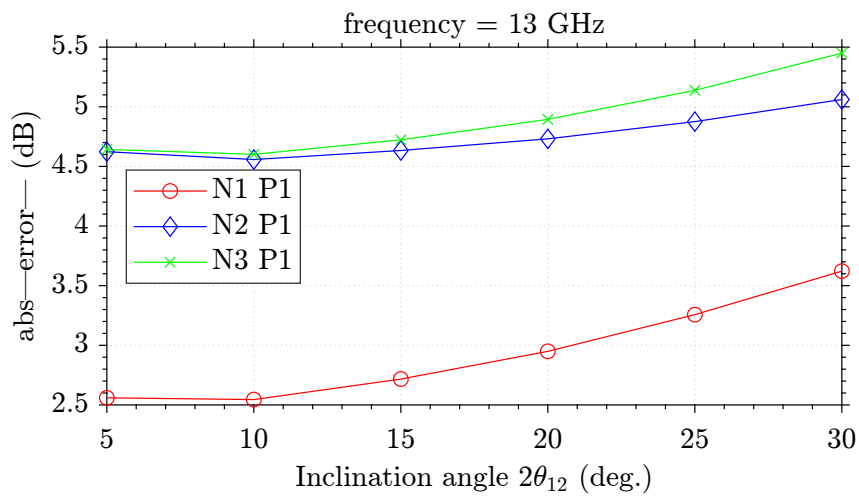


Figure 4.39: Absolute error for the configuration $\sin(n\phi)$, with $f = 13$ GHz.

Table 4.40: Results of the reflection coefficient for TE_{11}^z mode as a $\sin(n\phi)$ with $f = 13.5$ GHz and θ ($2\theta_{12}$) ranging from 5° to 30° , using Matlab algorithm (with $n = 1, 2$, and 3 and $p = 1$) and comparing with CST simulation.

θ	CST	Matlab $n = 1$ $p = 1$	Error $\Delta\%$	Matlab $n = 2$ $p = 1$	Error $\Delta\%$	Matlab $n = 3$ $p = 1$	Error $\Delta\%$
5	-55.4273	-52.6227	5.05%	-50.3375	9.18%	-50.3142	9.22%
10	-43.3269	-40.4839	6.56%	-38.2588	11.69%	-38.2131	11.80%
15	-36.3198	-33.2746	8.38%	-31.1619	14.20%	-31.0732	14.44%
20	-31.3407	-28.0437	10.51%	-26.0875	16.76%	-25.9279	17.27%
25	-27.4957	-23.8715	13.18%	-22.1025	19.61%	-21.8499	20.53%
30	-24.3660	-20.3577	16.45%	-18.7919	22.87%	-18.4202	24.40%

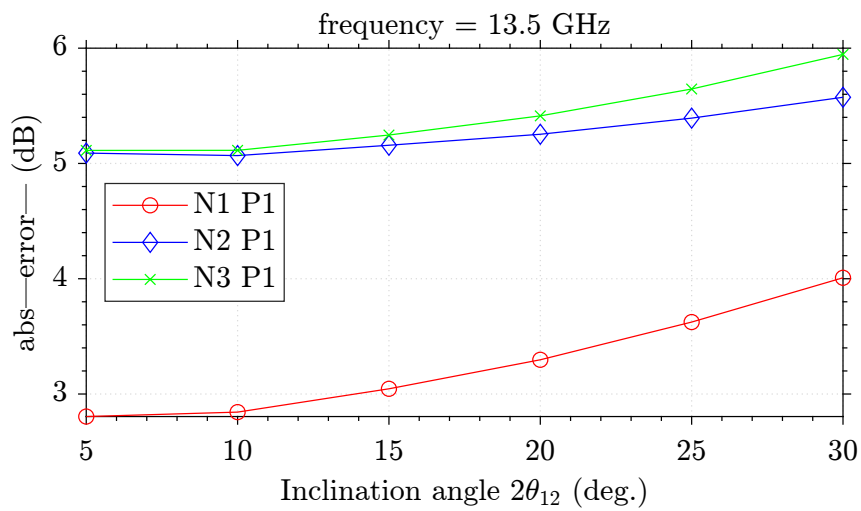


Figure 4.40: Absolute error for the configuration $\sin(n\phi)$, with $f = 13.5$ GHz.

Table 4.41: Results of the reflection coefficient for TE_{11}^z mode as a $\sin(n\phi)$ with $f = 14$ GHz and θ ($2\theta_{12}$) ranging from 5° to 30° , using Matlab algorithm (with $n = 1, 2$, and 3 and $p = 1$) and comparing with CST simulation.

θ	CST	Matlab $n = 1$ $p = 1$	Error $\Delta\%$	Matlab $n = 2$ $p = 1$	Error $\Delta\%$	Matlab $n = 3$ $p = 1$	Error $\Delta\%$
5	-56.1095	-53.2811	5.04%	-50.7385	9.57%	-50.7085	9.62%
10	-44.1459	-41.1208	6.85%	-38.6473	12.45%	-38.5966	12.57%
15	-37.0917	-33.8749	8.67%	-31.5296	14.99%	-31.4388	15.24%
20	-32.0709	-28.5923	10.84%	-26.4227	17.61%	-26.2649	18.10%
25	-28.1511	-24.3546	13.48%	-22.3948	20.44%	-22.1514	21.31%
30	-24.9228	-20.7637	16.68%	-19.0270	23.65%	-18.6811	25.04%

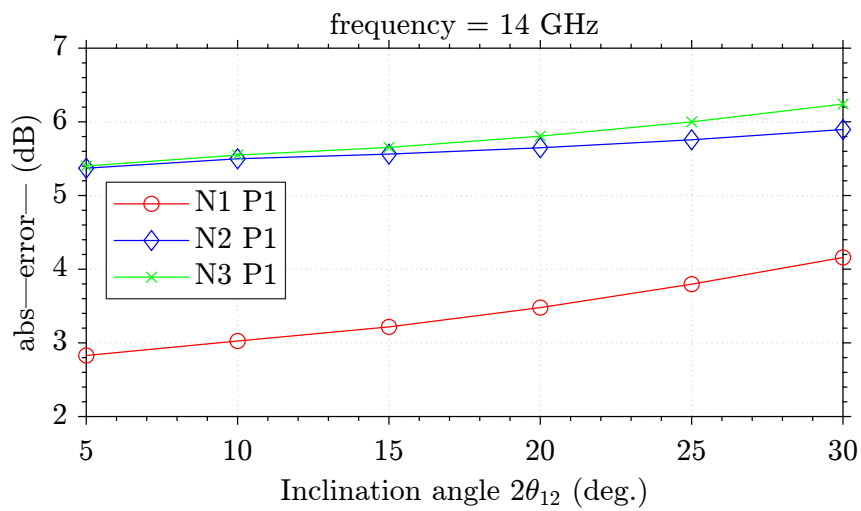


Figure 4.41: Absolute error for the configuration $\sin(n\phi)$, with $f = 14$ GHz.

Table 4.42: Results of the reflection coefficient for TE_{11}^z mode as a $\sin(n\phi)$ with $f = 14.5$ GHz and θ ($2\theta_{12}$) ranging from 5° to 30° , using Matlab algorithm (with $n = 1, 2$, and 3 and $p = 1$) and comparing with CST simulation.

θ	CST	Matlab $n = 1$ $p = 1$	Error $\Delta\%$	Matlab $n = 2$ $p = 1$	Error $\Delta\%$	Matlab $n = 3$ $p = 1$	Error $\Delta\%$
5	-55.4519	-53.7868	3.00%	-49.6914	10.38%	-49.6279	10.50%
10	-43.4413	-41.6055	4.22%	-37.6377	13.35%	-37.4941	13.69%
15	-36.1927	-34.3233	5.16%	-30.5721	15.52%	-30.2988	16.28%
20	-30.914	-28.9888	6.22%	-25.5176	17.45%	-25.0666	18.91%
25	-26.6462	-24.6840	7.36%	-21.5284	19.20%	-20.8818	21.63%
30	-22.9735	-21.0135	8.53%	-18.1710	20.90%	-17.3457	24.49%

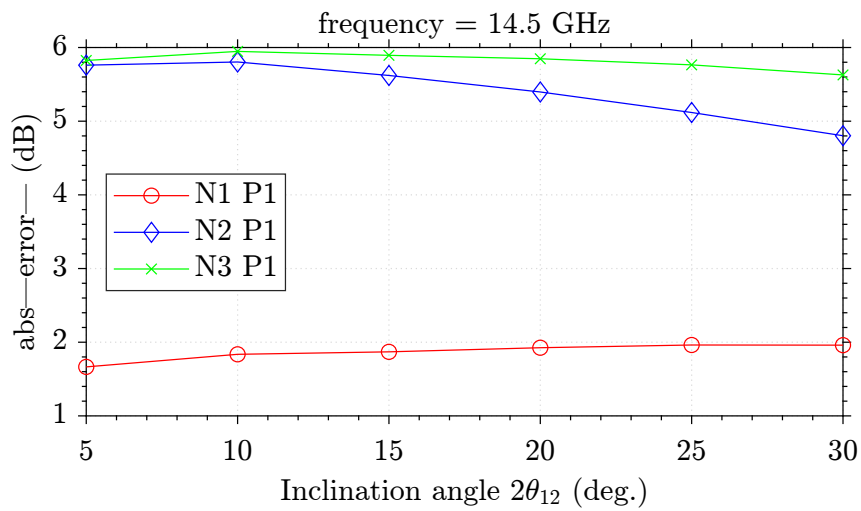


Figure 4.42: Absolute error for the configuration $\sin(n\phi)$, with $f = 14.5$ GHz.

Table 4.43: Results of the reflection coefficient for TE_{11}^z mode as a $\sin(n\phi)$ with $f = 15$ GHz and θ ($2\theta_{12}$) ranging from 5° to 30° , using Matlab algorithm (with $n = 1, 2$, and 3 and $p = 1$) and comparing with CST simulation.

θ	CST	Matlab $n = 1$ $p = 1$	Error $\Delta\%$	Matlab $n = 2$ $p = 1$	Error $\Delta\%$	Matlab $n = 3$ $p = 1$	Error $\Delta\%$
5	-60.0475	-54.1888	9.75%	-48.9636	18.45%	-48.9399	18.49%
10	-48.0063	-41.9865	12.53%	-36.8742	23.18%	-36.8307	23.27%
15	-40.9661	-34.6674	15.37%	-29.7529	27.37%	-29.6764	27.55%
20	-35.9690	-29.2788	18.59%	-24.6323	31.51%	-24.5127	31.85%
25	-32.0640	-24.9031	22.33%	-20.5739	35.83%	-20.4086	36.35%
30	-28.8078	-21.1479	26.58%	-17.1540	40.45%	-16.9454	41.17%

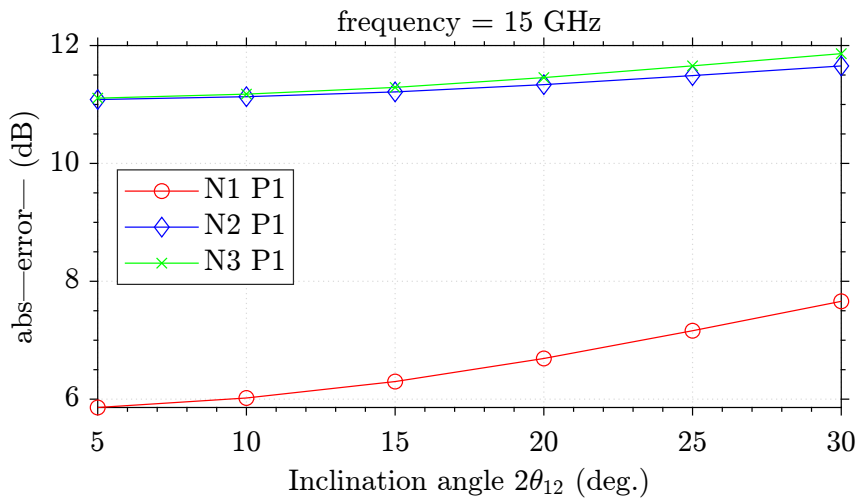


Figure 4.43: Absolute error for the configuration $\sin(n\phi)$, with $f = 15$ GHz.

Analyzing Figs. 4.22–4.32, we can observe that as the frequency and the angle increases, the configuration with better results for TE_{11}^z as a $\cos(n\phi)$ changes from $n = 3$ and $p = 1$ to $n = 2$ and $p = 1$, i.e. we have more precision with a smaller number of modes. This may be happening due to a limited number of p -terms used in our simulations. Also, when we have a frequency of 15 GHz, we have the worst case of precision, with high errors for the three set of modes used. The same occurs when we take the results for TE_{11}^z as a $\sin(n\phi)$, from Figs. 4.33–4.43 we can verify that the configuration with less number of modes ($n = 1$ and $p = 1$) have the minor absolute error for higher frequencies and smaller angles. And again, the biggest errors occurs when we have a frequency of 15 GHz.

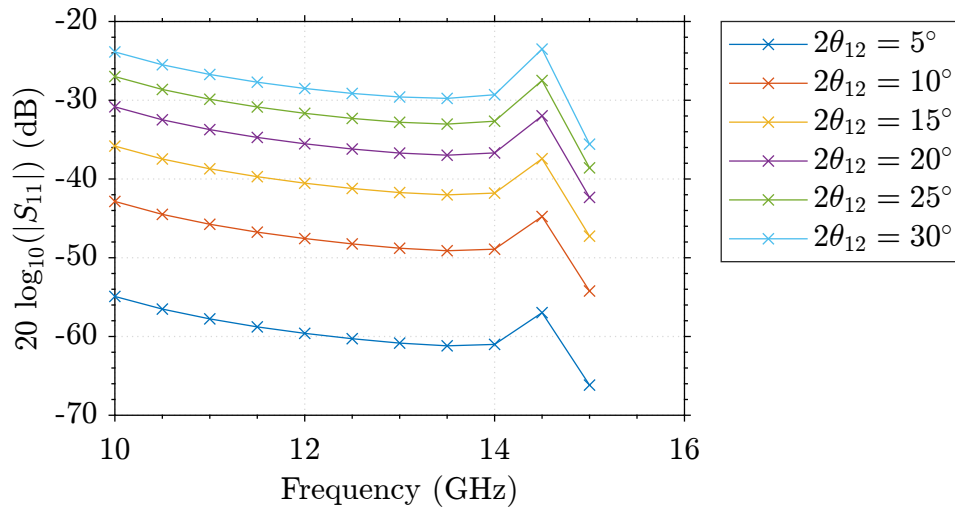


Figure 4.44: Reflection coefficient from CST for $TE_{11}^z = \cos(n\phi)$.

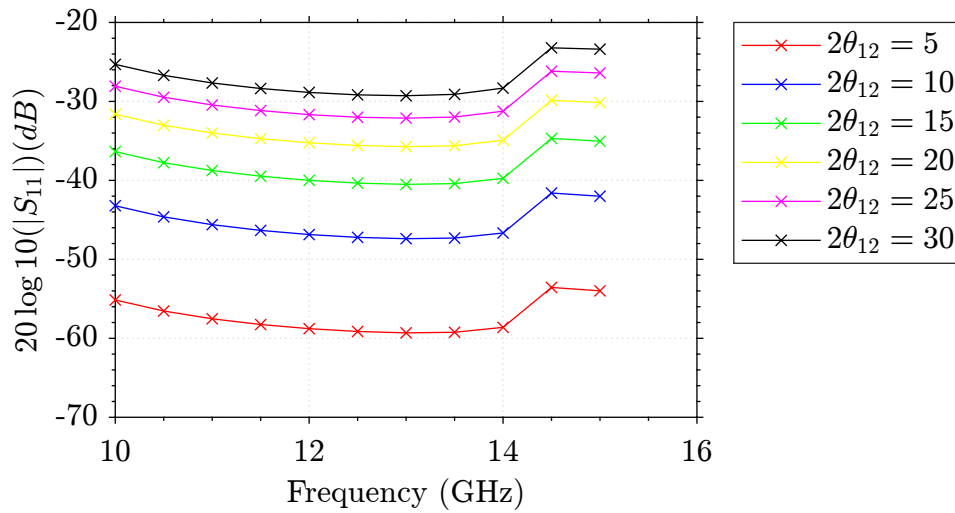


Figure 4.45: Reflection coefficient from our algorithm ($n = 2$ and $p = 1$) for $TE_{11}^z = \cos(n\phi)$.

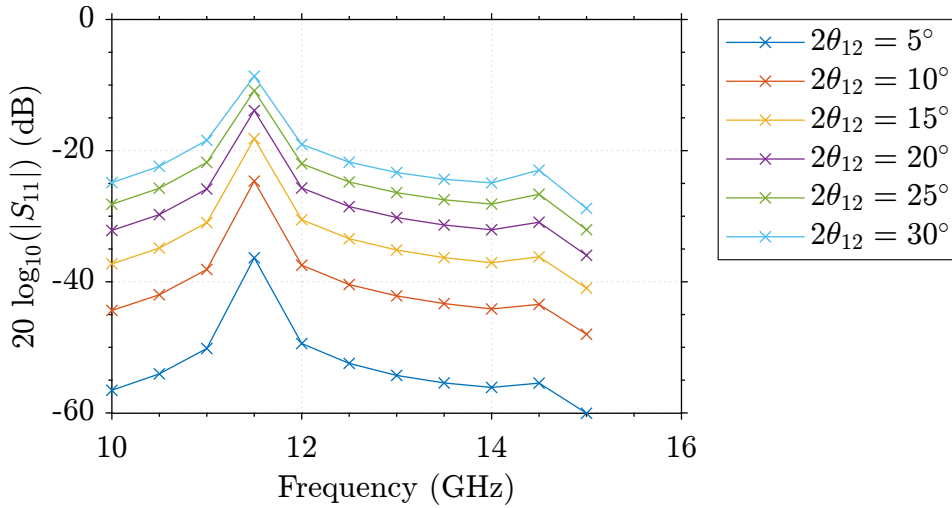


Figure 4.46: Reflection coefficient from CST for $TE_{11}^z = \sin(n\phi)$.

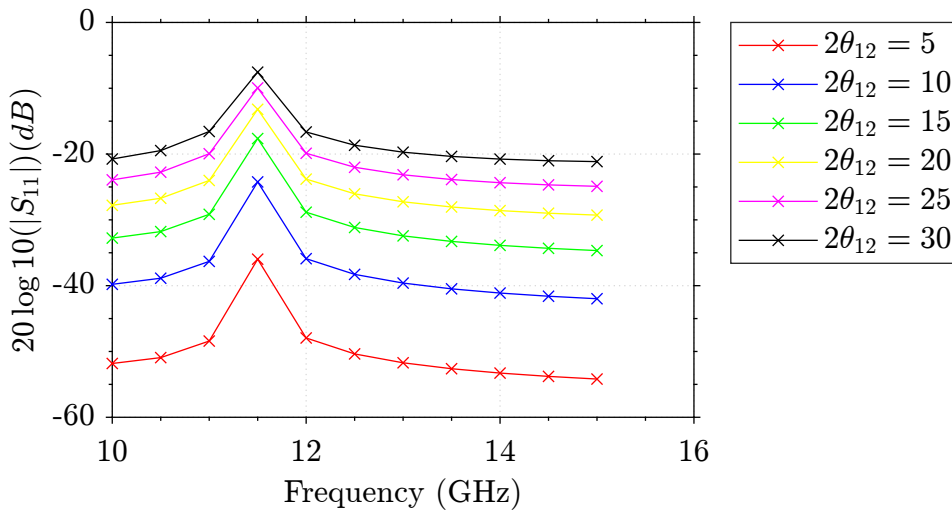


Figure 4.47: Reflection coefficient from our algorithm ($n = 1$ and $p = 1$) for $TE_{11}^z = \sin(n\phi)$.

Figs 4.44 and 4.45 compiles the results for all frequencies from CST and from our algorithm (for $n = 2$ and $p = 1$), respectively, for TE_{11}^z as a $\cos(n\phi)$. The same is exposed in Figs. 4.46 and 4.47, from CST and from our algorithm (for $n = 1$ and $p = 1$) for TE_{11}^z as a $\sin(n\phi)$. Despite the observed error we can notice that, except when the frequency is close to 15 GHz, both answers from our algorithm presents the same behavior as the CST responses.

5 Conclusion

In this final chapter, will be presented a review and a resume about the topics addressed in this research, by commenting the results obtained and making suggestions to future works.

In Chapter 1, we briefly discuss about how the evolution of technology in the area of communications systems eventually generated a need to use devices with connections made by curved transmission lines, often miniaturized. Thus, the need for knowledge of the behavior and modeling of electromagnetic field propagation in curved waveguides has become a subject of relevant importance. Since, depending on the geometry of the problem, some cases of transmission lines do not have a simple solution, it has become necessary to conduct studies for computational modeling of electromagnetic fields in regions of discontinuity in transmission lines. The numerical methods normally used to analyze geometries with complex shapes are based on the solution of Maxwell's equations in a brute force way, based on the discretisation of the 3D domain, but these methods demands high computational resources to obtain accurate answers, so that limitations of RAM memory and CPU processing speed may prevent an improvement of solutions by these cited techniques. Thus, the object of study of the present study was a semi-analytical approach which have a lower computational cost to model waveguide segment junctions considering along oblique surfaces. Thus, the focus of the work consisted in modeling and analyzing the reflection coefficient at oblique junctions of cylindrical waveguides through a solution based on MMT and by computing the GSM associated with each junction.

In Chapter 2, we briefly discuss the mathematical formulation for representing electromagnetic fields in cylindrical coordinates. Through a review of the literature, we present the cylindrical harmonics that solve the boundary values problems of TE and TM field configurations and thus we define the cutoff frequencies and the associated propagation constants of circular waveguides..

In Chapter 3, we presented our MMT formulation along oblique surfaces in terms of reaction integrals. Thus, in this chapter, the reaction integrals were developed to deal with modal coupling in the region of interest and we

obtain the GSM matrix. Also, we present a procedure to cascade a pair of GSM matrices in order to perform analysis of more complex structures formed by the subsequent junction of three or more waveguide segments. Besides this, a numerical algorithm was implemented in the Matlab platform in order to validate the capabilities of the mathematical model presented. The results obtained through the Matlab simulations of our approach were compared with the results obtained for the analysis of the same problem using the commercial CST Studio Suite software.

In Chapter 4, the numerical results of the application of our MMT are presented. We presented results for the reflection coefficient in decibel of the dominant mode versus the frequency and, in cases where guides with oblique junctions were explored, we present the curves of the reflection coefficient versus the oblique junction angle, given a fixed operating frequency. Initially, we performed tests in different scenarios for direct junctions between segments of curvatureless (straight) waveguides in order to verify and ensure the functionality and convergence of the developed method. In these tests, we varied frequency, electromagnetic characteristics, and explored the cascading of waveguide segments. When comparing the results obtained in these initial tests with those obtained by the model in FEM results from CST, we can observe the convergence and the accuracy of the method even using a minimum number of modes for the solution. After ensuring that the method works properly, scenarios where oblique junctions existed between two waveguide segments were analyzed. Since the existence of an angular junction between two waveguides generates a discontinuity where the higher modes end up interacting with the propagating mode, tests were performed considering two situations for the fundamental mode: the first one for an input excitation of the $\sin(n\phi)$ type and the second one considering an input in the $\cos(n\phi)$ form. To calibrate the algorithm, tests were performed varying the number of modes used to analyze the problem. The results for the tests were different for each of the situations explored. The results for the input in the $\sin(n\phi)$ form showed a good accuracy of the method, guaranteeing very small errors for angulations up to 60° . On the other hand, the results for the input in the $\cos(n\phi)$ format presented larger errors, but constant, for angulations up to 60° and, despite the errors, the behavior was the same as expected by the basis of comparison. As a guess for the constant error, we suspect that they may be caused by some numerical integration error that degenerates the accuracy of the MMT.

The scientific contribution of this work consists in the application of the MMT in oblique junctions of circular waveguides, so that the results obtained in this work have not been previously found in the literature. It is important to

note that the oblique junctions analyzed in this work consist of abrupt angular deformations and that practical cases would require a specific adaptation and modeling that can be performed, for example, via GSM matrix cascading.

For future work, we recommend the implementation of the developed equations in a different mathematical application software in order to verify the continuity of the numerical error found for one of the curved guide solutions. In addition, we suggest the real curvature analysis of waveguides through an approximation made by discretization and cascading of the curvature at oblique junctions presented in this work.

Bibliography

- [1] "Microwave engineering corporation," <https://microwaveeng.com/product/circular-waveguide/>.
- [2] C. A. Balanis, *Antenna Theory: Analysis and Design*. Wiley-Interscience, 2005.
- [3] "Qualwave website," <http://www.qualwave.com/resources/circular-waveguide-sizes.htm>.
- [4] Y. Wang and D. Dai, "Ultra-sharp multimode waveguide bends with dual polarizations," *J. Lightw. Technol.*, vol. 38, no. 15, pp. 3994–3999, 2020.
- [5] N. C. F. Foglia Manzillo, R. Sauleau and M. Ettore, "Mode matching analysis of an e-plane 90° bend with a square step in parallel-plate waveguide," *IEEE Antennas and Wireless Propagation Letters*, vol. 16, no. 2, pp. 2187–2190, Aug. 2017.
- [6] L. Biniashvili, "Eliminating Reflections in Waveguide Bends Using a Metagrating-Inspired Semianalytical Methodology," *IEEE Transactions on Antennas and Propagation*, vol. 70, no. 2, pp. 1221–1235, Feb 2022.
- [7] H.-W. Chang and W.-C. Cheng, "Analysis of Dielectric Waveguide Termination with Tilted Facets by Analytic Continuity Method," *Journal of Electromagnetic Waves and Applications*, pp. 1653–1662, 2007.
- [8] C. S. Lavranos and G. A. Kyriacou, "Eigenvalue analysis of curved waveguides employing an orthogonal curvilinear frequency-domain finite-difference method," *IEEE Trans. Microw. Theory Techn.*, vol. 57, no. 3, pp. 594–611, 2009.
- [9] A. Weisshaar, S. Goodnick, and V. Tripathi, "A rigorous and efficient method of moments solution for curved waveguide bends," *IEEE Trans. Microw. Theory Techn.*, vol. 40, no. 12, pp. 2200–2206, 1992.
- [10] A. A. S. Blas *et al.*, "A rigorous and efficient full-wave analysis of uniform bends in rectangular waveguide under arbitrary incidence," *IEEE Trans. Microw. Theory Techn.*, vol. 51, no. 2, pp. 397–405, 2003.

- [11] M. Mongiardo, A. Morini, and T. Rozzi, "Analysis and design of full-band matched waveguide bends," *IEEE Trans. Microw. Theory Techn.*, vol. 43, no. 12, pp. 2965–2971, 1995.
- [12] Q. Zhang, C.-W. Yuan, and L. Liu, "Theoretical design and analysis for te_{20} – te_{10} rectangular waveguide mode converters," *IEEE Trans. Microw. Theory Techn.*, vol. 60, no. 4, pp. 1018–1026, 2012.
- [13] J. Schorer, J. Bornemann, and U. Rosenberg, "Mode-matching design of substrate mounted waveguide (smw) components," *IEEE Transactions on Microwave Theory and Techniques*, vol. 64, no. 8, pp. 2401–2408, 2016.
- [14] R. R. Ricardo, "A study on the electromagnetic characterization of anisotropic materials in cylindrical measurement cells using the mode-matching method," Master Thesis, Dept. Elect. Eng., Pontifical Catholic University of Rio de Janeiro, Rio de Janeiro, RJ, Brasil, 2022.
- [15] L. Christie and P. Mondal, "Mode matching method for the analysis of cascaded discontinuities in a rectangular waveguide," *Procedia Computer Science*, vol. 93, pp. 251–258, 2016, proceedings of the 6th International Conference on Advances in Computing and Communications. [Online]. Available: <https://www.sciencedirect.com/science/article/pii/S187705091631448X>
- [16] X.-S. Fang and Z.-Q. Lin, "A coupled-mode approach to the analysis of fields in space-curved and twisted waveguides," *IEEE Trans. Microw. Theory Techn.*, vol. 35, no. 11, pp. 978–983, 1987.
- [17] A. Puzella and A. Palevsky, "Electromagnetic dispersion of a coaxial waveguide with an arbitrary radial dielectric profile," *IEEE Transactions on Electronic Devices*, vol. vol. 35, no. n. 11, pp. 2048–2051, 1988.
- [18] R. Yamada and K. Watanabe, "Propagation in cylindrical waveguide containing inhomogeneous dielectric," *IEEE Transactions on Microwave Theory and Techniques*, vol. vol. 13, no. n. 5, pp. 716–717, Sep. 1965.
- [19] R. F. Harrington, *Time-Harmonic Electromagnetic Fields*. New York, NY, USA: McGraw-Hill, 1961.
- [20] L. Biniashvili and A. Epstein, "Eliminating reflections in waveguide bends using a metagrating-inspired semianalytical methodology," *IEEE Transactions on Antennas and Propagation*, vol. 70, no. 2, pp. 1221–1235, Feb. 2022.

- [21] E. Marouby, M. Aubourg, and P. Guillon, "Application of the finite element method to the design of transitions between coaxial lines," in *IEE Proceedings H-Microwaves, Antennas and Propagation*, vol. 137. IET, 1990, pp. 219–225.
- [22] M. Warecka, R. Lech, and P. Kowalczyk, "Efficient finite element analysis of axially symmetrical waveguides and waveguide discontinuities," *IEEE Transactions on Microwave Theory and Techniques*, vol. 67, no. 11, pp. 4291–4297, 2019.
- [23] W. C. Chew, *Waves and Fields in Inhomogeneous Media*. IEEE press, 1995.
- [24] G. S. Rosa, "Pseudo-analytical modeling for electromagnetic well-logging tools in complex geophysical formations," Ph.D. dissertation, Dept. Elect. Eng., Pontifical Catholic University of Rio de Janeiro, Rio de Janeiro, RJ, Brazil, 2017.
- [25] G. S. Rosa and J. R. Bergmann, "Electromagnetic propagation along lossy anisotropic and radially stratified cylindrical structures," in *2014 Loughborough Antennas and Propagation Conference (LAPC)*. IEEE, 2014, pp. 155–159.
- [26] G. S. Rosa, "Propagação de ondas eletromagnéticas em estruturas coaxiais carregadas com meios não homogêneos excitadas pelo modo TEM," Master Thesis, Dept. Elect. Eng., Pontifical Catholic University of Rio de Janeiro, Rio de Janeiro, RJ, Brasil, 2013.
- [27] P. R. Evans, "Rotations and rotation matrices," *Acta Crystallographica Section D*, vol. 57, no. 10, pp. 1355–1359, Oct 2001. [Online]. Available: <https://doi.org/10.1107/S0907444901012410>